Solid-State NMR and DNP-Enhanced NMR Studies on Intrinsically Disordered Proteins

Inaugural-Dissertation

zur Erlangung des Doktorgrades

der Mathematisch-Naturwissenschaftlichen Fakultät

der Heinrich-Heine-Universität Düsseldorf

vorgelegt von

Boran ULUCA

aus

Sehitkamil, Türkei

Düsseldorf, Juli 2017

Aus dem Institut für Physikalische Biologie

der Heinrich-Heine Universität Düsseldorf

Gedruckt mit der Genehmigung

der Mathematisch-Naturwissenschaftlichen Fakultät

der Heinrich-Heine-Universität Düsseldorf

Referent: Prof. Dr. Henrike Heise

Korreferent: Dr. Manuel Etzkorn

Tag der mündichen Prüfung: 18.08.2017

Mountains, people, and even death feel exhausted,
now the most beautiful poem is PEACE.

Yaşar Kemal

Contents

List of figures

Abbreviations

CD	**C**ircular **D**ichroism
CE	**C**ross-**E**ffect
CIDNP	**C**hemically **I**nduced **D**ynamic **N**uclear **P**olarization
CP	**C**ross **P**olarization
CSA	**C**hemical **S**hift **A**nisotropy
CT	**C**onstant **T**ime
DMSO	**Di**methyl**s**ulf**o**xide
DNP	**D**ynamic **N**uclear **P**olarization
DQSQ	**D**ouble-**Q**uantum **S**ingle-**Q**uantum
EPR	**E**lectron **P**aramagnetic **R**esonance
fpRFDR	**f**inite **p**ulse **R**adio **F**requency-driven **D**ipolar **R**ecoupling
FRET	**F**luorescence **R**esonance **E**nergy **T**ransfer
IDPs	**I**ntrinsically **D**isordered **P**roteins
INEPT	**I**nsensitive **N**uclei **E**nhanced by **P**olarization **T**ransfer
MAS	**M**agic **A**ngle **S**pinning
MD	**M**olecular **D**ynamic
PDSD	**P**roton-**D**riven **S**pin **D**iffusion
PHIP	**P**ara-**H**ydrogen **I**nduced **P**olarization
REMD	**R**eplica-**E**xchange **M**olecular **D**ynamic
PD	**P**arkinson's **D**isease
RDCs	**R**esidual **D**ipolar **C**ouplings
SANS	**S**mall-**A**ngle **N**eutron **S**cattering
SAXS	**S**mall-**A**ngle **X**-ray **S**cattering
ssNMR	**S**olid-**s**tate **N**uclear **M**agnetic **R**esonance

Abstract

The 140 amino acid residue α-synuclein (α-syn) belongs to the family of intrinsically disordered proteins (IDPs). Thus, its native state does not adopt a well-defined single molecular structure but exists as a highly dynamic and heterogeneous ensemble of different conformers. While the exact function of the protein is not well understood, a considerable portion of α-syn can bind to the membrane in presynaptic terminals and is supposed to be associated with membrane structures at synaptic terminals. Additionally, its abnormal aggregation is associated with Parkinson's disease. Hence, we have studied conformational ensembles of α-syn in different states of the protein, i.e. the fully disordered form, the fibrillar form, and the membrane-bound state.

In this thesis, the combination in frozen solution NMR experiments with Dynamic Nuclear Polarization (DNP) has been used to overcome the inherently low sensitivity of solid-state NMR (ssNMR). Freezing the high conformational heterogeneity of IDPs at low temperature causes inhomogeneous line-broadening. While this is mostly accounted for as an unwanted side-effect of DNP-NMR, heterogeneous line-broadening contains valuable information about conformational ensembles of (disordered) proteins. We have explored the conformational ensemble of α-syn in the three states mentioned above from inhomogeneously broadened lines. Sparse labeling has enabled us to only label backbone atoms of the selected residue and reduce spectral overlap in the NMR spectra. As there is an empirical correlation between the protein backbone conformation and chemical shifts, we could exploit the secondary structure propensities of the protein. Our data on the monomeric form of α-syn in frozen solution is largely in line with conformational propensities of α-syn derived from NMR, SAXS and MD results, in which random-coil valine residues roughly sampled 70% β-sheet-like and 30% α-helical conformation. Utilizing this results, we could also estimate the secondary structure elements in fibrillar α-syn and test membrane binding of α-syn under different conditions.

Overall, in the first part of this thesis, we demonstrate that the DNP-enhanced NMR is a useful and powerful tool to study conformational ensemble of disordered proteins that are not accessible to solution NMR.

The [PSI $^{+}$] is a prion form of the Sup35 protein which is a subunit of the translation termination factor in yeast. The prion formation of Sup35 leads to read-through of stop codons, causing non-sense suppression. Despite the high interest on Sup35NM (N-domain together with the M-domain), there is no consensus on the organization of monomers within Sup35NM fibrils. One single point mutation in the Sup35NM sequence dramatically altered the amyloid core region. In the second part of this work, we have successfully determined the amyloid core region in fibrils of wild type as well as the S17R mutant of Sup35NM via distance measurements between the selectively ^{13}C labeled sites by ssNMR spectroscopy. In conclusion, our ssNMR results showed that different regions of the protein for wild type and the S17R mutant of Sup35NM are involved in the amyloid core region.

Zusammenfassung

α-Synuclein (α-syn), bestehend aus 140 Aminosäureresten, gehört zur Familie der intrinsisch ungeordneten Proteine (IDPs). Dies bedeutet, dass es keine wohl definierte native Konformation aufweist, sondern dynamisch eine Vielzahl von transienten Konformationen besitzt.

Die Funktion von α-Synuclein ist noch nicht gänzlich aufgeklärt. Es ist jedoch bekannt, dass ein Großteil des Proteins an Membranen der präsynaptischen Nervenenden bindet, und man vermutet, dass die Funktion mit der Bindung an diese Membranen zusammenhängt. Zudem ist bekannt, dass die Aggregation von α-Synuclein mit der Parkinson-Krankheit korreliert. Aus diesem Grund habe ich das Konformationen-Ensemble von α-Synuclein in verschiedenen Zuständen des Proteins, d.h. in nativer, fibrillärer und in Membran-gebundener Form, untersucht.

In der vorliegenden Dissertation wurden NMR Experimente an α-Synuclein in gefrorener Lösung in Kombination mit Hyperpolarisation (DNP) durchgeführt, um die inhärent geringe Sensitivität der Festkörper-NMR-Spektroskopie zu umgehen. Das Einfrieren der heterogenen Konformationen von IDPs führt zu inhomogener Linienverbreiterung. Obwohl dies häufig als ungewollter Nebeneffekt der DNP-NMR-Spektroskopie angesehen wird, enthalten die verbreiterten Linien wertvolle Informationen über das Konformationsensemble. Die Zusammensetzung der Konformationen wurde anhand der inhomogen verbreiterten Linien für jeden der drei oben genannten Zustände des Proteins untersucht. Mit Hilfe der *sparse* isotopen Markierungsstrategie wurden nur gewünschte Aminosäuren in der Sequenz markiert und somit die Überlappung der Signale in den Spektren reduziert. Aufgrund der empirischen Korrelation zwischen den chemischen Verschiebungen und der Konformation des Proteinrückgrates konnten die Sekundärstrukturelemente des Proteins ermittelt werden. Die erhaltenen Daten für monomeres α-Synuclein sind in guter Übereinstimmung mit früheren Konformationsstudien anhand von NMR und SAXS. In diesen Studien zeigte das Proteinrückgrat in der ungeordneten Form 30 % α-helikale und 70 % β-Faltblatt-typische Anteile. Monomeres α-syn gilt als vollständig ungeordnet, somit konnte die Anzahl der Reste geschätzt werden, die in fibrillärem und Membran-gebundenem Protein eine keine geordnete Struktur aufweisen.

Im ersten Teil der Dissertation wurde also gezeigt, dass DNP-Festkörper-NMR-Spektroskopie eine leistungsstarke Methode zur Untersuchung der Konformation von Proteinen ist, die nicht zugänglich für Lösung-NMR-Spektroskopie sind.

[PSI +] ist eine Prionenform des Sup35-Proteins, welches eine Untereinheit des Translationsterminationsfaktors ist. Die Bildung der Prionform von Sup35 führt zu einem vermehrten Überlesen des Stopcodons. Trotz des großen Forschungsinteresses an Sup35NM (N und M Domäne), herrscht noch kein Konsens über die Struktur der Moleküle in der Fibrille. Eine einzige Punktmutation in der Sup35NM Aminosäuresequenz ändert den Amyloid-Kernbereich bedeutend. Im zweiten Teil dieser Dissertation haben wir die

Amyloidkernbereiche in Fibrillen der Wildtyp-Form sowie von der S17R-Mutante von Sup35NM über Abstandsmessungen zwischen selektiv eingeführten ^{13}C-Isotopenmarkierungen mit Hilfe von Festkörper-NMR-Spektroskopie bestimmt. Zusammenfassend konnten wir besttätigen, dass verschiedene Bereiche des Proteins in der S17R Mutante und der Wildtyp-Form an der Fibrillenbildung beteiligt sind.

1 Introduction

1.1 Intrinsically Disordered Proteins

The traditional view of the structure-function paradigm is that the proper function of a protein requires a well-defined three-dimensional structure which is determined by its primary amino acid sequence and the external conditions [1]. This paradigm worked successfully for a large number of enzymes, proteins, and receptors. Nevertheless, with the development of new experimental techniques, it was proven that a number of proteins do not adopt a single defined tertiary structure under physiological conditions. Instead, they are described as an ensemble of interconverting conformations. This protein group is called intrinsically disordered proteins (IDPs) [2-4]. As energy barriers between the conformations are rather low [3, 5], IDPs can readily adopt different secondary structures under different conditions. For instance, α-synuclein (α-syn), which is a member of the IDP-family adopts a random-coil-like average ensemble of conformations in the monomeric form, and upon binding to a membrane readily adopts an α-helical structure [6-8]. Furthermore, α-syn can adopt an extended β-conformation and form a β-sheet structure, when following the energetically favorable pathway of aggregation and fibril formation. Because of its remarkable conformational flexibility, α-syn is also called 'protein-chameleon' [9].

IDPs carry out crucial biological functions such as transcriptional regulation, translation and cellular signal transduction [2, 10]. Understanding the function of IDPs is important because their altered availability is associated with a number of diseases, in particular, neurodegenerative diseases such as Alzheimer's disease [11], Parkinson's disease (PD) [12], and prion disease [13]. In the present thesis, α-syn and the prion protein Sup35 are studied and thus explained more in detail in the following sections.

1.1.1 α-synuclein

The 140 amino acid residue protein α-syn belongs to the family of IDPs. The primary sequence of the protein can be divided into three regions; *i)* the amphipathic N-terminal region (1-60) which contains the four 11-amino acid imperfect repeats with the highly conserved hexamer motif KTKEGV and facilitates membrane interactions, *ii)* a hydrophobic middle domain (61-95), also denoted NAC region which is essential for fibril formation and *iii)* the C-terminal region (96-140) which is rich in highly acidic residues (containing 10 glutamate and 5 aspartate residues) and prolines (Figure 1.a.) [14, 15]. The aggregation of α-syn is associated with various synucleinopathies including PD, dementia with Lewy bodies, and multiple system atrophy [16-19]. Despite a vast number of studies the physiological role of α-syn is not yet fully understood. α-syn is expressed predominantly in the brain and high concentrations of the protein are found in the presynaptic terminals in both soluble and membrane-bound forms [20, 21]. Thus, its role has been proposed to be associated with membrane structures at synaptic terminals such as

regulation of the size of presynaptic vesicles [22] and organization of phospholipid bilayers [23].

The N-terminus of the protein hosts 5 different familial mutations which result in early PD; A30P, E46K, A53T, H50Q, and G51D [24]. The positions of the mutations are shown in Figure 1.b. The A53T mutation is the first identified mutation that causes an inherited Lewy body disease [25]. This was followed by the identification of a second point mutation in the α-syn gene at position 30 (A30P) in a small German pedigree [26]. After the discovery of the relation between these two point mutations and PD, several excellent papers were published [12, 25, 27].

Although the exact native state of α-syn remains subject of active investigation and debate [28], most recent studies support the hypothesis that α-syn exists prevalently as a disordered monomer [29, 30]. The random coil structure of the protein is stabilized by long-range tertiary interactions between the C-terminal and the hydrophobic center region of the protein [31]. When binding to lipid bilayers or detergent micelles α-syn can readily adopt an α-helical conformation [6]. Both fibril formation and membrane binding strongly depend on the experimental conditions. At least five different polymorphic forms have been observed for α-syn amyloid fibrils [32-35]. Membrane binding critically depends on membrane properties, such as curvature and charge, as well as molecular crowding [36, 37]. Different membrane affinities have been determined for different regions of the protein [8].

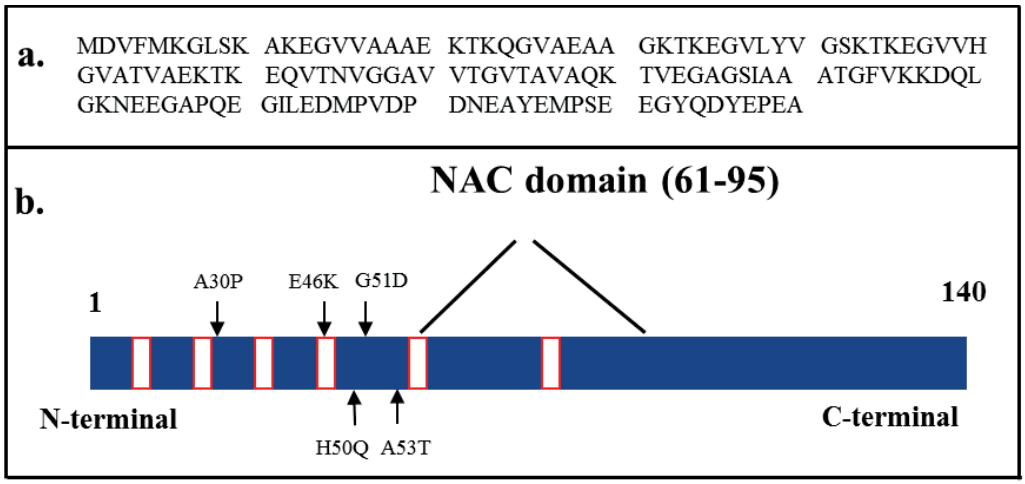

Figure 1. a. The primary sequence of human α-syn and **b.** its domain structure. The imperfect KTKEGV repeats are shown by red columns. The position of A30P, E46K, H50Q, G51D and A53T mutations are indicated by black arrows.

1.1.2 Yeast Prion-Sup35

The name prion is derived from "proteinaceous infectious particle" by *Stanley Prusiner* [38]. The replication of prions is based on the conversion of globular cellular prion protein

into its prion form without nucleic acid sequence [13]. Prions are found in both mammals and yeasts. The phenotypes [URE3], [PIN$^+$] and [PSI$^+$] in yeast are caused by prion formation of the proteins Ure2p, Rnq1p, and Sup35p, respectively.
The Sup35 is composed of 685 residues and consists of three domains. The N-terminal domain (residues 1-114) is rich in glutamine and asparagine amino acids and is essential for prion formation. The middle domain (residues 114-253) increases the solubility of the protein and the C-terminus (residue 253-685) is known as translation termination domain [39]. As shown in Figure 2, the presence of the prion form of Sup35 decreases the level of soluble Sup35 and leads to a read-through of stop codons which results in increased non-sense suppression [40]. Prion forms of Sup35 are sedimentable and more resistant to proteasomal degradation than the cellular form [41].

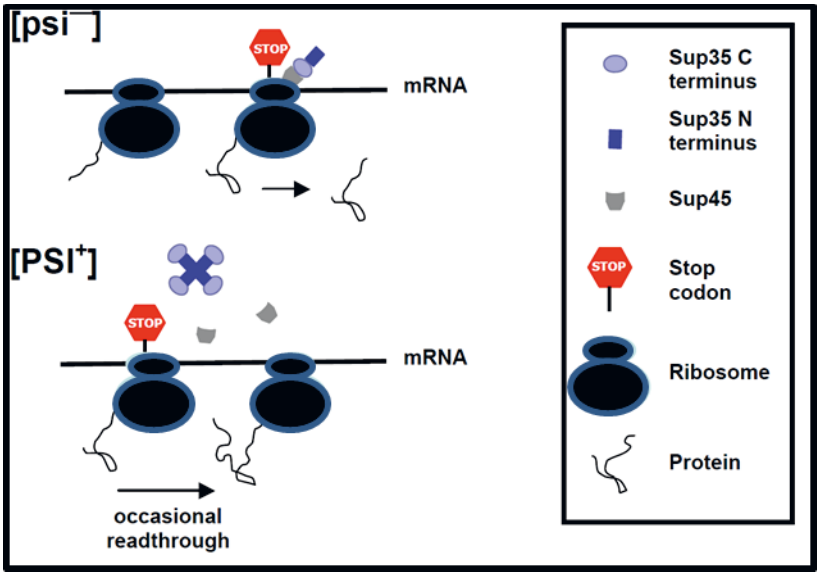

Figure 2: In [psi$^-$] (non-prion form) cells, Sup35 works in conjunction with Sup45 to terminate protein translation. In [PSI$^+$] cells, the N-termini of Sup35 aggregate, meaning there is less Sup35 available for translation termination and the ribosome reads through some stop codons. Adapted from [42].

Despite the vast number of studies on Sup35NM there is no consensus on the organization of monomers within Sup35NM fibrils. Some studies settle with a parallel in-register architecture [43-45] whereas others suggest a β-helical arrangement [46]. Long-range intermolecular interactions between the molecules of the same type can be determined by MAS-NMR spectroscopy. The most common experiment that measures the distance between selectively introduced isotope labels via dipolar dephasing, PITHIRDS, is explained in section 1.2.2.
The previous NMR-study of Sup35NM has already shown that Sup35NM can adopt distinct conformation at different temperature [47]. For example, Sup35 fibrils formed at 4

°C and 37 °C result in mitotically stable strong and weak [PSI^+] strains, respectively [44, 47, 48]. Furthermore, one point mutation, the substitution of serine at position 17 arginine, in the Sup35NM amino acid sequence alters the phenotype associated with the amyloid protein [49].

1.1.3 Conformational Ensemble of IDPs

As just mentioned above, IDPs can be characterized by an ensemble of rapidly interconverting conformations. The ensemble description of IDPs is a challenging area to understand the biological roles of the proteins.

To study the conformational ensemble of IDPs, both experimental and computational methods have been developed. On the experimental side, the secondary structure (α-helix and β-sheet*)* content of an IDP in solution can be determined by far-UV circular dichroism (CD) spectroscopy. Small-angle X-ray scattering and neutron scattering (SAXS and SANS) measurements can provide global structural parameters such as the radius of gyration (R_g, the average size of the scattering object in solution) and the maximum dimension (D_{max}) [50]. Fluorescence Resonance Energy Transfer (FRET) can provide a quantitative description of IDPs, i.e. the number of subpopulations and long-range conformational properties [4, 51-53].

Besides all, a well-established experimental method to study structures, dynamics, and functions of IDPs is nuclear magnetic resonance (NMR) spectroscopy. In an NMR experiment the main observable chemical shifts (CS) and the residual dipolar couplings (RDCs), which include information about the averaged orientation of inter-nuclear vectors within a reference frame, are sensitive to the conformational sampling of IDPs. The advantage of NMR is that one can study the desired molecule in a native-like environment. Solution NMR has been successfully applied to study the ensembles of IDPs [54, 55], however, it does not enable to simultaneously detect all the possible conformations of the protein, because of conformational averaging due to rapid molecular tumbling.

On the simulation side, a number of computational methods have evolved in recent years to overcome two main problems in the molecular dynamics (MD) simulation of IDPs: lack of sampling on the free energy surface and determination of the best force field for representation of the whole ensemble [56-58]. The implementation of the replica exchange molecular dynamic (REMD) algorithm is one of the most commonly used methods to overcome the sampling problem [56, 59]. The synergistic use of NMR together with classical MD simulations can extenuate the limitation of the solution NMR experiment and perform simulations that are inaccessible to NMR [58].

At lower temperature, the dynamic disorder of molecules can be slowed down or even frozen out. Solid-state NMR (ssNMR) is a method of choice to study these frozen solutions [60-63]. As ssNMR spectra of biological samples suffer from low sensitivity, the combination of frozen solution NMR experiments with Dynamic Nuclear Polarization (DNP) [64, 65] can be applied to study the whole ensemble of an IDP [66].

1.2 Solid-state Nuclear Magnetic Resonance Spectroscopy

Magic Angle Spinning (MAS) ssNMR Spectroscopy has been successfully applied to biological samples to obtain information at the atomic level [67-69]. Moreover, developments regarding higher magnetic fields, efficient sample preparation and the introduction of new pulse sequences made ssNMR a versatile tool for structural studies on biomolecules such as membrane proteins [70, 71], amyloid fibrils [32, 72, 73] and prion proteins [74, 75]. In contrast to solution NMR, which is limited by solubility and molecular weights of samples, ssNMR does not face these limitations. Consequently, it can be applied to a wide range of samples e.g. non-soluble and non-crystalline materials [76], large protein complexes [77], polymeric samples [78], as well as samples in frozen solutions [60-62, 66, 79].

1.2.1 Theoretical Background

In ssNMR experiments there are mainly two anisotropic interactions causing line broadening:

- **Chemical shift anisotropy (CSA):** As each nucleus is surrounded by electron clouds, an induced field is generated around the nucleus when an external magnetic field is applied to the system. This causes partial shielding of the nucleus from the external magnetic field [80]. The extent of shielding is influenced by both the chemical environment of the nucleus and the orientation of the molecule with respect to the magnetic field (in solid samples). The observed chemical shift can be written as the sum of the isotropic and anisotropic chemical shifts and is given in equation 1.

$$\delta_{obs} = \delta_{iso} + \frac{1}{3}\sum_{k=1}^{3}(3\cos\theta^2 - 1) * \delta kk \tag{1}$$

$$\delta_{iso} = \frac{1}{3}(\delta_{11} + \delta_{22} + \delta_{33}) \tag{2}$$

δ_{iso} is the isotropic chemical shift (the average of the three main values δ_{11}, δ_{22}, δ_{33}, given in equation 2) and θ represents the orientation of the inter-nuclear vector relative to the external magnetic field. The orientation dependent part is called CSA.

- **Dipolar Coupling:** The interaction between two neighboring spins in spatial proximity is known as dipolar coupling. The strength of dipolar coupling, D has a linear dependence on the gyromagnetic ratios of the nuclei ($\gamma_1$and γ_2) and is inversely proportional with the third power of the interatomic distance. D is defined as follows

$$D = \hbar(\frac{\mu_0}{4\Pi})\frac{\Upsilon_1\Upsilon_2}{r^3_{1,2}} \quad (3)$$

where $\hbar$ is the reduced Planck constant, μ_0 is the vacuum permeability and $r_{1,2}$ is the distance between the dipolar coupled nuclei.

As these two interactions are anisotropic they lead to very broad lines in ssNMR spectra. In solution, these interactions are averaged out by rapid molecular motion. In ssNMR, this averaging can be mimicked by spinning the sample around a specific angle (54.74°) with respect to the external magnetic field. This technique became known as MAS [81]. Spinning the sample causes a periodic modulation of the anisotropic interactions CSA and dipolar coupling which are thus averaged out over a sample rotation period.

In a biological sample which has a dense proton network, the heteronuclear dipolar couplings between protons and low abundant nuclei like ^{13}C or ^{15}N can cause line broadening even under MAS conditions. If a heteronucleus is coupled to a proton which changes orientation during one rotor period the signal of this nucleus will not be refocused and causes homogenous line broadening. Thus, in addition to MAS, high power proton decoupling during the evolution and acquisition time is needed to get well-resolved spectra.

1.2.2 Homonuclear Dipolar Recoupling-PITHIRDS

As explained above, in a ssNMR experiment dipolar couplings are averaged out by MAS. However, dipolar couplings contain valuable structural information such as inter-nuclear distances [82-84]. The strength of the dipolar interaction is inversely proportional to r^3, where r is the distance between the interacting nuclei. Reintroducing this information into the spectra under MAS has been a subject of ssNMR since the late 1980s. Several homonuclear and heteronuclear recoupling pulse sequences have been introduced. Here, PITHIRDS-CT which is a symmetry-based constant time (CT) homonuclear dipolar recoupling technique is explained. For other homonuclear and heteronuclear recoupling techniques, the interested reader is referred to appropriate publications [85-91]. Additionally, we recently wrote a book chapter which includes recoupling techniques in biomolecular NMR [92].

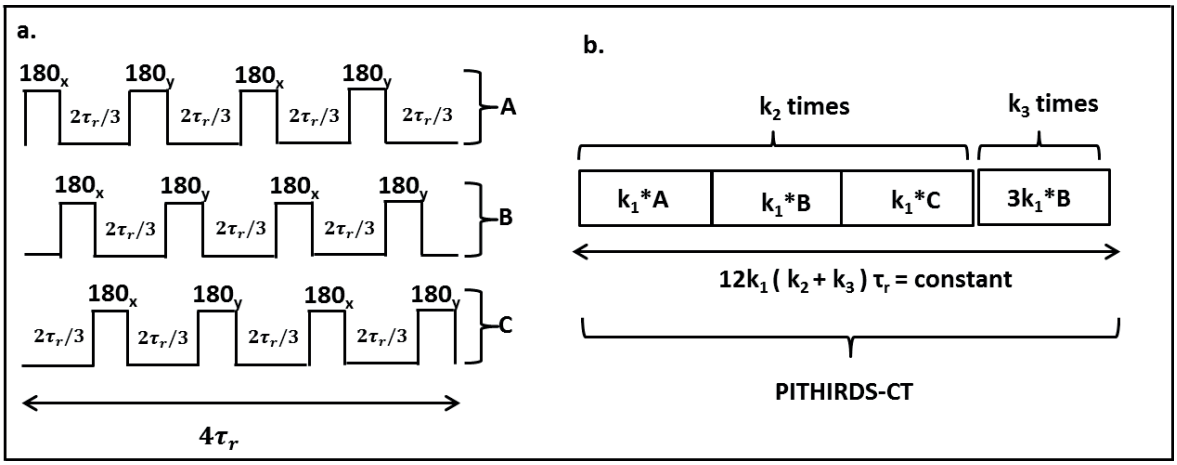

Figure 3 a. A, B, and C are three fpRFDR blocks which are differing in the positions of π pulses within the MAS rotation period τ_r, used in symmetry based constant time homonuclear dipolar recoupling experiments. **b**. Schematic representation of PITHIRDS-CT pulse sequence. Adapted from [93].

PITHIRDS-CT is a constant-time variant of the finite pulse radio frequency-driven dipolar recoupling (fpRFDR) technique in which the total pulse length and total number of radio frequency pulses are kept constant. The conditions of PITHIRDS-CT are explained in more detail by *Tycko* [93]. Briefly, RFDR is a homonuclear recoupling sequence consisting of one 180^0 pulse each MAS rotation period. Under high spinning speed, the pulse width of 180^0 pulses is not short compared to the rotor period and becomes a significant fraction of it. In this case, they cannot be treated as delta pulses (negligible pulse) anymore. Instead, the length of the 180° pulses is set to one-third of the rotor period [84]. Furthermore, dipolar dephasing curves are affected by transverse relaxation, which adds to the dipolar dephasing. This contribution of T_2 relaxation can be eliminated by keeping the transverse evolution time and the number of pulses constant. As shown in Figure 3.a., the 180^o pulses have a different location within the A, B, and C blocks to create a super sequence with a zero average dipole-dipole Hamiltonian. This means the overall effect of the blocks A, B and C together on the spin system is zero, also called pseudorecoupling. These three blocks are used to keep the total experimental time constant. Therefore, only during the "k_3" period which represents a classical rfdr recoupling sequence, dipolar recoupling takes place. Dipolar dephasing curves can then be recorded by simultaneously extending k3 and reducing k2 while keeping the total number of pulses constant.

The PITHIRDS-CT experiment has been used to detect intermolecular ^{13}C-^{13}C dipole-dipole couplings in ^{13}CO-labeled samples [44, 45, 94]. The decay of the ^{13}C-NMR signal intensity under PITHIRDS-CT sequence is related to the distance between the labeled ^{13}CO pairs. An in-register parallel β-sheet organization in amyloid fibrils, which has roughly 4.7 Å inter-strand distance (Figure 4.a.), shows a fast signal dephasing curve, as

has been observed in the prion domain of Sup35 [95] and Ure2p [74] by ssNMR. The β-sheet core arrangement of WT Sup35NM and the S17R mutant of Sup35NM is explained by *Ohhashi et al* [49]. The dephasing curve for a uniformly or extensively ^{13}C-labelled sample can be compared with numerical simulations to determine inter-nuclear distances [96]. PITHIRDS-CT reference dephasing curves were calculated using a linear five-spin system with inter-nuclear distances from 4 Å to 7 Å by simulation programs such as SIMPSON [97], gamma [98] or SPINEVOLUTION [99]. Reference dephasing curves are shown in Figure 4.b.

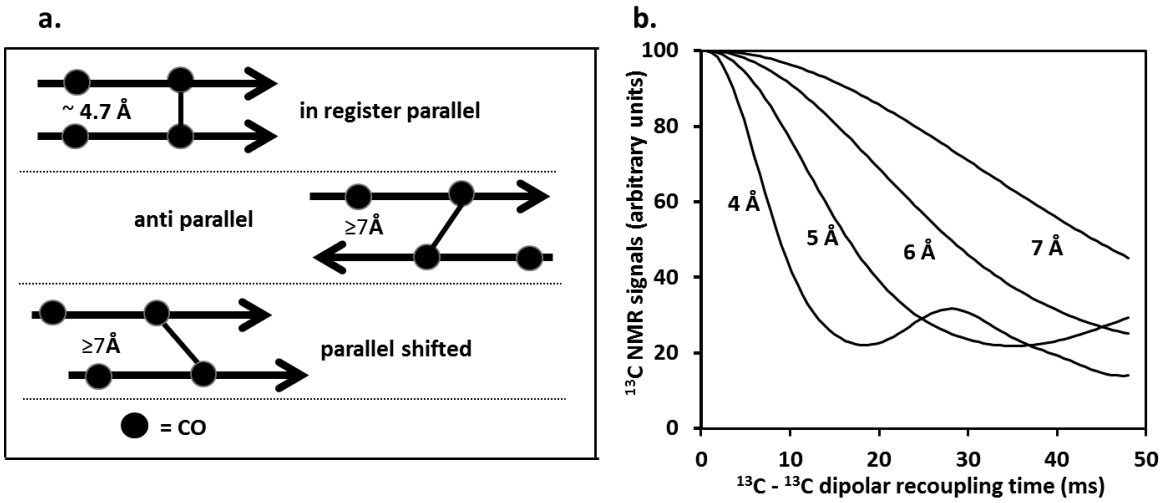

Figure 4 a. Representation of inter-nuclear distances between two labeled ^{13}C nuclei in different β-sheet structures; like in-register parallel, anti-parallel and parallel shifted β-sheet structures. In-register parallel β-sheets have the shortest inter-strand distance. **b**. Simulated PITHIRDS-CT curves are shown for ideal linear chains of ^{13}C nuclei with the indicated spacing.

1.3 Dynamic Nuclear Polarization

Application of traditional MAS ssNMR experiments in larger molecules suffers from low sensitivity due to the extremely low energy involved in nuclear spin transitions. This is particularly critical for nuclei with low gyromagnetic ratio γ combined with a low natural abundance such as ^{13}C and ^{15}N (natural abundance of ^{13}C: ~1.07 %, ^{15}N: ~0.37 %). Several techniques have been developed to overcome this issue. On the sample preparation side, different synthesis strategies and labeling techniques and methods are used for the generation of isotopically enriched samples, such as solid-phase peptide synthesis [100, 101], cell-free expression [102] and uniform or selective ^{13}C- and ^{15}N-labeling [103-105] by recombinant protein expression in *Escherichia coli*.

The Boltzmann distribution of the population of spin states is given by the following equation;

$$P = \frac{p_+ - p_-}{p_+ + p_-} = \tanh\left(\frac{\gamma \hbar B_0}{2kT}\right) \quad (4)$$

where p_+ and p_- are the populations of the spin up and down, respectively, $\hbar$ is the reduced Planck constant, γ is the gyromagnetic ratio of the nucleus, B_0 is the static magnetic field strength, k is the Boltzmann constant and T is the temperature in Kelvin. According to this equation, increasing the applied magnetic field or decreasing the sample temperature can help to get better sensitivity in the NMR signal. In this respect, hardware developments (for high magnetic field) proved to be extremely valuable in the NMR field to get better sensitivity. Additionally, applying improved specific polarization transfer schemes such as Cross Polarization (CP) [106] and insensitive nuclei enhanced by polarization transfer (INEPT) [107] can enhance the signal intensity of low γ nuclei. In such an experiment one can exploit the high γ of the starting nucleus by transferring it to the nucleus with low γ.

Alternatively, it is possible to use a "hyperpolarization" technique such as Para-Hydrogen Induced Polarization (PHIP) [108, 109], Chemically Induced Dynamic Nuclear Polarization (CIDNP) [110, 111] and Dynamic Nuclear Polarization (DNP). Here, DNP-enhanced ssNMR is briefly introduced, for the other techniques the interested reader is referred to appropriate reviews [112-114].

DNP was firstly proposed by *Albert Overhauser* in 1953 [65]. It is based on transferring the high spin polarization of unpaired electrons to the surrounding nuclei using continuous high-power microwave irradiation to excite electronic spin transitions. In the same year, the concept was demonstrated experimentally in metallic lithium using a static magnetic field of 3 mT by *Thomas Carver* and *Charles Slichter* [64]. The theoretical maximum sensitivity enhancement is equal to the ratio of the electron and nuclear spin gyromagnetic ratios (γ_e / γ_n). For protons a maximum enhancement factor of 660 could be achieved in principle [64].

Figure 5. A commercial Bruker Avance III HD spectrometer operating at 600 MHz, equipped with a 395.18 GHz second-harmonic gyrotron, corrugated wave guide and cooling cabinet. It is located at the Jülich-Düsseldorf Biomolecular NMR Center in Jülich, Germany and jointly run by the Forschungszentrum Jülich and the Heinrich-Heine-University Düsseldorf.

1.3.1 DNP Mechanisms

The electron polarization can be transferred to the surrounding nuclei via four different DNP mechanisms; Overhauser effect, Solid effect, Cross effect and Thermal mixing. The dominant DNP mechanism in an experiment depends on the experimental conditions such as the applied magnetic field, the radical concentration, and the sample temperature. As the cross effect is the mechanism used in this work we will focus on it, the other mechanisms will be briefly discussed.

1.3.1.1 *Overhauser Effect*

The Overhauser effect is the first DNP mechanism proposed by *Albert Overhauser* to make use of the large electron polarization for NMR experiments. It is a two-spin cross-relaxation process consisting of one electron and one nuclear spin between the hyperfine-coupled electron and nuclear spins.

The Overhauser effect is an efficient mechanism at low magnetic fields. At high magnetic fields, this mechanism has been successfully applied for the study of small molecules [115-117]. For bigger molecules, the main drawback is the rapid decrease of the enhancement level [118]. As the Overhauser effect depends on the local dynamics, the system should contain either mobile electrons or liquids (where molecules have high tumbling rates).

Additionally, for an efficient Overhauser mechanism, the microwave power has to be tuned to the electron Larmor frequency.

1.3.1.2 *Solid Effect*

The Solid effect relies on forbidden zero quantum or double quantum electron-nuclear transitions [119]. However, it is partially allowed because of the mixing of adjacent states and can be excited by high power microwave irradiation [120]. The electron polarization is transferred to the core nuclei when the microwave irradiation satisfies the $\omega_e \pm \omega_n$ condition (ω_e and ω_n are electron and nuclear Larmor frequencies, respectively).

The Solid effect is an efficient mechanism in systems where electrons have little or no g-anisotropy with narrow EPR spectra. Both the inhomogenous EPR line width Δ and the homogenous EPR linewidth δ, have to be less than the nuclear Larmor frequency ω_n. The condition is given as $\delta, \Delta < \omega_n$ [121, 122]. TEMPO and BDPA are available mono-radicals for this transition [123].

1.3.1.3 *Cross Effect*

Cross Effect (CE)-DNP is the most commonly used transfer mechanism for signal enhancement in solid-state MAS NMR-spectroscopy of biomolecules. It was described by *Kessenikh et al*. in the 1960s and relies on a three-spin process between two strongly-dipolar coupled electron spins and one nuclear spin [124-127]. It requires an inhomogeneous EPR linewidth Δ of the polarizing agent larger than the nuclear Larmor frequency ω_n, while the homogeneous linewidth δ remains small ($\delta < \omega_n < \Delta$) [128, 129]. Since three-spin states are involved in the CE mechanism, eight energy levels, as shown in Figure 6, are involved. If the frequency difference between the two electrons (ω_{e1} and ω_{e2}) is equal to the nuclear Larmor frequency ($\omega_{e1} - \omega_{e2} \sim \omega_n$), the energy levels |4> and |5> become degenerate. In this case, the saturation of an EPR transition for one dipolar coupled electron ω_{e1} (low field) leads to negative NMR polarization, whereas saturation of the second transition ω_{e2} (high field) leads to a positive signal enhancement. The CE relies on the irradiation of the allowed EPR transitions. The efficiency of the CE mechanism is affected by several experimental parameters such as the applied magnetic field, the microwave power, and the polarizing agent's properties. Importantly, as the CE mechanism relies on a three-spin process including two dipolar coupled electrons and one nucleus, the electron-electron dipole coupling is a crucial parameter for an efficient CE mechanism [130]. For this reason, using biradicals with certain distances can yield better signal enhancement. As shown in Figure 7., TEMPO and TEMPO-based radicals, like AMUpol and TOTAPOL, support the CE-DNP [131].

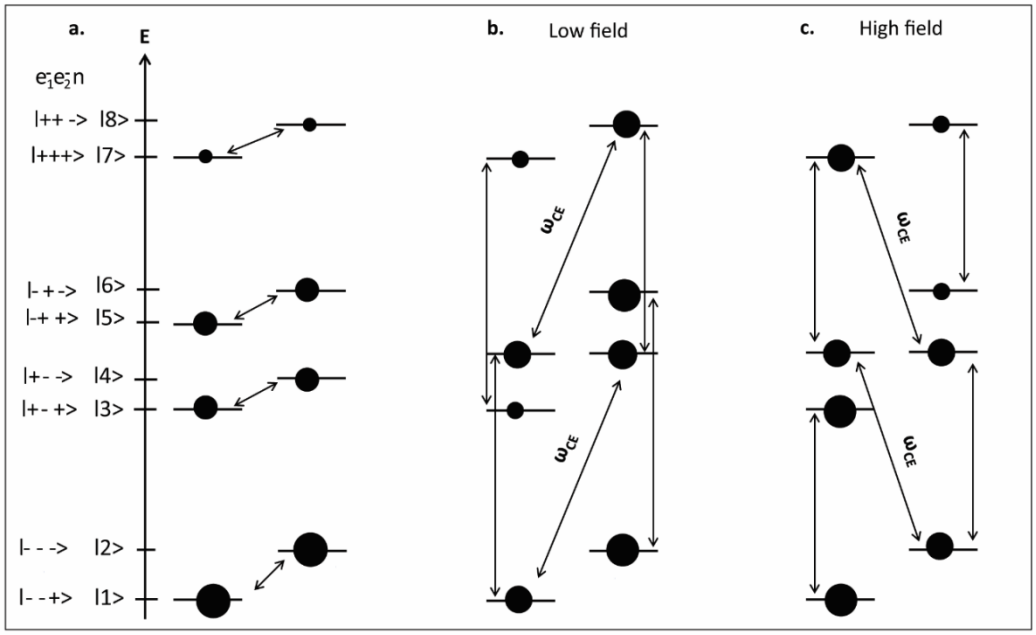

Figure 6. Representation of the energy level diagrams of the Cross effect mechanism at **a.** thermal equilibrium**, b.** low and **c**. high magnetic field. Circles represent the relative amount of the magnetization on every energy level.

1.3.1.4 *Thermal Mixing*

Thermal mixing was proposed by *Borghini* [132] and re-proposed in a slightly different way by *Abragam* and *Goldman* [133]. Multiple electrons and one nucleus are involved in the Thermal mixing mechanism [134]. Additionally, the homogeneously broadened EPR linewidth δ needs to be larger than the nuclear Larmor frequency ω_n ($\omega_n > \delta$). Thermal mixing is observed at rather high radical concentrations. So it can be neglected at the high magnetic field strengths and low concentrations of radicals used in most common applications of MAS-DNP.

1.3.2 Experimental Requirements for DNP

The sample preparation protocol has to be optimized to ensure the achievement of sufficient enhancement and resolution in DNP-NMR experiments. A typical DNP sample consists of three parts: radicals, buffer and the sample of interest. Radicals are used as source for unpaired electron spins and the buffer contains a partly deuterated cryoprotectant/water mixture.

Here, the sample preparation for an efficient CE mechanism under ssDNP-NMR conditions is explained.

DNP experiments require a suitable paramagnetic centre as the source of electron polarization. This can be either an endogenous or exogenous paramagnetic system. As most protein samples of interest for DNP-enhanced NMR are diamagnetic, exogenous

polarizing agents are needed. For an efficient ssDNP-NMR experiment three points have to be addressed: *i.)* the polarizing agent needs to be soluble in the solvent of choice and homogeneously mix with the sample, *ii.)* a favorable relaxation time of the electron is desirable and *iii.)* stable radicals are preferred because it is easy to control their concentration in the sample. Employing TEMPO-based biradicals allow achieving better DNP enhancements for CE mechanism than with monoradicals [130, 135]. The water soluble biradical TOTAPOL is compatible with biological systems and is used by many NMR-groups [136-138]. Another common biradical, AMUPol, results in much higher efficiencies in comparison with TOTAPOL because of longer electron relaxation times and larger electron-electron dipole couplings [139, 140].

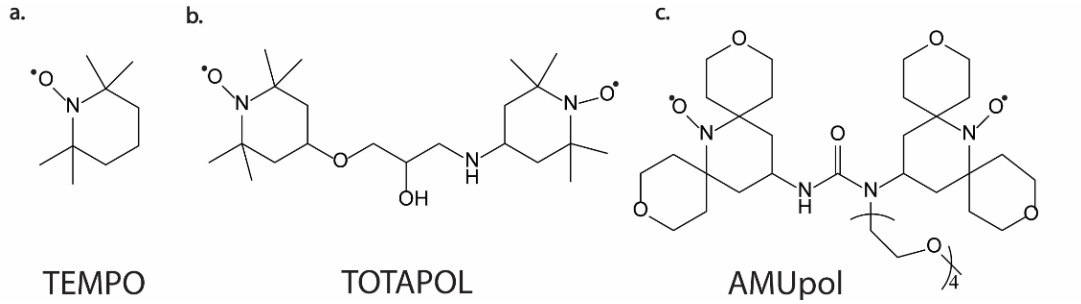

Figure 7. Chemical structures of common radicals used for DNP experiments: **a.** TEMPO is a nitroxide based monoradical. **b.** TOTAPOL and **c**. AMUPol, the biradical derivatives of TEMPO, are used to induce the CE mechanism.

The radical concentration should be optimized according to the system. Higher concentrations of radicals may cause homogeneous line broadening due to paramagnetic relaxation enhancement (PRE) [141]. On the other hand, electrons in the sample should provide a sufficient source of polarization for an efficient DNP experiment. Another important parameter which affects both the enhancement factor and the resolution is the deuteration level of the matrix. The deuteration of the solvent can improve polarization transfer both from electrons to nuclei and from protons to heteronuclei. As a consequence by prolonging the relaxation times significant larger enhancement factors can be achieved [136]. On the other hand, protons are needed to spread polarization in the bulk. The optimized buffer condition for DNP studies of biomolecules includes 10 % of protons (60 % d_8-glycerol, 30 % D_2O, 10 % H_2O). All experiments in this thesis are performed under these buffer conditions and with a concentration of 2.5 mM AMUPol.
The electronic spin transitions are excited by microwave irradiation and thus, to prevent sample heating, DNP experiments are carried out at low temperatures (using cold nitrogen gas, Figure 5). To avoid ice crystal formation a cryoprotectant such as dimethylsulfoxide (DMSO) or glycerol is needed [135, 136]. Additionally, the cryoprotectant serves to

disperse the radical homogeneously and thus to achieve optimal polarization distribution [140].

Lastly, at low temperatures different conformations of the protein freeze out and chemical shift differences are no longer averaged out by rapid conformational sampling. The corresponding NMR lines are found to be inhomogenous. As most of the DNP-NMR spectra of IDPs suffer from this inhomogeneous line broadening, labeling strategies for the reduction of labeled ^{13}C spins in the sample are desirable. In contrast to uniform labeling approaches, specific labeling can help to minimize signal overlap for big proteins such as TEASE labeling, where [2-^{13}C] or [1-^{13}C] glucose is used as a sole carbon source in the expression medium [105].

1.4. Scope of This Thesis

Aim #1. DNP overcomes the inherently low sensitivity of magnetic resonance methods by transferring high spin polarization of unpaired electrons to surrounding nuclei. Low-temperature NMR spectra usually suffer from severe line broadening due to the freezing out of different conformations [142]. While this is usually accounted for as an unwanted side-effect of DNP-NMR, these inhomogeneously broadened lines also contain valuable information about conformational ensembles of (disordered) proteins.

We made use of inhomogeneous line broadening to study conformational ensembles of IDPs. For the experiments reported here, we have chosen α-syn as a model protein and the large-scale conformational flexibility is investigated by DNP-enhanced NMR spectroscopy and complemented by molecular dynamics (MD) simulations. We have studied the conformational ensemble of α-syn in frozen solution under different conditions: in the fully disordered form, in the fibrillated form with flexible ends, and in contact with lipid bilayers in the form of nanodiscs.

Aim #2. The [PSI^+] prion is a self-propagating amyloid form of the protein Sup35, which is a subunit of the translation termination factor [143]. As mentioned above, there is no consensus on the organization of monomers within Sup35NM fibrils. However, some of previous solid-state NMR structural studies on a construct containing the N and M domains, Sup35NM, have shown that it has a parallel in register β-sheet core region whose length depends on the fibrillation temperature [44]. One single point mutation, the substitution of S17 by a positively charged R residue, is sufficient to prevent S17R mutant of Sup35 monomers from being co-fibrillated with wild-type Sup35NM [39]. However, the S17R monomers can form fibrils themselves at 4°C, as well as at 37°C. The aim of the present work is to investigate the amyloid core arrangement of the wild-type as well as S17R mutant of the Sup35NM protein.

In the second part of this thesis, we have used symmetry-based constant-time homonuclear dipolar recoupling experiments [93] to probe the amyloid core region of wild type and S17R mutant of Sup35NM. Our results have shown that one point mutation can dramatically alter the amyloid core region of Sup35NM.

2 Publications

2.1 Modulation of Structural and Kinetic Determinants of α-synuclein Aggregation by Stable, Planar Lipid-bilayer Nanodiscs

Thibault Viennet, Michael M. Wördehoff, Boran Uluca, Chetan Poojari, Hamed Shaykhalishahi, Dieter Willbold, Birgit Strodel, Henrike Heise, Alexander K. Buell, Wolfgang Hoyer, and Manuel Etzkorn

Journal: Communications Biology

Impact Factor: - (New Journal)

Doi: 10.1038/s42003-018-0049-z.

Corresponding Author: Manuel Etzkorn, manuel.etzkorn@hhu.de

Contribution: 7%

Involved in the expression and purification part of sparsely labeled α-synuclein. Involved in Magic-angle spinning solid-state DNP-NMR experiments performed for membrane-bound α-synuclein.

Reprint

This section contains a complete reprint of the publication Communications Biology volume 1, Article number: 44 (2018), doi: 10.1038/s42003-018-0049-z. This article is available under the terms of the Creative Commons Attribution License (CC BY) which can be found here: https: //creativecommons.org/licenses/by/4.0/.

2.2 DNP-Enhanced Solid-state NMR at Cryogenic Temperatures: a Tool to Snapshot Conformational Ensembles of α-Synuclein in Different States

Boran Uluca, Hamed Shaykhalishahi, Dusan. Petrović, Thibault Viennet, Franziska Weirich, Aysenur Gönülalan, Birgit Strodel, Manuel Etzkorn, Wolfgang Hoyer, and Henrike Heise

Journal: Biophysical Journal

Impact Factor: 3.6 (2016)

Doi: 10.1016/j.bpj.2018.02.011

Corresponding Author: Henrike Heise, h.heise@fz-juelich.de

Contribution: 80%

Involved in the conception and design of the experiments; except for nanodisc preparation. Conducted all other experimental parts and data analysis. Involved in writing the manuscript.

Reprint

This section contains a complete reprint of the publication Biophysical Journal 2018 April 10;114(7):1614-1623, doi: 10.1016/j.bpj.2018.02.011. This article can be found here: https://www.sciencedirect.com/science/article/pii/S0006349518302145?via%3Dihub

2.3 Molecular Basis for Diversification of Yeast Prion Strain Conformation

Yumiko Ohhashi, Yoshiki Yamaguchi, Yuji O. Kamatari, Shinju Sugiyama, Boran Uluca, Timo Piechatzek, Yusuke Komi, Toshinobu Shida, Henrik Müller, Shinya Hanashima, Henrike Heise, Kazuo Kuwata, and Motomasa Tanaka

Journal: Proceedings of the National Academy of Sciences

Impact Factor: 9.6 (2016)

Doi: 10.1073/pnas.1715483115

Corresponding Author: Motomasa Tanaka, motomasa@brain.riken.jp

Contribution: 7%

Performed Magic-angle spinning solid-state NMR experiments for all samples and involved in the data analysis.

Reprint

This section contains a complete reprint of the publication PNAS March 6, 2018. 115 (10) 2389-2394, doi: 10.1073/pnas.1715483115.

2.4 Methods for Complex Systems–Isotopically Enriched Systems (Chapter 10)

Claudia Beumer, Anna König, Daniel Schölzel, Boran Uluca, Franziska Weirich and Henrike Heise

Publisher: Royal Society of Chemistry

Book Title: Modern Methods in Solid-state NMR: a Practitioner´s Guide

Editor: Paul Hodgkinson, paul.hodgkinson@durham.ac.uk

Type: Book Chapter

Doi: 10.1039/9781788010467-00289

eISBN: 978-1-78801-046-7

Contribution: 17%

Wrote the subsection “Signal enhancement by dynamic nuclear polarization”

This article can be found here:
http://pubs.rsc.org/en/content/chapterhtml/2018/bk9781782628545-00289?isbn=978-1-78262-854-5&sercode=bk

3 Conclusion

The work in this doctoral thesis can be divided into two parts. In the first part conformational ensembles of IDPs were studied. The definition of a representative conformational ensemble sampled by IDPs usually requires the combination of different methodologies. This work showed us that it is possible to probe conformational distributions only with one experiment and in one day. DNP-enhanced ssNMR was successfully applied to frozen solutions. This method allowed us to probe representative conformational ensembles sampled by IDPs with high sensitivity. The conformational ensembles for different states were produced in good agreement with previous studies for our model protein chameleon, α-syn. More importantly, we could observe α-helical signals from the membrane binding region of α-syn which was not possible with our previous solution-state NMR study. The proportion of random coil secondary structure could be quantified for different protein-to-nanodisc ratios. Our both results from solution-state NMR and DNP-enhanced solid-state NMR have shown the same trend of increasing random-coil conformation with increasing protein to nanodisc ratio.

Furthermore, we have observed that in order to achieve accurate signal quantification, one should take the deuterated matrix into account. We compared two experiment types used in this thesis, PDSD and DQSQ spectra and saw that DQSQ spectra are more reliable than PDSD spectra. PDSD polarization transfer relies on the proton network, and the transfer efficiency is clearly affected by the proton/deuterium ratio in the close environment of the involved nuclei. Thus, for all the quantitative analyses in this thesis were carried out on DQSQ spectra.

Additionally, we have conducted long replica exchange MD simulations with three different force fields and two solvent models. The comparison of all MD results showed that the AMBER99SB*-ILDN force field with explicit solvent nearly samples the complete conformational ensemble of valine residues. We could successfully produced the two-dimensional ^{13}C-^{13}C correlation spectrum for an ensemble of valine residues.

In the second part of this thesis, yeast prion Sup35NM is studied. In order to investigate the effect of S17R mutation on the position of amyloid core region of the protein, PITHIRDS-CT experiment is carried out on both wild-type and S17R mutant of Sup35NM. The comparison of PITHIRDS-CT experimental results showed different decay curves for both types. As the rate of decay of the NMR signal is primarily a reflection of internuclear distances, we have concluded that one single point mutation can alter the core region dramatically. Additionally, our ssNMR data on Sup35NM are consistent with Mass Spectral Analysis results of the protein.

4 References

1. Wright, P.E. and H.J. Dyson, *Intrinsically unstructured proteins: re-assessing the protein structure-function paradigm.* Journal of Molecular Biology, 1999. **293**(2): p. 321-331.
2. Dyson, H.J. and P.E. Wright, *Intrinsically unstructured proteins and their functions.* Nature Reviews Molecular Cell Biology, 2005. **6**(3): p. 197-208.
3. Burger, V.M., D.O. Nolasco, and C.M. Stultz, *Expanding the Range of Protein Function at the Far End of the Order-Structure Continuum.* Journal of Biological Chemistry, 2016. **291**(13): p. 6706-6713.
4. Rauscher, S., et al., *Structural Ensembles of Intrinsically Disordered Proteins Depend Strongly on Force Field: A Comparison to Experiment.* J Chem Theory Comput, 2015. **11**(11): p. 5513-24.
5. Zhang, W.H., D. Ganguly, and J.H. Chen, *Residual Structures, Conformational Fluctuations, and Electrostatic Interactions in the Synergistic Folding of Two Intrinsically Disordered Proteins.* Plos Computational Biology, 2012. **8**(1).
6. Eliezer, D., et al., *Conformational properties of alpha-synuclein in its free and lipid-associated states.* J Mol Biol, 2001. **307**(4): p. 1061-73.
7. Ulmer, T.S., et al., *Structure and dynamics of micelle-bound human alpha-synuclein.* Journal of Biological Chemistry, 2005. **280**(10): p. 9595-9603.
8. Fusco, G., et al., *Direct observation of the three regions in alpha-synuclein that determine its membrane-bound behaviour.* Nature Communications, 2014. **5**.
9. Uversky, V.N., *A protein-chameleon: Conformational plasticity of alpha-synuclein, a disordered protein involved in neurodegenerative disorders.* Journal of Biomolecular Structure & Dynamics, 2003. **21**(2): p. 211-234.
10. Tompa, P., *Intrinsically unstructured proteins.* Trends in Biochemical Sciences, 2002. **27**(10): p. 527-533.
11. Glenner, G.G. and C.W. Wong, *Alzheimers-Disease - Initial Report of the Purification and Characterization of a Novel Cerebrovascular Amyloid Protein.* Biochemical and Biophysical Research Communications, 1984. **120**(3): p. 885-890.
12. Lücking, C.B. and A. Brice*, *Alpha-synuclein and Parkinson's disease.* Cellular and Molecular Life Sciences CMLS, 2000. **57**(13-14): p. 1894-1908.
13. Prusiner, S.B., *Prions.* Proceedings of the National Academy of Sciences of the United States of America, 1998. **95**(23): p. 13363-13383.
14. Li, D., et al., *Structure-Based Design of Functional Amyloid Materials.* Journal of the American Chemical Society, 2014. **136**(52): p. 18044-18051.
15. Iwai, A., et al., *Non-A beta component of Alzheimer's disease amyloid (NAC) is amyloidogenic.* Biochemistry, 1995. **34**(32): p. 10139-45.
16. Spillantini, M.G., et al., *Alpha-synuclein in Lewy bodies.* Nature, 1997. **388**(6645): p. 839-40.
17. Luk, K.C., et al., *Pathological alpha-synuclein transmission initiates Parkinson-like neurodegeneration in nontransgenic mice.* Science, 2012. **338**(6109): p. 949-53.
18. Jucker, M. and L.C. Walker, *Self-propagation of pathogenic protein aggregates in neurodegenerative diseases.* Nature, 2013. **501**(7465): p. 45-51.
19. Tuttle, M.D., et al., *Solid-state NMR structure of a pathogenic fibril of full-length human alpha-synuclein.* Nat Struct Mol Biol, 2016. **23**(5): p. 409-15.
20. McLean, P.J., et al., *TorsinA and heat shock proteins act as molecular chaperones: suppression of alpha-synuclein aggregation.* Journal of Neurochemistry, 2002. **83**(4): p. 846-854.

21. Lee, D., et al., *alpha-Synuclein exhibits competitive interaction between calmodulin and synthetic membranes.* Journal of Neurochemistry, 2002. **82**(5): p. 1007-1017.
22. Murphy, D.D., et al., *Synucleins are developmentally expressed, and alpha-synuclein regulates the size of the presynaptic vesicular pool in primary hippocampal neurons.* J Neurosci, 2000. **20**(9): p. 3214-20.
23. Madine, J., A.J. Doig, and D.A. Middleton, *A study of the regional effects of alpha-synuclein on the organization and stability of phospholipid bilayers.* Biochemistry, 2006. **45**(18): p. 5783-92.
24. Clayton, D.F. and J.M. George, *Synucleins in synaptic plasticity and neurodegenerative disorders.* J Neurosci Res, 1999. **58**(1): p. 120-9.
25. Polymeropoulos, M.H., et al., *Mutation in the alpha-synuclein gene identified in families with Parkinson's disease.* Science, 1997. **276**(5321): p. 2045-7.
26. Kruger, R., et al., *Ala30Pro mutation in the gene encoding alpha-synuclein in Parkinson's disease.* Nat Genet, 1998. **18**(2): p. 106-8.
27. Plaas, M., et al., *Alpha-synuclein A30P point-mutation generates age-dependent nigrostriatal deficiency in mice.* J Physiol Pharmacol, 2008. **59**(2): p. 205-16.
28. Bartels, T., J.G. Choi, and D.J. Selkoe, *alpha-Synuclein occurs physiologically as a helically folded tetramer that resists aggregation.* Nature, 2011. **477**(7362): p. 107-U123.
29. Fauvet, B., et al., *α-Synuclein in Central Nervous System and from Erythrocytes, Mammalian Cells, and Escherichia coli Exists Predominantly as Disordered Monomer.* Journal of Biological Chemistry, 2012. **287**(19): p. 15345-15364.
30. Theillet, F.-X., et al., *Structural disorder of monomeric α-synuclein persists in mammalian cells.* Nature, 2016. **530**(7588): p. 45-50.
31. Bertoncini, C.W., et al., *Release of long-range tertiary interactions potentiates aggregation of natively unstructured alpha-synuclein.* Proc Natl Acad Sci U S A, 2005. **102**(5): p. 1430-5.
32. Heise, H., et al., *Molecular-level secondary structure, polymorphism, and dynamics of full-length alpha-synuclein fibrils studied by solid-state NMR.* Proc Natl Acad Sci U S A, 2005. **102**(44): p. 15871-6.
33. Bousset, L., et al., *Structural and functional characterization of two alpha-synuclein strains.* Nature Communications, 2013. **4**: p. 13.
34. Tuttle, M.D., et al., *Solid-state NMR structure of a pathogenic fibril of full-length human [alpha]-synuclein.* Nat Struct Mol Biol, 2016. **23**(5): p. 409-415.
35. Hoyer, W., et al., *Structural characterization of alpha-Synuclein amyloids*, in *InThe Prion Phenomena in Neurodegenerative Diseases: New Frontiers in Neuroscience*. 2015, Nova Science Biomedical. p. 111-128.
36. Viegas, A., T. Viennet, and M. Etzkorn, *The power, pitfalls and potential of the nanodisc system for NMR-based studies*, in *Biological Chemistry*. 2016. p. 1335.
37. Viennet, T., et al., *A structural and kinetic link between membrane association and amyloid fibril formation of α-Synuclein.* bioRxiv, 2017.
38. Prusiner, S., *Novel proteinaceous infectious particles cause scrapie.* Science, 1982. **216**(4542): p. 136-144.
39. DePace, A.H., et al., *A critical role for amino-terminal glutamine/asparagine repeats in the formation and propagation of a yeast prion.* Cell, 1998. **93**(7): p. 1241-1252.
40. Glover, J.R., et al., *Self-seeded fibers formed by Sup35, the protein determinant of [PSI+], a heritable prion-like factor of S. cerevisiae.* Cell, 1997. **89**(5): p. 811-9.

41. Paushkin, S.V., et al., *Propagation of the yeast prion-like [psi(+)] determinant is mediated by oligomerization of the SUP35-encoded polypeptide chain release factor.* Embo Journal, 1996. **15**(12): p. 3127-3134.
42. Chernoff, Y.O., S.M. Uptain, and S.L. Lindquist, *Analysis of prion factors in yeast.* Guide to Yeast Genetics and Molecular and Cell Biology, Pt C, 2002. **351**: p. 499-538.
43. Wickner, R.B., et al., *Prion diseases of yeast: amyloid structure and biology.* Semin Cell Dev Biol, 2011. **22**(5): p. 469-75.
44. Shewmaker, F., et al., *Two prion variants of Sup35p have in-register parallel beta-sheet structures, independent of hydration.* Biochemistry, 2009. **48**(23): p. 5074-82.
45. Shewmaker, F., et al., *Amyloids of shuffled prion domains that form prions have a parallel in-register beta-sheet structure.* Biochemistry, 2008. **47**(13): p. 4000-7.
46. Frederick, K.K., et al., *Combining DNP NMR with segmental and specific labeling to study a yeast prion protein strain that is not parallel in-register.* 2017. **114**(14): p. 3642-3647.
47. Tanaka, M., et al., *Conformational variations in an infectious protein determine prion strain differences.* Nature, 2004. **428**(6980): p. 323-8.
48. Tanaka, M., et al., *The physical basis of how prion conformations determine strain phenotypes.* Nature, 2006. **442**(7102): p. 585-589.
49. Ohhashi, Y., et al., *Molecular basis for diversification of yeast prion strain conformation.* Proc Natl Acad Sci U S A, 2018. **115**(10): p. 2389-2394.
50. Punta, M., I. Simon, and Z. Dosztanyi, *Prediction and analysis of intrinsically disordered proteins.* Methods Mol Biol, 2015. **1261**: p. 35-59.
51. Kjaergaard, M., et al., *Temperature-dependent structural changes in intrinsically disordered proteins: Formation of α-helices or loss of polyproline II?* Protein Science : A Publication of the Protein Society, 2010. **19**(8): p. 1555-1564.
52. Receveur-Bréchot, V., et al., *Assessing protein disorder and induced folding.* Proteins: Structure, Function, and Bioinformatics, 2006. **62**(1): p. 24-45.
53. Haas, E., *Ensemble FRET Methods in Studies of Intrinsically Disordered Proteins*, in *Intrinsically Disordered Protein Analysis: Volume 1, Methods and Experimental Tools*, V.N. Uversky and A.K. Dunker, Editors. 2012, Humana Press: Totowa, NJ. p. 467-498.
54. Ozenne, V., et al., *Mapping the potential energy landscape of intrinsically disordered proteins at amino acid resolution.* J Am Chem Soc, 2012. **134**(36): p. 15138-48.
55. Schwalbe, M., et al., *Predictive Atomic Resolution Descriptions of Intrinsically Disordered hTau40 and alpha-Synuclein in Solution from NMR and Small Angle Scattering.* Structure, 2014. **22**(2): p. 238-249.
56. Carballo-Pacheco, M. and B. Strodel, *Comparison of force fields for Alzheimer's A beta42: A case study for intrinsically disordered proteins.* Protein Sci, 2016.
57. Henriques, J., C. Cragnell, and M. Skepo, *Molecular Dynamics Simulations of Intrinsically Disordered Proteins: Force Field Evaluation and Comparison with Experiment.* J Chem Theory Comput, 2015. **11**(7): p. 3420-31.
58. Fisette, O., et al., *Synergistic Applications of MD and NMR for the Study of Biological Systems.* Journal of Biomedicine and Biotechnology, 2012. **2012**: p. 12.
59. Sgourakis, N.G., et al., *The Alzheimer's Peptides Aβ40 and 42 Adopt Distinct Conformations in Water: A Combined MD / NMR Study.* Journal of Molecular Biology, 2007. **368**(5): p. 1448-1457.
60. Concistre, M., et al., *Freezing of Molecular Motions Probed by Cryogenic Magic Angle Spinning NMR.* Journal of Physical Chemistry Letters, 2014. **5**(3): p. 512-516.

61. Heise, H., et al., *Probing conformational disorder in neurotensin by two-dimensional solid-state NMR and comparison to molecular dynamics simulations.* Biophysical Journal, 2005. **89**(3): p. 2113-2120.
62. Havlin, R.H. and R. Tycko, *Probing site-specific conformational distributions in protein folding with solid-state NMR.* Proceedings of the National Academy of Sciences of the United States of America, 2005. **102**(9): p. 3284-3289.
63. Siemer, A.B., K.Y. Huang, and A.E. McDermott, *Protein Linewidth and Solvent Dynamics in Frozen Solution NMR.* Plos One, 2012. **7**(10).
64. Carver, T.R. and C.P. Slichter, *Polarization of Nuclear Spins in Metals.* Physical Review, 1953. **92**(1): p. 212-213.
65. Overhauser, A.W., *Polarization of Nuclei in Metals.* Physical Review, 1953. **92**(2): p. 411-415.
66. Uluca, B., et al., *DNP-Enhanced MAS NMR: A Tool to Snapshot Conformational Ensembles of alpha-Synuclein in Different States.* Biophys J, 2018. **114**(7): p. 1614-1623.
67. Tycko, R., *Molecular structure of amyloid fibrils: insights from solid-state NMR.* Quarterly Reviews of Biophysics, 2006. **39**(1): p. 1-55.
68. Heise, H., *Solid-state NMR spectroscopy of amyloid proteins.* Chembiochem, 2008. **9**(2): p. 179-89.
69. Thompson, L.K., *Unraveling the secrets of Alzheimer's beta-amyloid fibrils.* Proceedings of the National Academy of Sciences of the United States of America, 2003. **100**(2): p. 383-385.
70. Opella, S.J., *Solid-state NMR and membrane proteins.* Journal of Magnetic Resonance, 2015. **253**: p. 129-137.
71. Ward, M.E., L.S. Brown, and V. Ladizhansky, *Advanced solid-state NMR techniques for characterization of membrane protein structure and dynamics: Application to Anabaena Sensory Rhodopsin.* Journal of Magnetic Resonance, 2015. **253**: p. 119-128.
72. Colvin, M.T., et al., *Atomic Resolution Structure of Monomorphic A beta(42) Amyloid Fibrils.* Journal of the American Chemical Society, 2016. **138**(30): p. 9663-9674.
73. Gath, J., et al., *Yet another polymorph of alpha-synuclein: solid-state sequential assignments.* Biomolecular Nmr Assignments, 2014. **8**(2): p. 395-404.
74. Baxa, U., et al., *Characterization of beta-sheet structure in Ure2p1-89 yeast prion fibrils by solid-state nuclear magnetic resonance.* Biochemistry, 2007. **46**(45): p. 13149-62.
75. Kryndushkin, D.S., R.B. Wickner, and R. Tycko, *The core of Ure2p prion fibrils is formed by the N-terminal segment in a parallel cross-beta structure: evidence from solid-state NMR.* J Mol Biol, 2011. **409**(2): p. 263-77.
76. Wickholm, K., P.T. Larsson, and T. Iversen, *Assignment of non-crystalline forms in cellulose I by CP/MAS 13C NMR spectroscopy.* Carbohydrate Research, 1998. **312**(3): p. 123-129.
77. Mainz, A., et al., *The chaperone alpha B-crystallin uses different interfaces to capture an amorphous and an amyloid client.* Nature Structural & Molecular Biology, 2015. **22**(11): p. 898-905.
78. Akbey, Ü., et al., *Solid-State NMR investigations of anhydrous proton-conducting acid–base poly(acrylic acid)– poly(4-vinyl pyridine) polymer blend system: A study of hydrogen bonding and proton conduction.* Journal of Polymer Science Part B: Polymer Physics, 2009. **47**(2): p. 138-155.
79. Bauer, T., et al., *Line-Broadening in Low-Temperature Solid-State NMR Spectra of Fibrils.* J Biomol NMR, 2017. **67**(1): p. 51-61.

80. Duer, M.J., *The Basics of Solid-State NMR*, in *Solid-State NMR Spectroscopy Principles and Applications*. 2007, Blackwell Science Ltd. p. 1-72.
81. Andrew, E.R., A. Bradbury, and R.G. Eades, *Nuclear Magnetic Resonance Spectra from a Crystal rotated at High Speed.* Nature, 1958. **182**(4650): p. 1659-1659.
82. Tycko, R. and S.O. Smith, *Symmetry Principles in the Design of Pulse Sequences for Structural Measurements in Magic Angle Spinning Nuclear-Magnetic-Resonance.* Journal of Chemical Physics, 1993. **98**(2): p. 932-943.
83. Raleigh, D.P., M.H. Levitt, and R.G. Griffin, *Rotational resonance in solid state NMR.* Chemical Physics Letters, 1988. **146**(1–2): p. 71-76.
84. Ishii, Y., *13C–13C dipolar recoupling under very fast magic angle spinning in solid-state nuclear magnetic resonance: Applications to distance measurements, spectral assignments, and high-throughput secondary-structure determination.* The Journal of Chemical Physics, 2001. **114**(19): p. 8473-8483.
85. Gullion, T. and J. Schaefer, *Detection of Weak Heteronuclear Dipolar Coupling by Rotational-Echo Double-Resonance Nuclear-Magnetic-Resonance.* Advances in Magnetic Resonance, Vol 13, 1989. **13**: p. 57-83.
86. Gullion, T. and J. Schaefer, *Rotational-Echo Double-Resonance Nmr.* Journal of Magnetic Resonance, 1989. **81**(1): p. 196-200.
87. Takegoshi, K., S. Nakamura, and T. Terao, *C-13-H-1 dipolar-assisted rotational resonance in magic-angle spinning NMR.* Chemical Physics Letters, 2001. **344**(5-6): p. 631-637.
88. Morcombe, C.R., et al., *Diluting abundant spins by isotope edited radio frequency field assisted diffusion.* Journal of the American Chemical Society, 2004. **126**(23): p. 7196-7197.
89. Tycko, R. and G. Dabbagh, *Measurement of Nuclear Magnetic Dipole-Dipole Couplings in Magic Angle Spinning Nmr.* Chemical Physics Letters, 1990. **173**(5-6): p. 461-465.
90. Raleigh, D.P., M.H. Levitt, and R.G. Griffin, *Rotational Resonance in Solid-State Nmr.* Chemical Physics Letters, 1988. **146**(1-2): p. 71-76.
91. Gregory, D.M., et al., *Windowless Dipolar Recoupling - the Detection of Weak Dipolar Couplings between Spin-1/2 Nuclei with Large Chemical-Shift Anisotropies.* Chemical Physics Letters, 1995. **246**(6): p. 654-663.
92. Beumer, C., et al., *Chapter 10 Isotopically Enriched Systems*, in *Modern Methods in Solid-state NMR: A Practitioner's Guide*. 2018, The Royal Society of Chemistry. p. 289-321.
93. Tycko, R., *Symmetry-based constant-time homonuclear dipolar recoupling in solid state NMR.* J Chem Phys, 2007. **126**(6): p. 064506.
94. Shewmaker, F., et al., *The functional curli amyloid is not based on in-register parallel beta-sheet structure.* J Biol Chem, 2009. **284**(37): p. 25065-76.
95. Shewmaker, F., R.B. Wickner, and R. Tycko, *Amyloid of the prion domain of Sup35p has an in-register parallel beta-sheet structure.* Proceedings of the National Academy of Sciences of the United States of America, 2006. **103**(52): p. 19754-19759.
96. Bennett, A.E., et al., *Chemical-Shift Correlation Spectroscopy in Rotating Solids - Radio Frequency-Driven Dipolar Recoupling and Longitudinal Exchange.* Journal of Chemical Physics, 1992. **96**(11): p. 8624-8627.
97. Bak, M., J.T. Rasmussen, and N.C. Nielsen, *SIMPSON: A general simulation program for solid-state NMR spectroscopy.* Journal of Magnetic Resonance, 2000. **147**(2): p. 296-330.
98. Smith, S.A., et al., *Computer Simulations in Magnetic Resonance. An Object-Oriented Programming Approach.* Journal of Magnetic Resonance, Series A, 1994. **106**(1): p. 75-105.

99. Veshtort, M. and R.G. Griffin, *SPINEVOLUTION: a powerful tool for the simulation of solid and liquid state NMR experiments.* J Magn Reson, 2006. **178**(2): p. 248-82.
100. Merrifield, R.B., *Solid-phase peptide synthesis.* Adv Enzymol Relat Areas Mol Biol, 1969. **32**: p. 221-96.
101. Shelton, P.T. and K.J. Jensen, *Linkers, Resins, and General Procedures for Solid-Phase Peptide Synthesis*, in *Peptide Synthesis and Applications*, K.J. Jensen, P. Tofteng Shelton, and S.L. Pedersen, Editors. 2013, Humana Press: Totowa, NJ. p. 23-41.
102. Abdine, A., M.A. Verhoeven, and D.E. Warschawski, *Cell-free expression and labeling strategies for a new decade in solid-state NMR.* New Biotechnology, 2011. **28**(3): p. 272-276.
103. Lundstrom, P., et al., *Fractional 13C enrichment of isolated carbons using [1-13C]- or [2-13C]-glucose facilitates the accurate measurement of dynamics at backbone Calpha and side-chain methyl positions in proteins.* J Biomol NMR, 2007. **38**(3): p. 199-212.
104. Verardi, R., et al., *Isotope Labeling for Solution and Solid-State NMR Spectroscopy of Membrane Proteins*, in *Isotope labeling in Biomolecular NMR*, H.S. Atreya, Editor. 2012, Springer Netherlands: Dordrecht. p. 35-62.
105. Hong, M. and K. Jakes, *Selective and extensive 13C labeling of a membrane protein for solid-state NMR investigations.* J Biomol NMR, 1999. **14**(1): p. 71-4.
106. Pines, A., M.G. Gibby, and J.S. Waugh, *Proton-Enhanced Nmr of Dilute Spins in Solids.* Journal of Chemical Physics, 1973. **59**(2): p. 569-590.
107. Morris, G.A. and R. Freeman, *Enhancement of Nuclear Magnetic-Resonance Signals by Polarization Transfer.* Journal of the American Chemical Society, 1979. **101**(3): p. 760-762.
108. Bouchiat, M.A., T.R. Carver, and C.M. Varnum, *Nuclear Polarization in He-3 Gas Induced by Optical Pumping and Dipolar Exchange.* Physical Review Letters, 1960. **5**(8): p. 373-375.
109. Bowers, C.R. and D.P. Weitekamp, *Transformation of Symmetrization Order to Nuclear-Spin Magnetization by Chemical-Reaction and Nuclear-Magnetic-Resonance.* Physical Review Letters, 1986. **57**(21): p. 2645-2648.
110. Daviso, E., et al., *A 10 000-fold Nuclear Hyperpolarization of a Membrane Protein in the Liquid Phase via Solid-State Mechanism.* Journal of the American Chemical Society, 2011. **133**(42): p. 16754-16757.
111. Closs, G.L. and L.E. Closs, *Induced Dynamic Nuclear Spin Polarization in Photoreductions of Benzophenone by Toluene and Ethylbenzene.* Journal of the American Chemical Society, 1969. **91**(16): p. 4549-4550.
112. Weis, V., et al., *Solid effect in the electron spin dressed state: A new approach for dynamic nuclear polarization.* Journal of Chemical Physics, 2000. **113**(16): p. 6795-6802.
113. Loening, N.M., et al., *Solution-state dynamic nuclear polarization at high magnetic field.* Journal of the American Chemical Society, 2002. **124**(30): p. 8808-8809.
114. Weis, V. and R.G. Griffin, *Electron-nuclear cross polarization.* Solid State Nuclear Magnetic Resonance, 2006. **29**(1-3): p. 66-78.
115. Griesinger, C., et al., *Dynamic nuclear polarization at high magnetic fields in liquids.* Progress in Nuclear Magnetic Resonance Spectroscopy, 2012. **64**: p. 4-28.
116. Turke, M.-T. and M. Bennati, *Saturation factor of nitroxide radicals in liquid DNP by pulsed ELDOR experiments.* Physical Chemistry Chemical Physics, 2011. **13**(9): p. 3630-3633.
117. Türke, M.T. and M. Bennati, *Comparison of Overhauser DNP at 0.34 and 3.4 T with Frémy's Salt.* Applied Magnetic Resonance, 2012. **43**(1-2): p. 129-138.
118. van Bentum, J., et al., *Perspectives on DNP-enhanced NMR spectroscopy in solutions.* Journal of Magnetic Resonance, 2016. **264**: p. 59-67.

119. Hovav, Y., A. Feintuch, and S. Vega, *Theoretical aspects of dynamic nuclear polarization in the solid state - The solid effect.* Journal of Magnetic Resonance, 2010. **207**(2): p. 176-189.
120. McDermott, A.E. and T. Polenova, *Solid State NMR Studies of Biopolymers*. 2012: John Wiley & Sons.
121. Maly, T., et al., *H-2-DNP-enhanced H-2-C-13 solid-state NMR correlation spectroscopy.* Physical Chemistry Chemical Physics, 2010. **12**(22): p. 5872-5878.
122. Jeffries, C.D., *Polarization of Nuclei by Resonance Saturation in Paramagnetic Crystals.* Physical Review, 1957. **106**(1): p. 164-165.
123. Wiśniewski, D., et al., *Solid effect DNP polarization dynamics in a system of many spins.* Journal of Magnetic Resonance, 2016. **264**: p. 30-38.
124. Lee, D., S. Hediger, and G. De Paëpe, *Is solid-state NMR enhanced by dynamic nuclear polarization?* Solid State Nuclear Magnetic Resonance, 2015. **66–67**: p. 6-20.
125. Rosay, M., et al., *Solid-state dynamic nuclear polarization at 263 GHz: spectrometer design and experimental results.* Physical Chemistry Chemical Physics, 2010. **12**(22): p. 5850-5860.
126. Thurber, K.R. and R. Tycko, *Theory for cross effect dynamic nuclear polarization under magic-angle spinning in solid state nuclear magnetic resonance: The importance of level crossings.* Journal of Chemical Physics, 2012. **137**(8).
127. Mentink-Vigier, F., et al., *Fast passage dynamic nuclear polarization on rotating solids.* Journal of Magnetic Resonance, 2012. **224**: p. 13-21.
128. Maly, T., et al., *Dynamic nuclear polarization at high magnetic fields.* Journal of Chemical Physics, 2008. **128**(5).
129. Kuhn, L.T. and Ü. Akbey, *Hyperpolarization methods in NMR spectroscopy*. Vol. 338. 2013: Springer.
130. Hu, K.N., et al., *Dynamic nuclear polarization with biradicals.* Journal of the American Chemical Society, 2004. **126**(35): p. 10844-10845.
131. Siaw, T.A., et al., *A versatile and modular quasi optics-based 200 GHz dual dynamic nuclear polarization and electron paramagnetic resonance instrument.* Journal of Magnetic Resonance, 2016. **264**: p. 131-153.
132. Borghini, M., *Spin-Temperature Model of Nuclear Dynamic Polarization Using Free Radicals.* Physical Review Letters, 1968. **20**(9): p. 419-&.
133. Abragam, A. and M. Goldman, *Nuclear magnetism : order and disorder*. The International series of monographs on physics. 1982, Oxford: New York: Clarendon Press ; Oxford University Press.
134. Serra, S.C., A. Rosso, and F. Tedoldi, *On the role of electron-nucleus contact and microwave saturation in thermal mixing DNP.* Physical Chemistry Chemical Physics, 2013. **15**(21): p. 8416-8428.
135. Song, C.S., et al., *TOTAPOL: A biradical polarizing agent for dynamic nuclear polarization experiments in aqueous media.* Journal of the American Chemical Society, 2006. **128**(35): p. 11385-11390.
136. Akbey, U., et al., *Dynamic nuclear polarization of deuterated proteins.* Angew Chem Int Ed Engl, 2010. **49**(42): p. 7803-6.
137. Fricke, P., et al., *Studies on the MxiH protein in T3SS needles using DNP-enhanced ssNMR spectroscopy.* Chemphyschem, 2014. **15**(1): p. 57-60.
138. Viennet, T., et al., *Selective Protein Hyperpolarization in Cell Lysates Using Targeted Dynamic Nuclear Polarization.* Angew Chem Int Ed Engl, 2016. **55**(36): p. 10746-50.

139. Sauvée, C., et al., *Highly Efficient, Water-Soluble Polarizing Agents for Dynamic Nuclear Polarization at High Frequency.* Angewandte Chemie, 2013. **125**(41): p. 11058-11061.
140. Liao, S.Y., et al., *Efficient DNP NMR of membrane proteins: sample preparation protocols, sensitivity, and radical location.* J Biomol NMR, 2016. **64**(3): p. 223-37.
141. Lange, S., et al., *The effect of biradical concentration on the performance of DNP-MAS-NMR.* Journal of Magnetic Resonance, 2012. **216**: p. 209-212.
142. Tycko, R., *NMR at Low and Ultralow Temperatures.* Accounts of Chemical Research, 2013. **46**(9): p. 1923-1932.
143. Stansfield, I., et al., *The products of the SUP45 (eRF1) and SUP35 genes interact to mediate translation termination in Saccharomyces cerevisiae.* EMBO J, 1995. **14**(17): p. 4365-73.

Acknowledgements

There are a number of people who helped me during this 3,5 years of my Ph.D. life. For me, it was not only an ordinary education life in addition to that I gain a lot experiences both in science and life with the help of very nice people. Firstly, I thank my advisor Professor Henrike Heise for her guidance and for allowing me the opportunity to work with some of the best solid-state NMR spectrometers in the world. Thank you for giving me a lot of freedom in this research project. All members of the Heise group have contributed to my personal and professional growth during this time. I am especially grateful to Franziska Weirich who helped me a lot in my first abroad experience, away from Istanbul. She was source of my motivation all the time I need. I also appreciate very much the good companionship with other members of the group Claudia Beumer, Anna König, Daniel Schölzel, Hohom Pei and Timo Piechatzek. Thanks all of them for awesome dinners, BBQ, and knitting night. Special thanks to all for spending my birthday with me and I never feel alone in Germany on this special day. I also really enjoy the time at GDCh, EUROMAR and research school which we have joined together.

For introducing me protein expression and purification world I am deeply thankful to Wolfgang Hoyer and Hamed Shaykhalishahi. I would like to thank Manuel Etzkorn and Thibault Viennet for their nice discussion and collaboration. I also would like to thank Dusan Petrovic for his nice friendship since IHRS of Biosoft 2013.

I would like to thank everyone at the NMR Facility at the Research Center especially Rudolf Hartmann for dealing with all the problems I couldn't figure out. Especially, thank you for teaching the TOPSIN and helping to reconnect the probehead. You always have an open door for all cases, even technical issues in my house. I learned a lot from you about being a good colleague.

I would like to acknowledge Hatice Sasioglu and Hanife Karakas for being my family in Jülich. Thanks for being present in my life.

Finally, I thank my family for love, support, and understanding. Thanks for letting me choose my own way and follow the science. My parents, HANIM and HASARI ULUCA raised me to believe that I could achieve anything I set in my mind. This thesis is dedicated to them.

Eidesstattliche Erklärung

Ich versichere an Eides Statt, dass die Dissertation von mir selbständig und ohne unzulässige fremde Hilfe unter Beachtung der „Grundsätze zur Sicherung guter wissenschaftlicher Praxis an der Heinrich-Heine-Universität Düsseldorf" erstellt worden ist.

Ferner erkläre ich, dass ich in keinem anderen Dissertationsverfahren mit oder ohne Erfolg versucht habe, diese Dissertation einzureichen.

Declaration

I do solemnly declare that my thesis is presentation of original research performed according to the "Principles of Good Scientific Practice" set out by Heinrich-Heine University of Düsseldorf. This thesis does not contain the data already published in public domain and it has never been submitted or accepted by any other institutions for the award of any other degrees.

Düsseldorf, 21.07.2017

Boran ULUCA

COMMUNICATIONS BIOLOGY

ARTICLE

DOI: 10.1038/s42003-018-0049-z OPEN

Structural insights from lipid-bilayer nanodiscs link α-Synuclein membrane-binding modes to amyloid fibril formation

Thibault Viennet [1,2], Michael M. Wördehoff [1], Boran Uluca[1,2], Chetan Poojari [2,3,4], Hamed Shaykhalishahi[1], Dieter Willbold [1,2], Birgit Strodel [2], Henrike Heise [1,2], Alexander K. Buell [1], Wolfgang Hoyer [1,2] & Manuel Etzkorn [1,2]

The protein α-Synuclein (αS) is linked to Parkinson's disease through its abnormal aggregation, which is thought to involve cytosolic and membrane-bound forms of αS. Following previous studies using micelles and vesicles, we present a comprehensive study of αS interaction with phospholipid bilayer nanodiscs. Using a combination of NMR-spectroscopic, biophysical, and computational methods, we structurally and kinetically characterize αS interaction with different membrane discs in a quantitative and site-resolved way. We obtain global and residue-specific αS membrane affinities, and determine modulations of αS membrane binding due to αS acetylation, membrane plasticity, lipid charge density, and accessible membrane surface area, as well as the consequences of the different binding modes for αS amyloid fibril formation. Our results establish a structural and kinetic link between the observed dissimilar binding modes and either aggregation-inhibiting properties, largely unperturbed aggregation, or accelerated aggregation due to membrane-assisted fibril nucleation.

[1] Institute of Physical Biology, Heinrich-Heine-University, Universitätsstrasse 1, 40225 Düsseldorf, Germany. [2] Instititue of Complex Systems (ICS-6), Forschungszentrum Jülich, Wilhelm-Johnen-Strasse, 52428 Jülich, Germany. [3] Department of Physics, Tampere University of Technology, Korkeakoulunkatu 10, 33720 Tampere, Finland. [4] Department of Physics, University of Helsinki, Gustaf Hällströmin katu 2a, 00560 Helsinki, Finland. Correspondence and requests for materials should be addressed to M.E. (email: manuel.etzkorn@hhu.de)

The protein α-Synuclein (αS) is associated with various synucleinopathies including Parkinson's disease through its abnormal aggregation, fibril formation, and formation of Lewy bodies[1–4]. Although its exact native function is not yet fully understood, αS is found in synaptic vesicles and supposed to be involved in membrane interactions, e.g., in synaptic vesicle homeostasis[5,6] and SNARE-like vesicle-to-vesicle or vesicle-to-membrane fusion[7,8]. Membrane association of αS has been shown to modulate its aggregation propensity[9,10] and αS oligomeric species have been proposed to be the toxic species in Parkinson's disease, especially through membrane pore formation mechanisms[11,12]. Notably, αS has been shown to be specifically acetylated at its N-terminus, which is thought to act as an important mode of regulation of protein–membrane association[13,14].

Previous data recorded using micelle and vesicle preparations already provided valuable information of the αS–membrane interactions, including binding and lipid specificity[15–18], effect of mutations on membrane association[8,19], micelle-bound structure[20], vesicle-bound structural insights[21–23], and conformational dynamics[8,23,24]. Two structural models of lipid-bound αS were proposed, i.e., the "extended helix" consisting of one roughly 100-residue-long α-helix[25] and the "horse-shoe" consisting of two helices with different lipid affinities separated by a kink at residues 42–44[26]. Furthermore, various effects of lipids for αS aggregation were reported including inhibition of aggregation[27], triggering of fibrillation[28,29], and modification of fibril structure[29]. Membrane binding and its effect on aggregation have been shown to be strongly dependent on chemical properties of the lipids including head group charge content[26] and fatty acid type[30].

Although the phospholipid bilayer nanodisc (NDs) system[31] does not fully resemble the physiological properties of synaptic vesicle membranes in all aspects (e.g., absence of curvature and integral membrane proteins), it offers the potential to provide additional insights that are complementary to the information obtained, e.g., on micelles or liposome preparations. Notably, NDs have been used before to study the effect of calcium ions on the membrane interaction of αS[32], as well as lipid and monomer specificity of the Alzheimer-associated Aβ peptide[33]. In general, NDs are very homogeneous, stable in a wide buffer range[34], and allow the preparations of well-defined lipid mixtures with an accurate estimate of the bilayer size[35], charge[36], and lipid molarity[37]. The increased stability may, e.g., offer the possibility to determine the interaction with a stable planar bilayer surface. In contrast, it is known for small unilamellar vesicles (SUVs) that the interaction with αS can considerably and rapidly change the lipid environment (e.g., from homogeneous SUVs to rather heterogeneous particles[8,38–40]). In addition, the smaller size of the NDs should, in theory, allow the detection of the lipid-bound state using suitable solution nuclear magnetic resonance (NMR) techniques[34,41,42]. In general, the well-defined size and lipid composition of NDs, paired with their accessibility, homogeneity, and stability should permit unique quantitative insights into αS membrane association and its role in aggregation.

Here we explore this potential and report on a comprehensive NMR investigation of the effects of lipid charge, bilayer fluidity, and αS N-terminal acetylation on the structural aspects of αS membrane association. We corroborate these insights with molecular dynamics (MD) simulations and a series of complementary biophysical measurements to further characterize membrane plasticity, global affinities, as well as binding and aggregation kinetics. Based on this data we correlate structural insights, such as residue-specific affinities and competition for accessible membrane surface area, to their potential role in modulating αS aggregation properties. Our study provides insights into (i) the different lipid binding modes of αS to stable planar bilayers of defined lipid quantity and composition, (ii) the effect of membrane plasticity for αS binding, (iii) the modulation of membrane plasticity through αS, and (iv) the connection between binding modes and their effect on αS aggregation. In addition, it gives an initial estimate of the number of lipid molecules and of lipid-associated αS molecules that are required to induce fibril nucleation, and allows to develop a basic structural and kinetic model of the modulation of αS aggregation through its interaction with different membrane surfaces. Our in vitro data help to better understand the molecular determinants of αS–membrane association and may point to possible in vivo implications in the context of Parkinson's disease.

Results

αS membrane-modulated aggregation due to lipid charge. To obtain residue-specific insights into the interaction of αS with lipid bilayer NDs of various composition, we recorded a series of solution NMR two-dimensional transverse relaxation optimized spectroscopy (TROSY)-heteronuclear single quantum coherence (HSQC) spectra keeping a molar ratio of one αS molecule per membrane leaflet (Fig. 1a). In the presence of NDs containing only 1,2-dimyristoyl-*sn*-glycero-3-phosphocholine (DMPC) lipids, no differences to the spectrum of αS in the absence of NDs were detected (Fig. 1a–c, black). This finding shows that αS does not interact with the membrane scaffold protein and provides additional evidence that αS does not interact with non-charged lipid bilayers. In a similar way as reported previously using liposomes[26,43], we further tested the influence of increasing amounts of negatively charged lipid head groups on αS membrane association (Fig. 1a–c). It is noteworthy that lipid ratios and proper mixing of the different lipid types inside the NDs were also verified by NMR spectroscopy (Supplementary Fig. 1a). When increasing the content of the negatively charged lipid 1-palmitoyl-2-oleoyl-sn-glycero-3-phospho-(1′-rac-glycerol) (POPG) our NMR data show a gradually increasing bilayer interaction of αS, as evident by a residue-specific decrease in the ratio of NMR signals in the presence and absence of NDs. This NMR attenuation profile divides the protein into rather distinct regions with different membrane-binding behaviors (Fig. 1b, c). The first region spans the N-terminal residues 1–38, which are already weakly interacting at 25% content of negatively charged lipids and strongly interact at 50% (or higher) charge content. A comparison between αS that is acetylated at its N-terminus (Fig. 1b) and non-acetylated αS (Fig. 1c) shows that, in particular at lower anionic lipid content the N-terminus does interact stronger with the membrane when it is acetylated, which is in line with previous data observed on SUVs[14]. While we recorded most data for both αS forms, unless otherwise stated, only data obtained on the more physiologically relevant acetylated αS will be shown in the following. Data recorded on non-acetylated αS along with a more detailed discussion can be found in the Supplementary Information (Supplementary Fig. 2).

At 50% charge content, the region comprising residues 38–60 also gradually starts to interact. Amino acids 60–98, corresponding approximately to the aggregation-prone non-amyloid-β component (NAC region), display some interactions with membranes containing 75% anionic lipids and strongly interact at 100% anionic lipid content. The 98–120 region is (partly) affected by 100% net charge content only. Finally, the last 20 C-terminal residues never show any membrane interaction (see Fig. 1d for a model of the different binding modes). This data is largely in line with a predominantly electrostatic model[44] (the first 60 residues displaying a net positive charge, the last 40 residues a net negative charge, and the NAC region being mostly

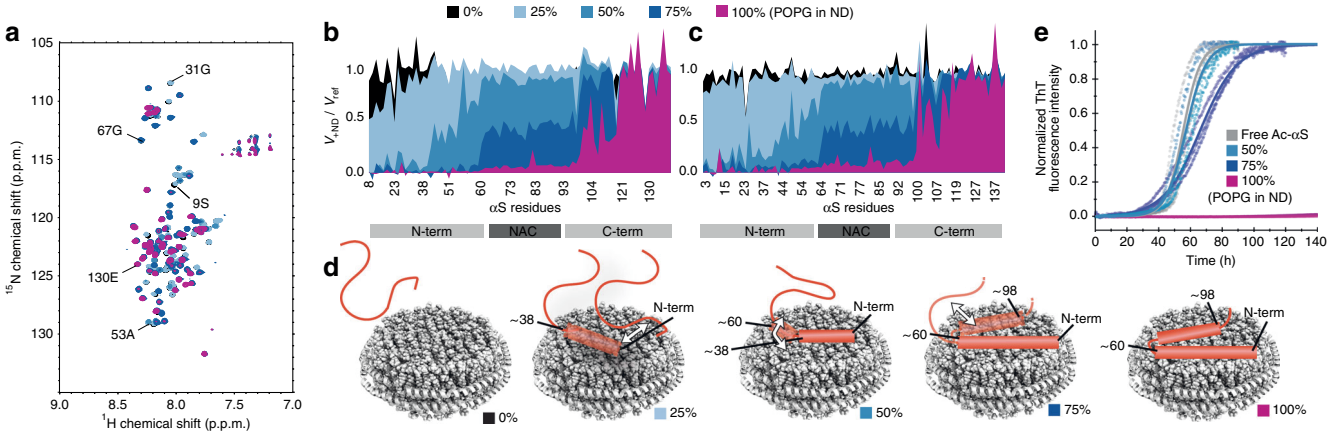

Fig. 1 Lipid charge content modulates αS membrane binding modes and different binding modes show different effects on αS aggregation. **a** NMR [^{15}N-^{1}H]-TROSY-HSQC spectra of [^{15}N]-αS (50 μM) in the absence (gray) or in the presence of 25 μM NDs containing an increasing amount of the anionic lipid POPG complemented with the zwitterionic lipid DMPC (0% POPG (black), 25% POPG (light blue), 50% POPG (blue), 75% POPG (dark blue), and 100% POPG (purple)). Selected residue assignments corresponding to differently affected parts of αS are indicated. Corresponding NMR attenuation profiles, i.e., the ratio of peak volumes in the presence and absence of NDs, are plotted against αS primary sequence for acetylated **b** and non-acetylated **c** αS. **d** Molecular model visualizing the gradual binding of different parts of αS to NDs with increasing charge content. White arrows and transparent coloring indicate αS regions that experience intermediate NMR-signal attenuation indicative of multiple (dynamic or static) states. **e** αS aggregation assays (normalized ThT fluorescence) in the absence and presence of NDs with indicated POPG content for acetylated αS (concentration of αS and NDs identical to NMR data in **a**–**c**, data of triplicate measurements until reaching saturation and their respective fits are shown, color code as in **a**–**c**)

hydrophobic), as well as the three regions dynamic model reported before using SUVs[23].

Interestingly, a comparison with the previously published data on SUVs that observe similar negative charge-dependent binding modes for vesicle-bound αS using electron paramagnetic resonance (EPR) and NMR[26,45], suggests that factors such as membrane curvature, potential instability of liposomes, or the physical borders introduced by the scaffold proteins, which should prevent formation of a fully extended αS α-helix on the membrane surface, do not have a large effect on the detected αS membrane association (see below for more detailed discussion on binding modes; also see Supplementary Note 1 for more detailed discussion on NDs stability).

Using Thioflavin T (ThT) fluorescence as a reporter for fibril formation, we also measured aggregation kinetics of αS in the absence and presence of the different ND compositions (Fig. 1e). These aggregation assays were recorded using identical protein and ND concentrations, as well as buffer conditions as used for the NMR measurements, facilitating a direct comparison between membrane-binding modes and their consequences for protein aggregation. It is noteworthy that, unless stated otherwise, an aggregation assay setup was chosen that mainly reports on the consequences of ND interactions with the lipid-independent aggregation pathway of αS[46–49] (see Methods for more details).

Interestingly, despite the fact that the NMR data show interaction, the presence of NDs up to an anionic lipid content of 50% does not appear to affect aggregation kinetics of acetylated αS. When increasing the negative charge content to 75%, the aggregation half-time slightly increases (Fig. 1e, dark blue) and a strong aggregation-inhibiting effect is detected in the presence of NDs with 100% anionic lipids (Fig. 1e, purple). A comparison of the ThT kinetic data with the NMR-detected modes of αS binding to membranes of different charge contents allows to link molecular determinants of membrane association to their possible effects on αS aggregation. One of the most striking connections is that αS interaction with NDs comprising up to 50% negatively charged lipids does not involve the NAC region, and that under the same conditions no detectable effect on the aggregation behavior of (acetylated) αS is found in ThT assays. When further increasing the charge density above 50% negatively charged lipids, NMR data show first a partial (75% POPG, Fig. 1a–c, dark blue) and then a full (100% POPG, Fig. 1a–c, purple) signal attenuation of the NAC region. This membrane interaction of the NAC region correlates with a slight inhibitory effect of the 75% charged NDs on αS aggregation (Fig. 1e dark blue) and a very strong inhibitory effect of 100% charged NDs (Fig. 1e, purple). Therefore, our data strongly suggest that for the tested conditions (high anionic lipid content and high lipid-to-αS ratios) membrane association of the NAC region protects αS from aggregation.

The ND-bound state of αS. It is noteworthy that, despite possible in principle[34], we could not detect the ND-bound conformation of αS by solution NMR (see Supplementary Fig. 3 and Supplementary Note 2 for more detailed discussion). In order to still gain insight into the conformation of αS bound to NDs, we used magic angle spinning solid-state NMR. Moreover, we took advantage of the very low temperatures (100 K) used in dynamic nuclear polarization (DNP) to additionally eliminate exchange processes and to increase the sensitivity of the experiment. To avoid problems of signal overlap arising from severe inhomogeneous line broadening often seen in this range of temperatures[50], we used a sparse isotope labeling scheme[51], leading to the simplification of ^{13}C–^{13}C spectra to secondary structure-sensitive Cα–Cβ cross-correlations of valines (and leucine Cβ–Cγ). Notably, according to the αS primary sequence and our solution NMR observations (Fig. 1a–c), 95% of the valine residues (i.e., 18 out of the 19) should be membrane bound at the used charge content (100%) and αS-to-ND ratio (1:2). Although in the absence of NDs the DNP ^{13}C–^{13}C spectrum shows a continuous distribution of the valine Cα–Cβ cross-peaks reflecting the carbon chemical shifts of the allowed Ramachandran space (expected for an intrinsically disordered protein such as αS, see Fig. 2, black), a very strong peak shift to a defined chemical shift range typical for α-helical structure is visible after addition of NDs (Fig. 2, purple). The DNP data thus show that αS binds the NDs in α-helical

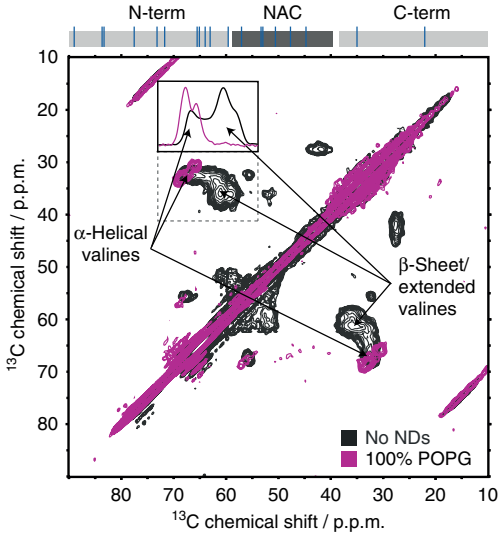

Fig. 2 Nanodiscs binding induces α-helical structure in αS. [^{13}C-^{13}C]-Proton driven spin diffusion magic angle spinning-DNP spectra of free non-acetylated αS in frozen solution (black) and when bound to NDs with 100% POPG lipids (purple). Selective isotope labeling was used to specifically monitor valine Cα-Cβ chemical shift distributions. Peak positions indicative of β-sheet and α-helical secondary structure are labelled. The insert shows normalized 1D projections of the highlighted region (dashed square) in the absence (black) and presence of 100% POPG NDs. Signal deconvolution of these spectra reveals that about 92% of the valines are in an α-helical configuration in the presence of 100% POPG NDs. The occurrence of valine residues in the αS sequence is shown on top (blue lines). According to the respective solution NMR attenuation profile (Fig. 1c, purple) 18 out of 19 valines (i.e., 94.7%) are expected in the membrane-bound state at the used conditions

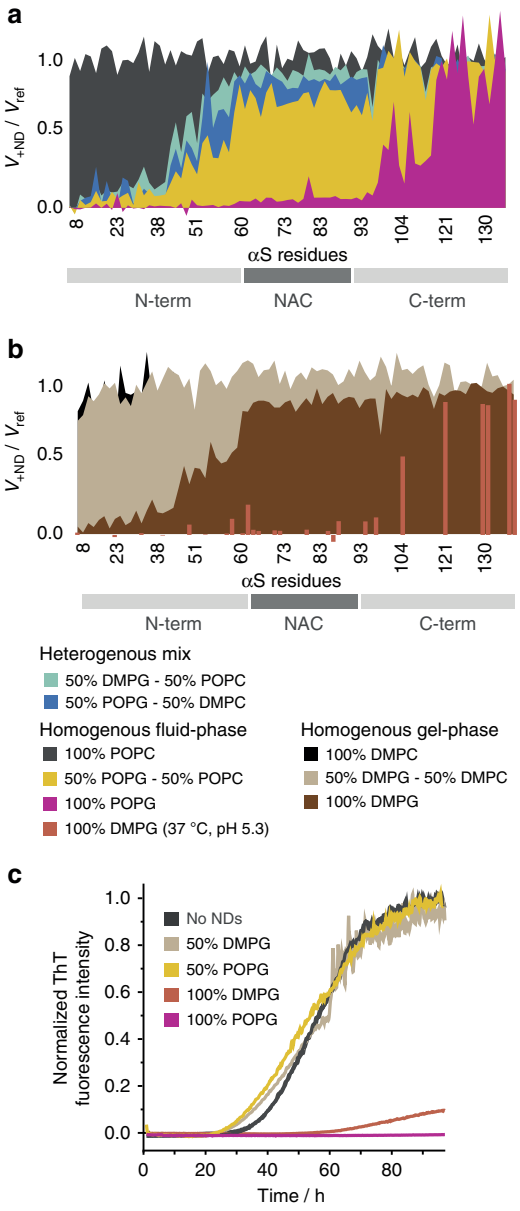

Fig. 3 αS–lipid interaction is favored by increased membrane plasticity. [^{15}N]-αS (50 μM) NMR attenuation profiles in the presence of 25 μM NDs with indicated lipid composition (molar ratio 2:1, αS-to-NDs) for bilayers that are in a more fluid **a** or gel phase **b** at 10 °C. It is noteworthy that all NMR data are recorded at 10 °C and pH 7.4 with the exception of one of the 100% DMPG samples (**b**, red bars) that was recorded at 37 °C and pH 5.3. **c** Corresponding ThT aggregation assays (50 μM αS, 25 μM NDs) for selected conditions (for better visibility only the mean values of triplicate measurements are shown, colors correspond to respective attenuation profiles in **a**, **b**)

conformation corroborating previous studies using circular dichroism (CD) spectroscopy of vesicles, solution NMR spectroscopy of detergents micelles, and solid-state NMR spectroscopy of SUVs[20,23,29]. Interestingly, in contrast to SUVs the lipid bilayer of the NDs system does have a defined edge that can act as physical barrier for the αS membrane interactions. Geometrical considerations suggest that a fully extended α-helix with about 60 residues will completely span the diameter of one ND. Therefore, either the formation of a significantly bent helix (parallel to the membrane scaffold proteins) or at least one kink in the helix is compulsory for the largest observed ND-binding modes. The presence of rather defined steps in the NMR attenuation profiles for 50% and 75% POPG content (Fig. 1b, c) would be in line with the latter and could indicate possible kink positions (as visualized in Fig. 1d). The high similarity to the previously reported SUV-binding modes suggest that αS, in a similar manner as the so-called "horse-shoe" model[22], has an intrinsic propensity to form the necessary kink in the membrane-binding interface.

αS membrane-modulated aggregation due to lipid phase. To further investigate the effect of different lipid properties we recorded NMR spectra of αS in the presence of NDs containing different lipids and lipid mixtures. The data recorded with 100% 1-palmitoyl-2-oleoyl-sn-glycero-3-phosphocholine (POPC, one unsaturation, neutral charge) NDs do not show interaction (Fig. 3a, gray), comparable to 100% DMPC (no unsaturation, neutral charge) NDs (Fig. 1a–c, black). We also used all combinations of binary lipid mixtures of DMPC, 1,2-dimyristoyl-sn-glycero-3-phospho-(1′-rac-glycerol) (DMPG), POPC, and POPG, with an overall net charge content of 50%. Our data show that the heterogeneous mixtures DMPG/POPC and POPG/DMPC, and the homogeneous POPG/POPC mix behave very similarly (Fig. 3a), suggesting that the position of charge with respect to fatty acid as well as the 'surface roughness,' as potentially introduced by heterogeneous chain lengths, has little effect on αS–membrane interaction.

Interestingly, a mixture of fully saturated lipids (dimyristoyl lipids) with 50% charge content does not considerably interact with αS (Fig. 3b, beige). At the temperature of the NMR experiments (10 °C), the bilayer formed by saturated dimyristoyl lipids, in contrast to the partially unsaturated PO-lipids, is in

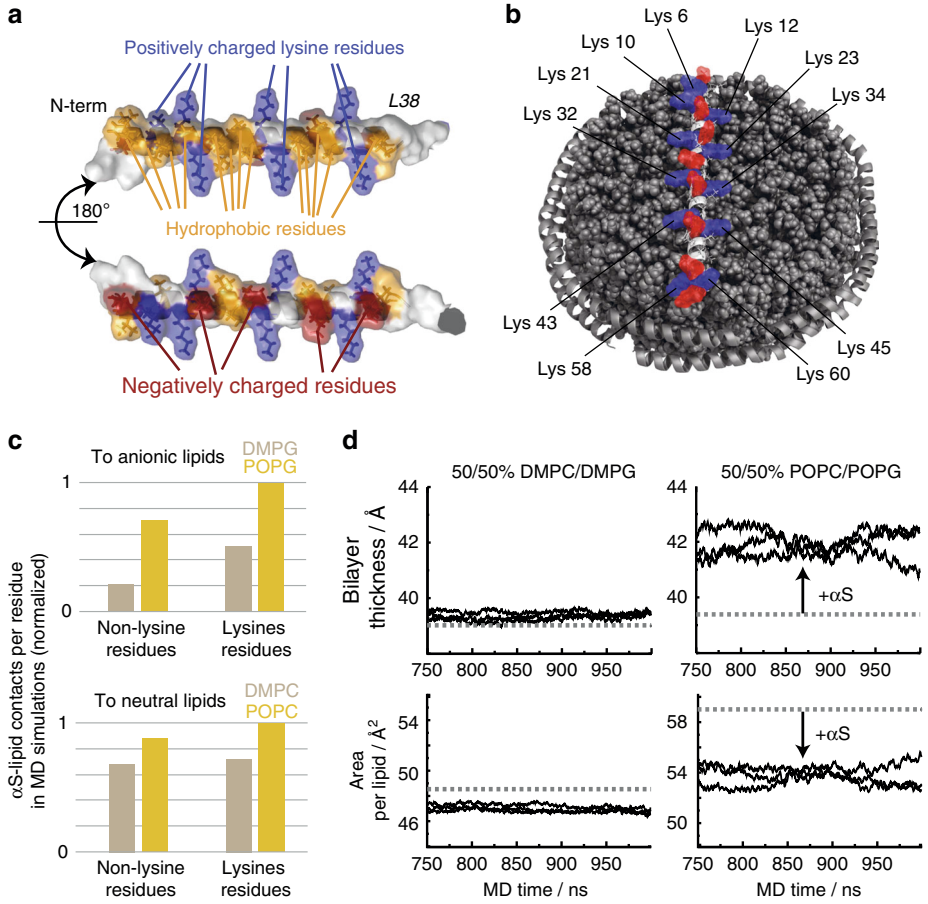

Fig. 4 αS–lipid interaction potentially modulates membrane plasticity. **a** Molecular features of αS's key lipid binding mode (residues 1–38), including periodically and symmetrically appearing lysine residues (blue) that form a positively charged "grid" (see text for more details). **b** Model of $\alpha S_{1\text{-}61}$-nanodisc interaction (drawn to scale), lysine (blue) and negatively charged residues (red) are highlighted. **c** αS-to-lipid contacts (< 4 Å) per residue as occurring during the time course of MD simulations. Normalized values for interactions with anionic lipids (upper diagram) or neutral lipids (lower diagram) differentiating between lysines and all other residues as well as between gel/fluid-phase membranes (beige/yellow bars), respectively. **d** Bilayer thickness (upper panels) and area per lipid (lower panels) during the end of MD simulations in the presence (solid lines, three independent simulations) and in the absence of αS (dashed line). While simulations in the gel phase show no considerable effect (**d**, left panels), a clear trend toward a more ordered state for the fluid phase membrane, induced by the presence of αS, is visible by an increase bilayer thickness and reduced area per lipid (**d**, right panels)

the gel phase (T_m around 28 °C, Supplementary Fig. 1d). When increasing the charge content to 100%, but remaining in the gel phase (100% DMPG, Fig. 3b, brown), αS shows a clear interaction with the membrane resembling a binding mode that is found for 50% charge content in the fluid phase. This data is well in line with previous CD data on SUVs that identified an important role of the lipid phase for αS–lipid interaction[30]. Although increasing the temperature for the NMR measurements above T_m leads to a previously observed loss of NMR signals due to amide-water exchange processes for most relevant residues, lowering the pH from 7.4 to 5.3 can counter this effect (Supplementary Fig. 3c-f). The respective NMR data show that αS forms a much larger binding interface with DMPG lipids in the fluid phase (Fig. 3b, red-brown bars, only peaks with easily transferable resonance assignments are plotted), in line with previous findings using vesicles[30,44], providing residue-specific insights into the modulation of αS membrane-binding modes by lipid phase properties.

Taken together, these data on αS–lipid association can be summarized as follows: (i) unsaturations in the hydrocarbon chains, leading to increased membrane fluidity, are not sufficient to induce binding; (ii) the presence of heterogeneity in fatty acid chains and the combination of charge and unsaturation on the same lipid molecule are not critical; and (iii) in addition to charge, a lipid phase state that introduces an increased membrane fluidity is important for binding.

We also performed ThT aggregation assays with NDs containing selected lipid mixtures as investigated by NMR. All mixtures that contain 50% negatively charged lipids, independently of acyl chain heterogeneity or charge position, show consistently unaffected aggregation behavior (Fig. 3c). However, αS aggregation is drastically impeded in the presence of 100% DMPG NDs (Fig. 3c, red-brown). As aggregation assays were measured at 37 °C, our NMR data (Fig. 3b, red-brown) show that αS is in a lipid-binding mode, which involves the NAC region and therefore is expected to inhibit aggregation.

αS and membrane plasticity: a two-way street. It is apparent that the initial N-terminal αS residues comprise a central lipid-binding motif with key features highly suitable for interactions with a charged lipid surface[45,52], and that these residues form a helical secondary structure after binding[16,23,29]. Based on the exposed and symmetric distribution of lysine residues, the occurrence of hydrophobic residues on one side of the helix and the distribution of negative charges on the opposite side (Fig. 4a), it is tempting to speculate that αS adopts a lipid-interacting conformation as shown in Fig. 4b. In this picture, it would be likely that the lipids

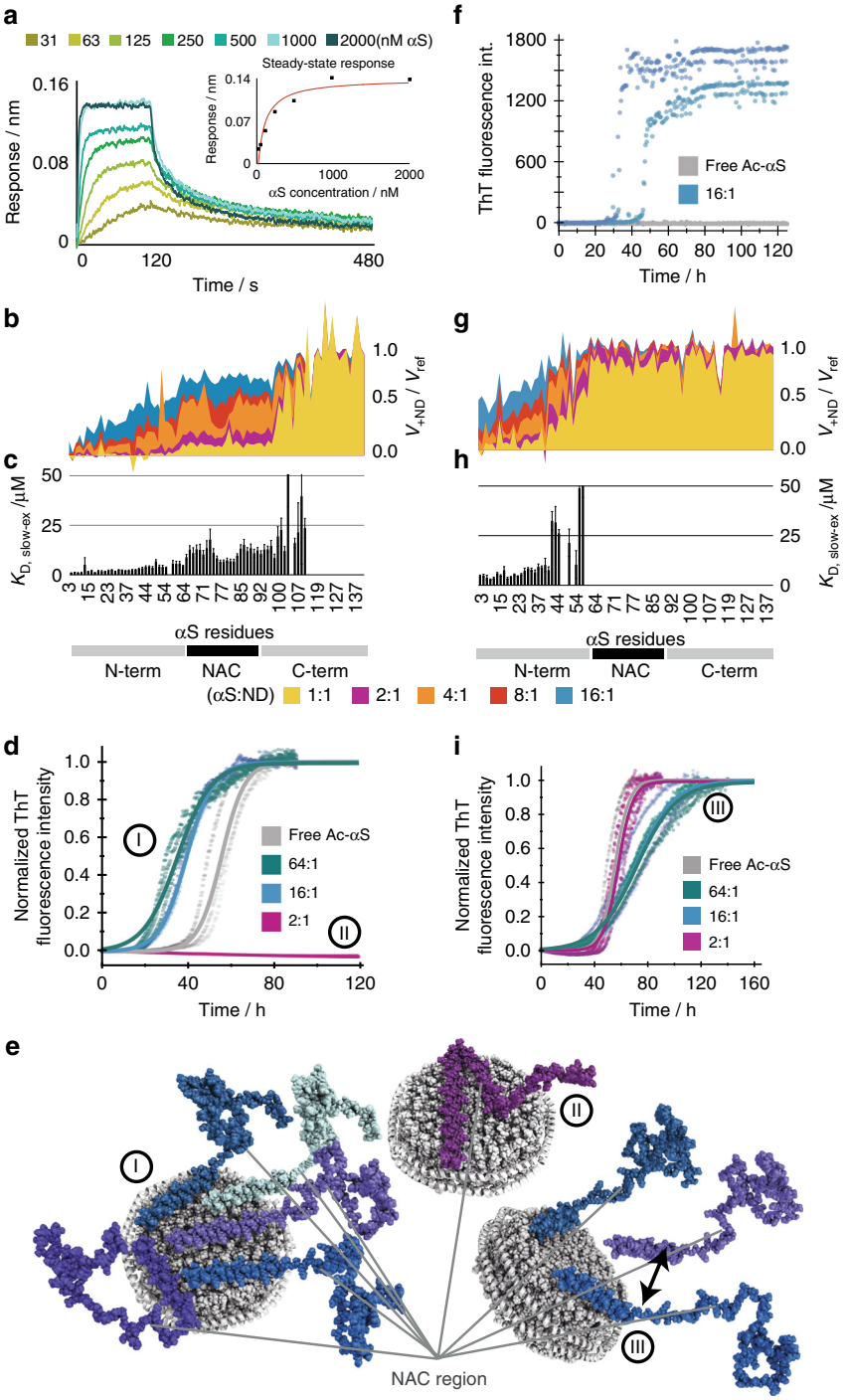

Fig. 5 The interplay between interaction kinetics, differential residue specific affinities, membrane charge density and accessible surface area modulates αS aggregation. **a** BLI sensorgrams obtained with immobilized 100% POPG NDs and addition of different concentrations of αS. Corresponding steady-state response plot are shown as insert. A fitted global affinity (K_D) of 67 ± 17 nM and a fitted off-rate of 0.015 ± 0.006 s^{-1} could be extracted. **b** NMR attenuation profiles of a titration of 50 μM αS with varying concentrations of 100% POPG NDs (αS-to-NDs molar ratios ranging from 16:1 to 1:1, see color code). **c** Corresponding residue-specific affinities extracted from NMR titration data. The values report on the slow-exchange (lower) limit for the affinities (see text for details). **d** Normalized ThT fluorescence aggregation curves for selected αS-to-ND ratios (conditions identical as in **b**–**g**). **e** NMR-derived binding modes and their link to the indicated aggregation behaviour (see Supplementary Note 3 for more details on how binding models were generated). Although high amounts of NDs with high charge density inhibit aggregation (binding mode II), limited amounts of highly charged membrane surfaces enhances aggregation (binding mode I). For NDs with a moderate lipid charged density, only one αS-binding mode was observed that has little effect on aggregation (binding mode III). **f** Nucleation ThT assays in quiescent conditions at pH 5.3. Although under these conditions no aggregation is observed in the absence of NDs (duplicates in gray), the presence of 16:1 molar ratio of 100% POPG NDs (duplicates in light and dark blue) induces primary nucleation. **g**–**i** Same as data shown in **b**–**d** but using NDs with 50% POPG content

and the lysine side chains (partly) rearrange, from their "unbound" conformation, to ideally accommodate electrostatic interactions. In line with our NMR results, this rearrangement may be favored by a more fluid lipid phase.

To test this hypothesis, we performed MD simulations of αS–membrane interactions. Our simulations focus on the first 61 residues of αS and their interactions with membranes formed by a mixture of either 50% POPG–50% POPC lipids in the fluid phase or a 50% DMPG–50% DMPC mix in the gel phase. The MD data confirm that lysine residues have a key role in the membrane interaction, as, e.g., visible by forming considerably more contacts to anionic lipids as compared with other residues (Fig. 4c, upper diagram). In addition, a generally stronger interaction of αS with the anionic lipids in the fluid membranes (POPG) is detected, as compared with the gel-phase membranes (DMPG) (Fig. 4c, yellow vs. beige). Noteworthy, these effects are much less pronounced for contacts to the neutral lipids (Fig. 4c, lower diagram). These findings correlate well with the effects of lipid charge and membrane plasticity seen in the NMR and aggregation assays.

Interestingly, the MD data also report on the effect of αS interaction from the lipid point of view. According to this data, the well-ordered DMPC/PG lipids (gel phase) experience very small effects due to the presence of αS. These MD results are in line with only small effects seen in differential scanning calorimetry profiles that we recorded on gel-phase NDs in the presence and absence of αS (see Supplementary Fig. 1e). On the other hand, for MD simulations of less ordered POPC/PG lipids (fluid phase), the presence of αS induces a considerably more ordered lipid state as evident by an increased bilayer thickness, reduced surface area per lipid, and increased order parameters for the hydrocarbon chains (Fig. 4d and Supplementary Fig. 4). In general, the MD data suggest that αS–membrane interaction is (initially) facilitated by increased membrane plasticity, e.g., via more contacts found in the fluid phase. These interactions may consequently confine lipids and lead to reduced membrane plasticity. The latter is in line with recent experimental data showing that αS binding can increase lipid packing[53,54], an effect that has also been suggested to have a role in αS function as chaperone for SNARE-mediated vesicle fusion[55].

The role of affinities and kinetics. In addition to modulation of binding modes due to lipid charge and membrane plasticity we were also interested in αS membrane-binding affinities and kinetics. We therefore measured interaction kinetics and thermodynamics using biolayer interferometry (BLI) with immobilized NDs of different charge contents. In line with the NMR data, no αS binding was detected when NDs containing 100% DMPC were immobilized. When NDs with 100% anionic lipid content were immobilized, a clear response upon addition of different αS concentrations was observed (Fig. 5a), enabling a quantitative description of the membrane association with an overall dissociation constants K_D of 67 ± 17 nM (one αS to one ND) and a slow off-rate of 0.015 ± 0.006 s^{-1}.

In order to obtain residue-specific insights into the membrane affinity of αS, we additionally conducted NMR titration experiments using 100% negatively charged NDs (Fig. 5b). In general, affinities (K_D) can be extracted from NMR titrations attenuation profiles by fitting the concentration dependency of the attenuation with a single exponential decay for each resolved peak (corresponding to one assigned residue in a two-state binding model, i.e., unbound and membrane attached). This method is valid under the assumption of a pure slow exchange regime. Although the BLI data clearly point to the presence of slow exchange processes, contributions from intermediate exchange are still to be expected for residues showing weaker membrane interactions, i.e., residues located in the central region of αS. For these residues, the applied method does not provide accurate quantitative values; nevertheless, a qualitative trend can still be extracted. It is noteworthy that the underestimation of exchange contributions will generate lower K_D values and hence the obtained values can be seen as a lower limit. The resulting slow-exchange-biased affinities ($K_{D,slow\text{-}ex}$) are plotted in Fig. 5c and reveal differential membrane affinities for different regions of the αS primary sequence. As discussed above due to the slow-exchange bias, the differential affinities of αS are probably even larger. It is noteworthy that the regions with differential affinities for highly charged membranes largely overlap with the different binding modes induced by different charge densities identified before (Fig. 1b).

Due to the geometry of the used NDs, up to five αS molecules can simultaneously bind with a 38-residue long α-helix (first binding mode) to one side of one ND. If 8 molecules are accommodated together on the surface, (on average) a 23-residue long helix per monomer could be formed. The observed differential affinities are therefore a direct consequence of the competition of different monomers for accessible membrane surface area. As a result, membrane association of the weaker interacting NAC region is strongly dependent on the accessibility of negatively charged membrane surface. Importantly, it appears that one ND with 100% negatively charged lipids can simultaneously interact with about 16 αS molecules (8 per ND side) in the course of the NMR time scale, as seen from the complete disappearance of the signals of the very N-terminal residues (Fig. 5b, light blue). This means that under this condition the membrane surface brings several αS molecules, with nearly fully exposed NAC regions, in close spatial proximity.

To characterize the effect of the accessible membrane surface area on αS aggregation behavior, we measured ThT aggregation kinetics on samples with different αS-to-ND ratios by decreasing the ND concentration at constant αS concentrations (Fig. 5d). Interestingly, a higher ratio of αS-to-ND leads to a prominent decrease in aggregation lag times when using 100% POPG NDs (Fig. 5d, blue and cyan). These data show, in line with previously reported behavior on SUVs[28,29], that under specific conditions lipid bilayers can accelerate the fibrillation process. Our NMR data allow to link these conditions, i.e., limited membrane surface area with a high charge density, to an αS–lipid-binding mode that brings several αS molecules with exposed NAC regions in close proximity (binding mode I in Fig. 5e).

In order to disentangle the effect of NDs on the nucleation or the elongation step in the αS aggregation pathway, we used ThT assays predominantly reporting on the one or the other (see methods for more details of assay design). Nucleation-sensitive assays in the presence of 100% POPG NDs and an αS-to-ND ratio of 16:1 indeed show that the underlying membrane association (binding mode I in Fig. 5e) enhances primary nucleation (Fig. 5f, blue). Interestingly, as our data also allow an estimation of the total number of αS monomers that are brought in close proximity due to their interaction with the same ND (i.e., up to 8 monomers per bilayer side, Fig. 5b blue), this result may also provide a first approximation of the number of αS monomers needed for the formation of a nucleus. As discussed above, our data suggest that this "minimal critical nucleation number" has an upper limit of around 8 αS molecules. It is noteworthy that this number is only an initial estimate and may be influenced by dynamic processes as well as local fluctuations, which may lower or increase the value by a few monomers.

Fibril elongation-sensitive aggregation assays carried out in the presence of 100% POPG NDs (Supplementary Fig. 5c, d) show no effect on elongation rates for αS-to-ND ratios of 16:1 (binding

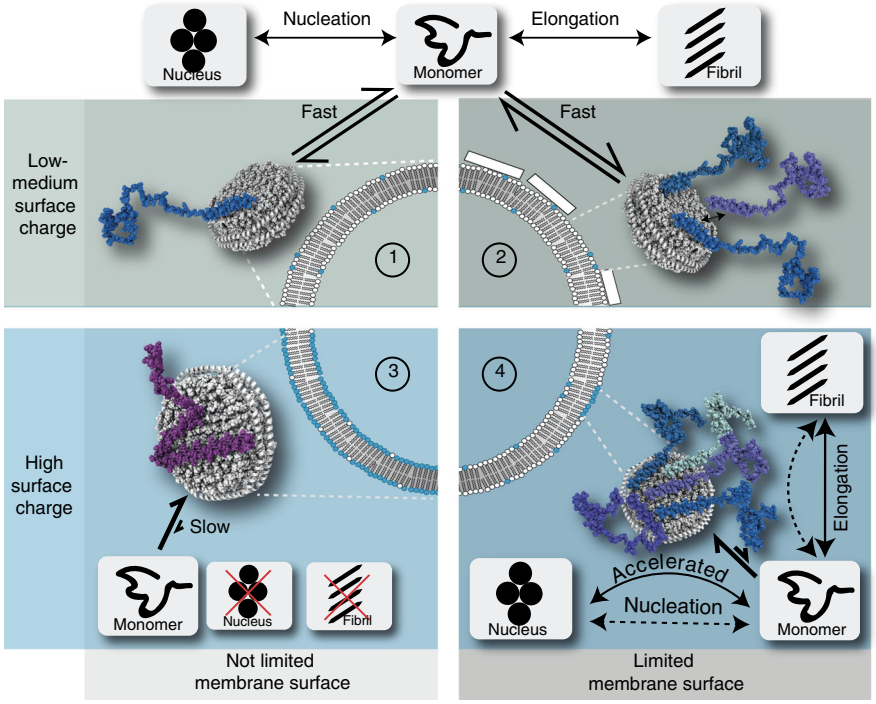

Fig. 6 Model of the influence of different NDs on the αS aggregation pathways and speculations regarding their potential implication in the context of cell/vesicle membranes. Four scenarios are depicted summarizing our in vitro data in respect to membrane surface charge and accessibility. (Note that schemes with nanodiscs and aggregation pathways are based on our findings, while possible implications in respect to physiological membranes are purely speculative.) In cases where membranes/NDs with only low charge densities are present (scenario 1 and 2) αS interacts with its N-terminal residues and forms an exchanging equilibrium between soluble and membrane associated αS monomers (binding mode III in Fig. 5e). This equilibrium does not seem to strongly interfere with the slow process of αS nucleation, it may however (slightly) decrease the pool of free monomers available for fibril formation. Although physiological membranes, in general, have a lower average charge density (represented by the upper panels), specific, abnormal, and/or stochastic processes may also lead to highly charged lipid clusters (lower panels). In the unlikely case of not limiting surface access (scenario 3) αS will interact in a binding mode that will largely inhibit both αS nucleation and fibril elongation (binding mode II in Fig. 5i). In cases with only local charge clusters, several αS monomers may compete for the limited highly charged membrane surface area (scenario 4). This binding mode (Fig. 5e mode I) can bring exposed NAC regions of several αS monomers in close proximity and accelerate the amyloid fibril nucleation process

mode I in Fig. 5e). However, a clear reduction in elongation rates with decreasing αS-to-ND ratio is visible, which is largely in line with sequestering monomers, in particular accessible NAC region, out of solution (Supplementary Fig. 5c, d). No fibril elongation is observed for αS with a fully membrane-bound NAC region (binding mode II in Fig. 5e) consistent with the overall aggregation-inhibiting properties of this condition. Noteworthy, unlike in the case of SUVs[29], atomic force microscopy (AFM) images of αS fibrils formed in the absence or presence of NDs do not show different morphology (Supplementary Fig. 6). This, however, does not exclude that (a limited amount of) lipids are also incorporated into the fibrils (see Supplementary Fig. 6 and stability considerations for more detailed discussion).

We additionally carried out the same BLI measurements, NMR titrations, and ThT assays for ND containing only 50% POPG lipids.

For these NDs, no clear signature of binding could be obtained in the BLI measurements, suggesting a weak affinity and/or too fast off rates to allow detection via BLI. This is in line with size exclusion chromatography (SEC) profiles that also point to a more transient interaction (Supplementary Fig. 1b, c).

NMR titrations, however, show clear concentration-dependent attenuation profiles that allow the calculation of (slow-exchange-biased) residue-specific affinities (Fig. 5g, h). Noteworthy, the NMR attenuation profiles and affinities for the αS residues in the first binding region (residues 1–38) are comparable to the values obtained for 100% charged NDs (Fig. 5b, c). In contrast, for the following binding regions much lower affinities are found (at the edge of detection for residues 39–60 and no interaction for residues > 60), including the absence of interactions of the NAC region. It is noteworthy that for the NDs with 50% anionic lipids the protein-to-ND ratio does not affect the overall binding mode (binding mode III in Fig. 5e). In line with an exposed NAC region, the ThT data for these NDs at low αS-to-ND ratios are consistently showing no effect on aggregation half-times (Fig. 5i). The data at higher ratios are less reproducible and show a slight tendency to prolonged elongation rates. Unlike for 100% POPG NDs and in line with the previously discussed moderate effects of 50% POPG NDs on the overall aggregation process, we did not observe accelerated αS nucleation in the presence of NDs with 50% POPG nor a clear perturbation of fibril elongation in seeded experiments (see Supplementary Fig. 7 for data and a more detailed discussion).

Discussion

Overall, our data demonstrate that the ND system allows to study the interaction of αS with stable, planar membranes in a quantitative, and site-resolved way. Many aspects of the membrane association are similar to previously reported interactions with micelles or SUVs, suggesting that features that distinguish the different membrane mimetics, such as curvature, physical bilayer borders, and potential vesicle disruption do not substantially alter the membrane binding properties of αS. The convenient handling, reliable, and unique quantification properties, as well as the wide compatibility of the NDs systems

for a broad range of biophysical techniques also enabled us to obtain a direct correlation between the structural and kinetic properties of the different membrane-binding modes and their consequences for αS amyloid fibril formation. In summary, our data show that (i) the N-terminal αS region interacts rather similarly with NDs composed of 100% or 50% anionic lipids; (ii) for 100% anionic lipids, the αS can adopt a substantially expanded binding mode as compared with 50% anionic lipid content, leading to considerably higher global affinities; (iii) the exchange rate between free αS in solution and membrane-bound αS is slow in the 100% charged case and likely to be faster in the 50% case; (iv) region-specific membrane affinities (especially the NAC region) are correlated with aggregation properties; (v) with sufficient excess of lipids and sufficient charge density, NDs can inhibit primary nucleation and fibril elongation by sequestering monomers out of solution; (vi) competition of αS monomers for highly charged lipid surface generates a membrane-bound αS conformation that can induce primary nucleation; and (vii) the number of αS monomers that are brought together by one ND and which can promote amyloid fibril nucleation is in the order of about 8 αS molecules.

Although our in vitro data directly support the above drawn conclusions, we can only speculate about which (if any) role these factors may have in vivo. Figure 6 summarizes the experimentally determined molecular and kinetic determinants of membrane-modulated αS aggregation and speculates about their potential physiological roles. In general, it should be noted that, in our study, the strongest effects were observed at lipid charge densities well above the average lipid compositions of native membranes. However, the normally found high lipid diffusion rates in physiological membranes may generate clusters of higher negative charges that may form spontaneously or be induced by an initially transient αS interaction. For the latter, the N-terminal acetylation may have an important role, as it increases membrane interaction at native lipid charge densities. Our data suggest that clusters of around 60–80 negatively charged lipids suffice to form a strong interaction (this may however not be the lower limit and specific physiological lipids not tested here may have even stronger effects). Sporadically formed charged lipid clusters could also induce a competition of several αS monomers for the accessible surface area. Our data show that due to the different residue-specific membrane affinities, this will generate a binding mode that, once the rather low αS critical oligomerization number is reached, can act as an aggregation seed. Such a scenario could promote the initial step of primary nucleation in the pathogenesis of Parkinson's disease and is in line with recent in vivo findings, suggesting that shielding αS from membrane interactions can inhibit initial steps of amyloid fibril formation including the formation of cell-toxic species[56].

Methods

αS expression and purification. Codon-optimized αS in the pT7-7 vector was expressed in *Escherichia coli* BL21 DE3. For acetylated αS, the N-terminal acetylation enzyme NatB from *Schizosaccharomyces pombe*, which will selectively acetylate αS at the free amino group of the N-terminus, was coexpressed in a second vector, pNatB[57]. Expression was conducted in 50 mM phosphate-buffered 2YT-medium (pH 7.2) with 0.4% glycerol and 2 mM $MgCl_2$, protein production was induced at OD 1-1.2 with 1 mM Isopropyl β-D-1-thiogalactopyranoside (IPTG) and run for 4 h at 37 °C. For ^{15}N-labeled protein, αS or acetylated αS was expressed in M9 medium with 0.2% $^{15}NH_4Cl$.

Sparsely labeled αS for DNP experiments was non-acetylated, expression was done in a similar way, in M9 medium using 0.4% [2-^{13}C]-glucose and 0.2% $^{15}NH_4Cl$. Isotope labeling of Phe, Gln, Glu, Pro, Asn, Asp, Met, Thr, Lys, and Ile was suppressed by supplementing sufficient quantities (150 μg ml^{-1} of each) of these unlabeled amino acids in the expression media as reported previously[51].

Purification of αS or acetylated αS was carried out as previously described[58], some changes to the original protocol have been made. Except for sparse labeled αS for which previous lysis in 20 mM Tris-HCl pH 8.0, 1 mM EDTA was done, cell lysis and release of αS or acetylated αS was performed by directly boiling the frozen cell pellet at 95 °C in a threefold volume of 20 mM sodium phosphate buffer, pH 7.4, for 30 min. Thermostable αS or acetylated αS remained in the supernatant after 30 min of centrifugation at 15,000 × *g* and 4 °C and was subsequently subjected to an ammonium sulfate precipitation by slowly adding saturated ammonium sulfate solution to 50% saturation at 4 °C. Precipitated protein was pelleted at 15,000 × *g* and 4 °C, dissolved in 50 ml of 50 mM Tris-HCl pH 8, sterile-filtered, and loaded onto an ion exchange chromatography column (HiTrap Q FF, GE Healthcare), where αS or acetylated αS eluted at around 300 mM NaCl in 50 mM Tris-HCl pH 8. Elution fractions containing αS or acetylated αS were subjected to another ammonium sulfate precipitation and finally purified by a SEC run (Superdex 75 10/300, GE Healthcare) in 20 mM sodium phosphate pH 7.4, 50 mM NaCl.

N-terminal acetylation of acetyl-αS was checked by high-performance liquid chromatography, mass spectrometry, and NMR, proved to be about 95% when co-expressed with NatB.

Membrane scaffold protein expression and purification. As reported before[59], *E. coli* BL21 (DE3) were transformed with MSP1D1 or MSP1D1ΔH5 plasmid DNA in vector pET28a. Cells were grown in lysogeny broth (LB) medium, induced by 1 mM IPTG at an optical density of 0.7, and incubated 5–6 h at 37 °C, then pelleted down. Cells were resuspended in 50 mM Tris-HCl pH 8, 500 mM NaCl (buffer B) supplemented with 6 M GdnHCl and EDTA-free Complete protease inhibitors (Macherey–Nagel) lysed by sonication (Bandelin Sonopuls MS72 probe), centrifuged at 17,000 × *g* for 1 h (Beckman J2-21 rotor JA-20.1) and incubated 1 h with previously equilibrated 2.5 ml Ni-NTA agarose resin/3 l culture (Macherey–Nagel). Column was washed with 4 column volumes (CV) buffer B, 4 CV buffer B supplemented with 1% Triton X-100, 4 CV buffer B + 60 mM Na-cholate, 4 CV buffer B, and 4 CV buffer B + 20 mM imidazole. Four fractions of 1 CV were eluted with 250 mM imidazole. The whole process was kept at 4 °C in a cold room. The elution fractions were pooled and dialysed against 100-fold 200 mM Tris-HCl pH 7.5, 100 mM NaCl. N-terminal His-tag was cleaved using tobacco etch virus (TEV) protease incubated overnight at 4 °C. ΔHis-MSP was separated by immobilized metal affinity chromatography (IMAC) and concentrated to the desired molarity using a Vivaspin centrifugal device of 10 kDa molecular weight cutoff (MWCO).

ND assembly. NDs were assembled according to established protocols[31]. In short, lipids' chloroform stocks were dried under nitrogen flow to obtain a lipid film and stored under vacuum overnight. ΔHis-MSP1D1 or MSP1D1ΔH5 and the appropriate amount of lipids (Avanti Polar Lipids) solubilized in 60 mM Na-cholate were mixed together in 20 mM Tris-HCl pH 7.5, 100 mM NaCl, 5 mM EDTA. The scaffold-to-lipids molar ratio was calculated from geometrical considerations. 20% w/v of previously washed Biobeads SM-2 (Biorad) were added and the mixture incubated at room temperature overnight. The Biobeads were removed by centrifugation and once again 20% w/v were added for an additional 4–5 h. Finally, they were purified by SEC on a HiLoad 16/600 Superdex 200 pg column (GE Healthcare) equilibrated with 20 mM sodium phosphate pH 7.4, 50 mM NaCl using a Äkta pure device at a flow rate of 1 ml min^{-1}. The quality of NDs preparation was check by the SEC chromatogram and by DLS (PSS Nicomp). NDs were concentrated to the desired molarity using a Vivaspin centrifugal device of 10 kDa MWCO. It is noteworthy that concentration of NDs can be rather accurately determined using the 280 nm absorbance of the membrane scaffold proteins and lipid concentration can be estimated using the geometrically ideal lipid amount per ND, i.e., 156 DMPC molecules or 150 POPG molecules.

Biolayer interferometry. NDs were immobilized on the sensor surface of amine reactive biosensors (AG2R) (fortéBIO, PALL Life Science) after 1-ethyl-3-(3-dimethylaminopropyl)carbodiimide/N-hydroxysulfoxuccinimide (EDC/NHS) activation to a final level between 1.2 and 1.8 nm depending on the NDs type using an Octet RED96 instrument (fortéBIO, PALL Life Science). All biosensors were quenched with 1 M ethanolamine for 3 min. All experiments were carried out in multi cycle kinetics at 25 °C. Association of αS in running buffer (20 mM sodium phosphate pH 7.4, 50 mM NaCl) on NDs and reference biosensors was recorded for 120 s, followed by a dissociation phase of 360 s. Sensorgrams were double referenced using the reference biosensors and a buffer cycle. Steady-state analysis was realized by fitting the αS concentration dependency of the highest response with a simple 1:1 binding model. After normalization, all on and off curves were fitted against simple exponential build-up or decays and led to similar on- and off-rates.

Solution NMR spectroscopy. Solution NMR experiments were performed on a Bruker Avance III HD$^+$ spectrometer operating at 600 MHz ^{1}H Larmor frequency, equipped with a triple resonance TCI (^{1}H, ^{13}C, ^{15}N) cryoprobe and shielded z-gradients. If not stated otherwise, all experiments were recorded at 10 °C with an αS concentration of 50 μM in 20 mM sodium phosphate pH 7.4, 50 mM NaCl, 10% (v/v) ^2H_2O, and ND concentration was set to 25 μM (one αS per membrane leaflet). All [^{1}H-^{15}N]-TROSY-HSQC NMR spectra were acquired with 32 scans and 256 indirect increments, processed with TOPSPIN 3.2 (Bruker) and analyzed with CCPN[60]. A full list of measured samples can be found in Supplementary Table 1. For attenuation profiles, peaks were automatically integrated and the ratio of volumes in the presence and absence of NDs plotted against the primary

sequence. The raw data without normalization, multi-residue averaging, or manual compensation of peak position is shown. Negative values are results of noise contributions and/or slight peak shifts. Outliers as results of peak overlap and/or ambiguities were removed.

ThT fluorescence aggregation assays. Three types of aggregation assays were used in this study. Unless otherwise stated, a setup under conditions where αS amyloid fibrils form spontaneously, mainly by interface-driven nucleation and subsequent amplification through fragmentation, was chosen. Experiments under these conditions mainly report on the potential interference of NDs on the lipid-independent aggregation pathways. Here, 50 μM of αS or acetylated αS was mixed with either 25 μM (2:1), 3.125 μM (16:1), or 0.781 μM (64:1) NDs with different lipid compositions. Assays were conducted in 20 mM sodium phosphate buffer pH 7.4 or 20 mM acetate buffer pH 5.3 with 50 mM NaCl, 0.02% NaN_3, and 10 μM ThT. Unless otherwise stated, triplicates of 120 μl were pipetted into 96-well half-area well plates with non-binding surface (Corning No. 3881, black, clear bottom) containing a glass ball (2.85–3.45 mm diameter) for mixing and incubated at 37 °C for up to 7 days. Orbital shaking at 217 r.p.m. was used for 15 s every 20 min. ThT fluorescence was excited at 445 nm and measured at 485 nm every 20 min with 15 s of shaking before the measurement in a plate reader (Tecan Spark 10 M or Tecan infinite M1000PRO).

Nucleation-sensitive assays: Under that minimize the intrinsic nucleation rate (quiescent conditions and protein repellent plate surfaces), lipid bilayers in the form of SUVs can accelerate the nucleation of αS amyloid fibrils[29]. In order to determine whether NDs can have a similarly accelerating effect, we performed ThT aggregation experiments under similar conditions, i.e., where no αS aggregation should be detected in the absence of lipids. These experiments were performed at mildly acidic pH (5.3), as it was recently shown that under these conditions, αS amyloid fibrils can amplify autocatalytically through surface-catalyzed secondary nucleation[49,61]. This should in principle enable even very low primary nucleation rates to be detected through autocatalytic amplification.

Elongation-sensitive assays: Seeded experiments using preformed αS fibrils were used to measure the effect of NDs on fibril elongation. Fibril seeds of αS or acetylated αS were prepared as follows: 300 μl of 100 μM αS or acetylated αS was fibrillated at 37 °C and 800 r.p.m. for 3 days in a 2 ml tube containing a glass ball in a Thermomixer (Eppendorf). The fibril solution was diluted to 50 μM and sonicated with a tip sonicator (Bandelin Sonopuls HD3200, BANDELIN electronic) at 10% power (20 W) for 60 s, with 1 s pulses on and 4 s off in between. Seed solution was diluted 20-fold for the aggregation assays (2.5 μM, 5%).

Assay analysis: Kinetic curves were corrected by subtracting the curve of buffer (containing NDs) in the presence of ThT and normalized to the highest fluorescence intensity (in line with comparable fibril mass seen in SDS-polyacrylamide gel electrophoresis after the aggregation assay). The corresponding triplicates are shown as transparent circles in order to visualize the reproducibility of each experiment. Data fits were obtained using a simple sigmoidal function and the Abscissa 2D plot tool (by Rüdiger Brühl). In the case of quiescent nucleation and seeded assays, no normalization was applied and data were recorded without the presence of glass balls and without plate shaking.

SDS–polyacrylamide gel electrophoresis. In order to compare the amounts of soluble and fibrillated αS or acetylated αS in the aggregation samples, 100 μl of each triplicate sample were taken out of the well plate, combined in 1.5 ml tubes, and spun down at 20,000 × *g* and 20 °C for 30 min. Supernatants (~ 290 μl) were removed and pellets were resuspended in 280 μl buffer, and SDS-sample buffer (4-fold) was added. Samples were boiled for 15 min at 98 °C and subsequently 10 μl were loaded onto a 15% SDS-gel together with standards of αS or acetylated αS and NDs.

DNP NMR spectroscopy. Magic-angle spinning solid-state DNP experiments were performed on a Bruker Avance III HD spectrometer operating at 600 MHz, equipped with a 395.18 GHz second-harmonic gyrotron and a 3.2 mm $^{1}H,^{13}C,^{15}N$ triple resonance low-temperature magic-angle-spinning probe. Data were collected at 100 K, 9 kHz magic angle spinning speed, and 9 W continuous-wave microwave power. The samples were prepared from sparsely labeled non-acetylated αS (250 μg) in the presence or in the absence of 2:1 molar ratio of 100% POPG NDs, and filled into 3.2 mm sapphire rotors. Final buffer conditions in the sample were 15 mM sodium phosphate pH 7.4, 25 mM sodium chloride, 30% $^{2}H_2O$, 60% glycerol-d_6, and 2.5 mM AMUPOL[62]. Two-dimensional [^{13}C-^{13}C]-proton-driven spin diffusion experiments with 1 s mixing time were performed. It is noteworthy that this DNP setup also allows a more detailed quantatitive analysis of different αS conformational ensembles and the effects of different polarization transfers as well[63]. ^{1}H decoupling using SPINAL64 with a decoupling field of 104 kHz was employed during evolution and detection periods. Both experiments were conducted using 300 t_1 increments with 16 and 48 scans each for αS in the absence and in the presence of NDs, respectively. A recycle delay of 5 s was used in both experiments. Both spectra were processed using Topspin 3.2 (Bruker) using identical parameters with squared and shifted sine bell function (qsine 2.5) for apodization.

MD simulations. As starting conformation for the MD simulations, the NMR structure of micelle-bound αS (PDB 1XQ8) was used, considering only the first 61 residues in order to concentrate on the membrane-binding region of αS.

The Amber99sb-ILDN force field[64] was used for αS, which was simulated in its non-acetylated form (i.e., with NH3 + at the N-terminus) and with a C-terminal N-methyl amide capping group to account for the fact that αS would continue beyond residue 61. All lysine side chains were modeled as positively charged, glutamate and aspartate as negatively charged, whereas glutamine and histidine residues were considered to be neutral corresponding to pH 7.4. The protein was placed either 0.5 nm or 1.5 nm above the membrane surface. A starting orientation with the negatively charged side chains pointing away from the membrane and the lysine side chains being oriented toward the membrane surface were chosen (Fig. 4b). For modeling the lipid bilayer, membrane patches consisting of POPC/POPG (1:1) or DMPC/DMPG (1:1) involving 512 lipids (256 lipids per leaflet) were built using CHARMM-GUI[65] and modeled with Slipids force field parameters[66,67]. Before αS was added, both lipid bilayers were solvated and simulated for 500 ns (POPC/POPG) or 1000 ns (DMPC/DMPG) to obtain relaxed membranes. Here, the same simulation procedure was employed as described below. αS was placed above the membrane, the protein–membrane complex solvated using the TIP3 water model, and Na^+ and Cl^- were added to neutralize the system and to mimic the Na + concentration used in the experiments. The ion parameters of Smith and Dang[68] were used. The system was then subjected to steepest descent energy minimization, followed by MD equilibration in the constant number (N), volume (V) and temperature (T) (NVT) ensemble for 1 ns at 10 °C using the V-rescale thermostat[69] with a time constant of 0.5 ps and separate temperature coupling for the protein, membrane, and water/ions. Afterwards, 1 ns of constant number (N), pressure (P) and temperature (T) (NPT) equilibration was performed using the Nose–Hoover thermostat[70,71] and Parrinello–Rahman barostat[72] with semi-isotropic pressure scaling, a reference pressure of 1 bar, a time constant of 10.0 ps, and an isothermal compressibility of 4.5×10^{-5} bar^{-1}. During both equilibration steps, restraints were applied to the positions of the P-atoms of the lipids and terminal C-atoms of their tails with a force constant of 1000 kJ mol^{-1} nm^{-2}. All bond lengths were constrained using the Lincs algorithm[73]. The Coulombic interactions were calculated using the Particle mesh Ewald method[74,75] with a cutoff value of 1.0 nm for the short-range interactions and a Fourier spacing of 0.12 nm. The cutoff value for the van der Waals interactions was set at 1.4 nm. Periodic boundary conditions were employed in all directions. For the MD production runs, the same settings as for the NPT equilibration were used, except that all position restraints were removed. All MD simulations were performed at 10 °C with a time step of 2 fs for integration using the GROMACS 4.6 MD package[76]. For the analysis, which was performed using Gromacs and Membrainy tools[77], only the last 250 ns of each production run was used.

A full list of simulations can be found in Supplementary Table 2.

Size exclusion chromatography. For analytical SEC, an Akta pure systems equipped with a Superdex 200 13/300 gl column (GE Healthcare) was used. After equilibration with two column volumes of running buffer (20 mM sodium phosphate pH 7.4, 50 mM NaCl), samples of approximately 5 μM NDs, 10 μM αS, or a mix thereof were injected at a flowrate of 0.5 ml min^{-1}. In order to assay stability of the NDs in the presence of αS, the same mix was incubated 24 h at room temperature and injected afterwards.

Differential scanning calorimetry. Samples of approximately 5 μM NDs of different types (and if stated 10 μM αS) in running buffer (20 mM sodium phosphate pH 7.4, 50 mM NaCl) were degassed for at least 20 min at 30 °C and measured in a Microcal VP-DSC instrument (Malvern Instruments). After equilibration and a pre-scan delay of 20 min, the thermograms were acquired up-scan from 5 °C to 45 °C at a scanning rate of 0.5 °C min^{-1} and corrected by subtracting the thermogram of buffer and adjusting the baseline to zero at 45 °C (*y*-axis molarity refers to estimated amounts of lipids).

Atomic force microscopy. AFM images were taken in air, using a Nanowizard III atomic force microscope (JPK, Berlin). Samples were taken at the end of aggregation experiments and diluted in pure water to approximately 1 μM protein concentration. Ten microliters of sample were added onto freshly cleaved mica and left to dry. Then, they were gently rinsed with water to remove excess salt. Imaging was performed using tapping mode with NSC 36 cantilevers (MikroMasch), with resonant frequencies between 70 and 150 kHz.

Data availability. The datasets generated during and/or analysed during the current study are available from the corresponding author on request. NMR chemical shift asignments are in line with data already deposited in the Biological Magnetic Resonance Data Bank, e.g., under accession codes 19350 (acetlyated) and 19337 (non-acetylated)[78].

Received: 24 November 2017 Accepted: 23 March 2018
Published online: 03 May 2018

References

1. Spillantini, M. G. et al. Alpha-synuclein in lewy bodies. *Nature* **388**, 839–840 (1997).
2. Luk, K. C. et al. Pathological alpha-synuclein transmission initiates parkinson-like neurodegeneration in nontransgenic mice. *Science (New York, N. Y.)* **338**, 949–953 (2012).
3. Jucker, M. & Walker, L. C. Self-propagation of pathogenic protein aggregates in neurodegenerative diseases. *Nature* **501**, 45–51 (2013).
4. Tuttle, M. D. et al. Solid-state NMR structure of a pathogenic fibril of full-length human alpha-synuclein. *Nat. Struct. Mol. Biol.* **23**, 409–415 (2016).
5. Gitler, A. D. et al. The Parkinson's disease protein alpha-synuclein disrupts cellular Rab homeostasis. *Proc. Natl Acad. Sci. USA* **105**, 145–150 (2008).
6. Bellani, S. et al. The regulation of synaptic function by alpha-synuclein. *Commun. Integr. Biol.* **3**, 106–109 (2010).
7. Diao, J. et al. Native alpha-synuclein induces clustering of synaptic-vesicle mimics via binding to phospholipids and synaptobrevin-2/VAMP2. *eLife* **2**, e00592 (2013).
8. Fusco, G. et al. Structural basis of synaptic vesicle assembly promoted by alpha-synuclein. *Nat. Commun.* **7**, 12563 (2016).
9. Zhu, M., Li, J. & Fink, A. L. The association of alpha-synuclein with membranes affects bilayer structure, stability, and fibril formation. *J. Biol. Chem.* **278**, 40186–40197 (2003).
10. Dikiy, I. & Eliezer, D. Folding and misfolding of alpha-synuclein on membranes. *Biochim. Et. Biophys. Acta* **1818**, 1013–1018 (2012).
11. Butterfield, S. M. & Lashuel, H. A. Amyloidogenic protein-membrane interactions: Mechanistic insight from model systems. *Angew. Chem. Int. Ed. Engl.* **49**, 5628–5654 (2010).
12. Auluck, P. K., Caraveo, G. & Lindquist, S. Alpha-synuclein: membrane interactions and toxicity in parkinson's disease. *Annu. Rev. Cell Dev. Biol.* **26**, 211–233 (2010).
13. Nemani, V. M. et al. Increased expression of alpha-synuclein reduces neurotransmitter release by inhibiting synaptic vesicle reclustering after endocytosis. *Neuron* **65**, 66–79 (2010).
14. Dikiy, I. & Eliezer, D. N-terminal acetylation stabilizes n-terminal helicity in lipid- and micelle-bound alpha-synuclein and increases its affinity for physiological membranes. *J. Biol. Chem.* **289**, 3652–3665 (2014).
15. Rhoades, E., Ramlall, T. F., Webb, W. W. & Eliezer, D. Quantification of α-synuclein binding to lipid vesicles using fluorescence correlation spectroscopy. *Biophys. J.* **90**, 4692–4700 (2006).
16. Jo, E., McLaurin, J., Yip, C. M., St George-Hyslop, P. & Fraser, P. E. Alpha-synuclein membrane interactions and lipid specificity. *J. Biol. Chem.* **275**, 34328–34334 (2000).
17. Bodner, C. R., Dobson, C. M. & Bax, A. Multiple tight phospholipid-binding modes of alpha-synuclein revealed by solution NMR spectroscopy. *J. Mol. Biol.* **390**, 775–790 (2009).
18. Theillet, F. X. et al. Structural disorder of monomeric alpha-synuclein persists in mammalian cells. *Nature* **530**, 45–50 (2016).
19. Bodner, C. R., Maltsev, A. S., Dobson, C. M. & Bax, A. Differential phospholipid binding of alpha-synuclein variants implicated in parkinson's disease revealed by solution NMR spectroscopy. *Biochemistry* **49**, 862–871 (2010).
20. Ulmer, T. S., Bax, A., Cole, N. B. & Nussbaum, R. L. Structure and dynamics of micelle-bound human alpha-synuclein. *J. Biol. Chem.* **280**, 9595–9603 (2005).
21. Jao, C. C., Hegde, B. G., Chen, J., Haworth, I. S. & Langen, R. Structure of membrane-bound alpha-synuclein from site-directed spin labeling and computational refinement. *Proc. Natl Acad. Sci. USA* **105**, 19666–19671 (2008).
22. Drescher, M. et al. Antiparallel arrangement of the helices of vesicle-bound alpha-synuclein. *J. Am. Chem. Soc.* **130**, 7796–7797 (2008).
23. Fusco, G. et al. Direct observation of the three regions in alpha-synuclein that determine its membrane-bound behaviour. *Nat. Commun.* **5**, 3827 (2014).
24. Eliezer, D., Kutluay, E., Bussell, R. Jr & Browne, G. Conformational properties of alpha-synuclein in its free and lipid-associated states. *J. Mol. Biol.* **307**, 1061–1073 (2001).
25. Georgieva, E. R., Ramlall, T. F., Borbat, P. P., Freed, J. H. & Eliezer, D. Membrane-bound alpha-synuclein forms an extended helix: long-distance pulsed esr measurements using vesicles, bicelles, and rodlike micelles. *J. Am. Chem. Soc.* **130**, 12856–12857 (2008).
26. Drescher, M. et al. Spin-label epr on alpha-synuclein reveals differences in the membrane binding affinity of the two antiparallel helices. *Chembiochem* **9**, 2411–2416 (2008).
27. Zhu, M. & Fink, A. L. Lipid binding inhibits alpha-synuclein fibril formation. *J. Biol. Chem.* **278**, 16873–16877 (2003).
28. Zhao, H., Tuominen, E. K. & Kinnunen, P. K. Formation of amyloid fibers triggered by phosphatidylserine-containing membranes. *Biochemistry* **43**, 10302–10307 (2004).
29. Galvagnion, C. et al. Lipid vesicles trigger alpha-synuclein aggregation by stimulating primary nucleation. *Nat. Chem. Biol.* **11**, 229–234 (2015).
30. Galvagnion, C. et al. Chemical properties of lipids strongly affect the kinetics of the membrane-induced aggregation of alpha-synuclein. *Proc. Natl Acad. Sci. USA* **113**, 7065–7070 (2016).
31. Bayburt, T. H., Grinkova, Y. V. & Sligar, S. G. Self-assembly of discoidal phospholipid bilayer nanoparticles with membrane scaffold proteins. *Nano Lett.* **2**, 853–856 (2002).
32. Zhang, Z. et al. Ca(2+) modulating alpha-synuclein membrane transient interactions revealed by solution NMR spectroscopy. *Biochim. Et. Biophys. Acta* **1838**, 853–858 (2014).
33. Thomaier, M. et al. High-affinity binding of monomeric but not oligomeric amyloid-beta to ganglioside GM1 containing nanodiscs. *Biochemistry* **55**, 6662–6672 (2016).
34. Viegas, A., Viennet, T. & Etzkorn, M. The power, pitfalls and potential of the nanodisc system for NMR-based studies. *Biol. Chem.* **397**, 1335–1354 (2016).
35. Denisov, I. G., Grinkova, Y. V., Lazarides, A. A. & Sligar, S. G. Directed self-assembly of monodisperse phospholipid bilayer nanodiscs with controlled size. *J. Am. Chem. Soc.* **126**, 3477–3487 (2004).
36. Her, C. et al. The charge properties of phospholipid nanodiscs. *Biophys. J.* **111**, 989–998 (2016).
37. Inagaki, S. et al. Modulation of the interaction between neurotensin receptor NTS1 and Gq protein by lipid. *J. Mol. Biol.* **417**, 95–111 (2012).
38. Ouberai, M. M. et al. Alpha-synuclein senses lipid packing defects and induces lateral expansion of lipids leading to membrane remodeling. *J. Biol. Chem.* **288**, 20883–20895 (2013).
39. Eichmann, C. et al. Preparation and characterization of stable alpha-synuclein lipoprotein particles. *J. Biol. Chem.* **291**, 8516–8527 (2016).
40. Comellas, G., Lemkau, L. R., Zhou, D. H., George, J. M. & Rienstra, C. M. Structural intermediates during α-synuclein fibrillogenesis on phospholipid vesicles. *J. Am. Chem. Soc.* **134**, 5090–5099 (2012).
41. Hagn, F., Etzkorn, M., Raschle, T. & Wagner, G. Optimized phospholipid bilayer nanodiscs facilitate high-resolution structure determination of membrane proteins. *J. Am. Chem. Soc.* **135**, 1919–1925 (2013).
42. Etzkorn, M. et al. Cell-free expressed bacteriorhodopsin in different soluble membrane mimetics: biophysical properties and NMR accessibility. *Structure* **21**, 394–401 (2013).
43. Iyer, A. et al. The impact of N-terminal acetylation of alpha-synuclein on phospholipid membrane binding and fibril structure. *J. Biol. Chem.* **291**, 21110–21122 (2016).
44. Pirc, K. & Ulrih, N. P. Alpha-synuclein interactions with phospholipid model membranes: Key roles for electrostatic interactions and lipid-bilayer structure. *Biochim. Biophys. Acta* **1848**, 2002–2012 (2015).
45. Lokappa, S. B. et al. Sequence and membrane determinants of the random coil-helix transition of alpha-synuclein. *J. Mol. Biol.* **426**, 2130–2144 (2014).
46. Rabe, M. et al. On-surface aggregation of α-synuclein at nanomolar concentrations results in two distinct growth mechanisms. *ACS Chem. Neurosci.* **4**, 408–417 (2013).
47. Vacha, R., Linse, S. & Lund, M. Surface effects on aggregation kinetics of amyloidogenic peptides. *J. Am. Chem. Soc.* **136**, 11776–11782 (2014).
48. Campioni, S. et al. The presence of an air-water interface affects formation and elongation of alpha-synuclein fibrils. *J. Am. Chem. Soc.* **136**, 2866–2875 (2014).
49. Gasper, R. et al. Secondary nucleation of monomers on fibril surface dominates α-synuclein aggregation and provides autocatalytic amyloid amplification. *Quart. Rev. Biophys.* **50**, e6 (2017).
50. Siemer, A. B., Huang, K. Y. & McDermott, A. E. Protein linewidth and solvent dynamics in frozen solution nmr. *PLoS ONE* **7**, e47242 (2012).
51. Hong, M. & Jakes, K. Selective and extensive 13C labeling of a membrane protein for solid-state NMR investigations. *J. Biomol. NMR* **14**, 71–74 (1999).
52. Davidson, W. S., Jonas, A., Clayton, D. F. & George, J. M. Stabilization of alpha-synuclein secondary structure upon binding to synthetic membranes. *J. Biol. Chem.* **273**, 9443–9449 (1998).
53. Iyer, A., Petersen, N. O., Claessens, M. M. & Subramaniam, V. Amyloids of alpha-synuclein affect the structure and dynamics of supported lipid bilayers. *Biophys. J.* **106**, 2585–2594 (2014).
54. Reynolds, N. P. et al. Mechanism of membrane interaction and disruption by alpha-synuclein. *J. Am. Chem. Soc.* **133**, 19366–19375 (2011).
55. Burre, J. et al. Alpha-synuclein promotes snare-complex assembly in vivo and in vitro. *Science* **329**, 1663–1667 (2010).
56. Perni, M. et al. A natural product inhibits the initiation of alpha-synuclein aggregation and suppresses its toxicity. *Proc. Natl Acad. Sci. USA* **114**, E1009–E1017 (2017).
57. Johnson, M., Coulton, A. T., Geeves, M. A. & Mulvihill, D. P. Targeted amino-terminal acetylation of recombinant proteins in *E. coli*. *PLoS ONE* **5**, e15801 (2010).
58. Hoyer, W. et al. Dependence of α-synuclein aggregate morphology on solution conditions. *J. Mol. Biol.* **322**, 383–393 (2002).

59. Bayburt, T. H., Carlson, J. W. & Sligar, S. G. Reconstitution and imaging of a membrane protein in a nanometer-size phospholipid bilayer. *J. Struct. Biol.* **123**, 37–44 (1998).
60. Vranken, W. F. et al. The CCPN data model for NMR spectroscopy: development of a software pipeline. *Proteins* **59**, 687–696 (2005).
61. Buell, A. K. et al. Solution conditions determine the relative importance of nucleation and growth processes in alpha-synuclein aggregation. *Proc. Natl Acad. Sci. USA* **111**, 7671–7676 (2014).
62. Sauvee, C. et al. Highly efficient, water-soluble polarizing agents for dynamic nuclear polarization at high frequency. *Angew. Chem. Int. Ed. Engl.* **52**, 10858–10861 (2013).
63. Uluca, B. et al. DNP-enhanced MAS NMR: A tool to snapshot conformational ensembles of alpha-synuclein in different states. *Biophys. J.* **114**, 1614–1623 (2018).
64. Lindorff-Larsen, K. et al. Improved side-chain torsion potentials for the amber ff99sb protein force field. *Proteins* **78**, 1950–1958 (2010).
65. Lee, J. et al. Charmm-GUI input generator for namd, gromacs, amber, openmm, and charmm/openmm simulations using the charmm36 additive force field. *J. Chem. Theory Comput.* **12**, 405–413 (2016).
66. Jambeck, J. P. & Lyubartsev, A. P. Derivation and systematic validation of a refined all-atom force field for phosphatidylcholine lipids. *J. Phys. Chem. B* **116**, 3164–3179 (2012).
67. Jambeck, J. P. & Lyubartsev, A. P. Another piece of the membrane puzzle: extending slipids further. *J. Chem. Theory Comput.* **9**, 774–784 (2013).
68. Smith, D. E. & Dang, L. X. Computer simulations of nacl association in polarizable water. *J. Chem. Phys.* **100**, 3757–3766 (1994).
69. Bussi, G., Donadio, D. & Parrinello, M. Canonical sampling through velocity rescaling. *J. Chem. Phys.* **126**, 014101 (2007).
70. Nosé, S. A molecular dynamics method for simulations in the canonical ensemble. *Mol. Phys.* **52**, 255–268 (1984).
71. Hoover, W. G. Canonical dynamics: equilibrium phase-space distributions. *Phys. Rev. A: General. Phys.* **31**, 1695–1697 (1985).
72. Parrinello, M. & Rahman, A. Polymorphic transitions in single crystals: a new molecular dynamics method. *J. Appl. Phys.* **52**, 7182–7190 (1981).
73. Hess, B., Bekker, H., Berendsen, H. J. C. & Fraaije, J. G. E. M. Lincs: a linear constraint solver for molecular simulations. *J. Comput. Chem.* **18**, 1463–1472 (1997).
74. Darden, T., York, D. & Pedersen, L. Particle mesh ewald: an n·log(n) method for ewald sums in large systems. *J. Chem. Phys.* **98**, 10089–10092 (1993).
75. Essmann, U. et al. A smooth particle mesh ewald method. *J. Chem. Phys.* **103**, 8577–8593 (1995).
76. Hess, B., Kutzner, C., van der Spoel, D. & Lindahl, E. Gromacs 4: algorithms for highly efficient, load-balanced, and scalable molecular simulation. *J. Chem. Theory Comput.* **4**, 435–447 (2008).
77. Carr, M. & MacPhee, C. E. Membrainy: a 'smart', unified membrane analysis tool. *Source Code Biol. Med.* **10**, 3 (2015).
78. Kang, L., Janowska, M. K., Moriarty, G. M. & Baum, J. Mechanistic insight into the relationship between N-terminal acetylation of α-synuclein and fibril formation rates by NMR and fluorescence. *PLoS ONE* **8**, e75018 (2013).

Acknowledgements

We acknowledge access to the Jülich-Düsseldorf Biomolecular NMR Center and thank the CSC–IT Center for Science, Finland, for computational resources. Financial supports from an Emmy Noether grant of the DFG ET103/2-1 to M.E. and an ERC consolidator grant to W.H. are gratefully acknowledged. T.V. and M.M.W. acknowledge support from the International Graduate School of Protein Science and Technology (iGRASP$_{seed}$) granted by the Ministry of Innovation, Science and Research of the state North Rhine-Westphalia. This work was supported by the DFG (HE 3243/4-1) and by the Ministry of Innovation, Science and Research within the framework of the NRW Strategieprojekt BioSC (BioSc seed fund) and the Strategische Forschungsfonds (SFF) of the Heinrich-Heine-University Düsseldorf. A.K.B. thanks the Parkinson's and Movement Disorder Foundation (PMDF) for funding. We thank Dr. Aldino Viegas for help with NMR data acquisition and Dr. Céline Galvagnion for fruitful discussions.

Author contributions

H.H., B.S., D.W., W.H., A.K.B., and M.E. designed the experiments. T.V., M.M.W., H.S., B.U., and C.P. performed the experiments. T.V., M.M.W., and C.P. analyzed the data. T.V. and M.E. wrote the manuscript. All authors commented on the manuscript.

Additional information

Supplementary Information accompanies this paper at https://doi.org/10.1038/s42003-018-0049-z.

Competing interests: The authors declare no competing interests.

Reprints and permission information is available online at http://npg.nature.com/reprintsandpermissions/

Publisher's note: Springer Nature remains neutral with regard to jurisdictional claims in published maps and institutional affiliations.

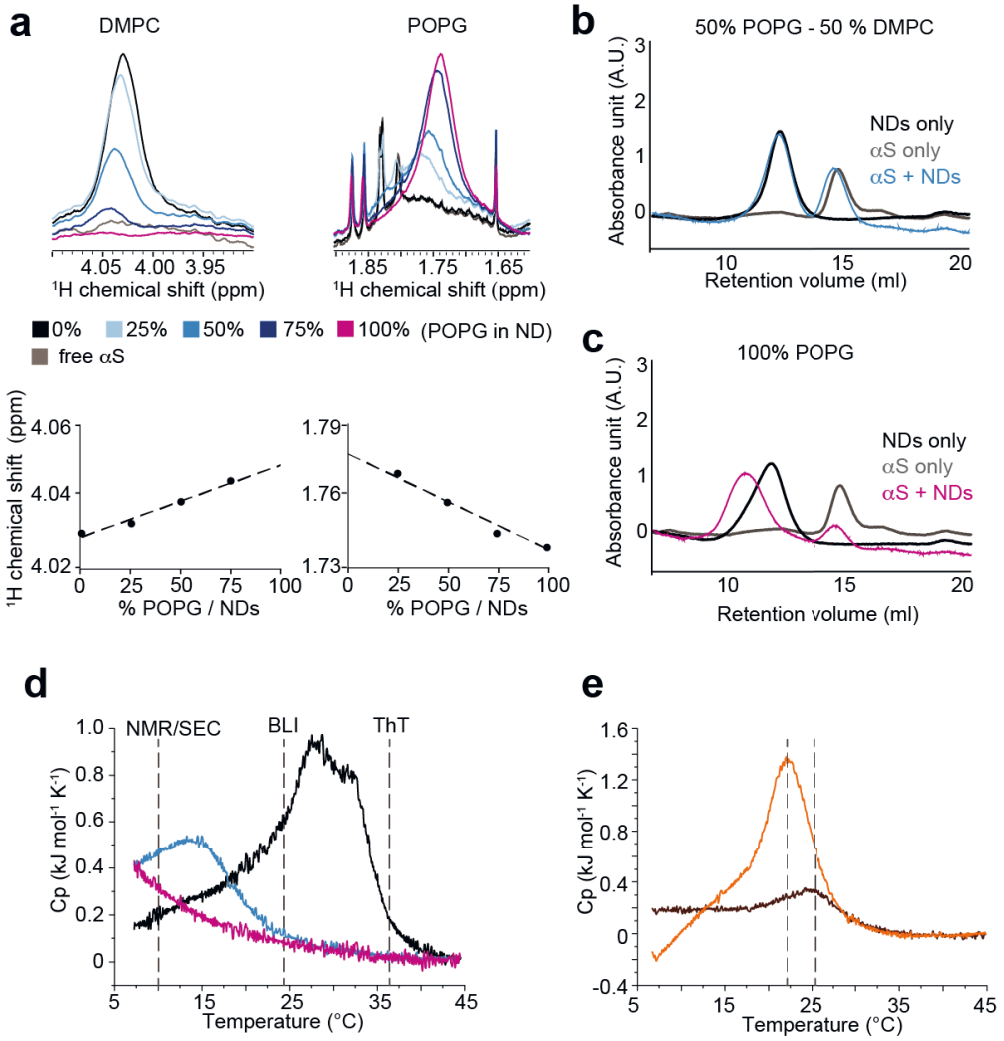

Supplementary Figure 1. Formation of lipid mixtures in NDs, lipid phase transitions and stability of αS association. (**a**) NMR ^{1}H-1D spectra of αS in the presence of NDs containing different POPG-to-DMPC ratios corresponding to the samples shown in Fig. 1a-b. Signals from either DMPC (left, choline methyl groups) or POPG (right, ^{1}H next to the unsaturation) are displayed. The volumes of the peaks reflect within an error of approximately 10% the aimed lipid compositions. In addition to volume changes also chemical shifts perturbations for both lipid specific peaks are visible and follow a rather linear dependence on the composition. The NMR data therefore report on both the presence and mixing of both lipid types in single nanodiscs. (**b**) Size exclusion chromatography (SEC) profiles (Superdex 200 13/300 gl, GE Healthcare) of αS alone (grey), 50% POPG NDs alone (black) and both after mixing (same amounts as in the isolated case) and incubation for 24h at room temperature (blue). The clear separation of αS from NDs in the mixture points to a fast-kinetic exchange between free and bound αS. The conserved total absorbance additionally confirms the stability of the NDs in the presence of αS. (**c**) Same as in (b) but using 100% POPG NDs. The SEC profile of the mixture of αS with 100% POPG NDs shows a clear reduction of free αS and a size increase of the ND peak, pointing to a strong interaction between the two components. (**d**) Differential scanning calorimetry (DSC) thermograms of nanodiscs prepared with either 100% DMPC (black), 100% POPG (purple) or a 50%-50% mixture thereof (blue), showing phase transitions temperatures around 28°C, below 5°C and 13°C, respectively. Temperatures at which different measurements were performed are highlighted. (**e**) DSC profile of 100% DMPG NDs in the absence (brown) or presence of 2 molar equivalent αS (orange). While the presence of αS leads to a lower phase transition temperatures of the lipid bilayer, in line with what was reported using SUVs[1], the transition temperature differences is much smaller for NDs (ΔT_m=2.5 °C) as compared to SUVs (ΔT_m=11 °C) in line with an increase stability of the NDs. Note that a more detailed discussion of the stability of the nanodiscs is given in the Supplementary Note 1 (*vide infra*).

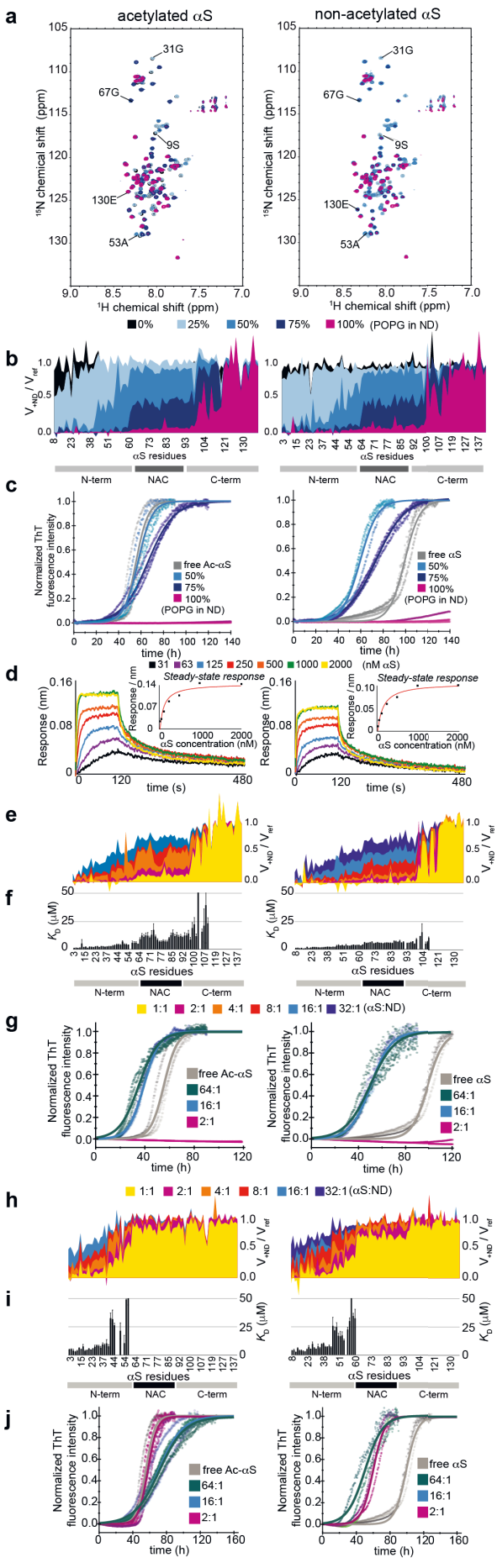

Supplementary Figure 2. N-terminal acetylation has moderate effect on membrane association and leads to different behavior in aggregation assays. Comparison of data recorded on acetylated αS (left hand side) and non-acetylation αS (right hand side). Note that data of acetylated αS represents the data shown in the main manuscript and is just added to facilitate a direct comparison. (**a**, *analog Fig. 1a*) [^{15}N-^{1}H]-TROSY-HSQC NMR spectra in the absence (grey) or in the presence of 25 μM NDs containing an increasing amount of anionic lipids. **(b**, *analog Fig. 1b,c***)** Corresponding NMR attenuation profiles, i.e. the ratio of peak volumes in the presence and absence of NDs, are plotted against αS primary sequence. In line with previous findings[9], N-terminal acetylation leads to clear chemical shift perturbations in the NMR spectra for the first 10 residues of αS. The peaks which are already shifted in free αS due to the acetylation are also the ones that are affected most by the presence of nanodiscs with low amount of charges (close to physiological concentration). Data show rather small but significant increase in the membrane association of the first 15 residues due to the N-terminal acetylation, which is in line with previous observation using SUVs[10,11]. αS acetylation is known to increase N-terminal helix propensity[9,12], which may facilitate formation of the initial binding mode and be of significance for naturally occurring processes.

(**c**, *analog Fig. 1e*) αS aggregation assays (normalized ThT fluorescence) in the absence and presence of NDs with indicated POPG content. While aggregation behavior in the presence of NDs is in general very similar for acetylated and non-acetylated αS in all tested conditions, it is very different in the absence of NDs. In the absence of NDs the ThT kinetic data of non-acetylated αS reproducibly have a strongly delayed reference kinetic curve under the applied conditions as compared to the acetylated reference. In the setup used, primary nucleation processes are likely to happen at the air-water or plate-water interface[13,14], thus a lower hydrophobic propensity of non-acetylated αS could explain this effect. While this may be the dominant process in the absence of lipids, it may not be the case anymore in the presence of NDs [1], either because NDs shield these interfaces or because nucleation happens primarily at the membrane surface. The much lower differences due to acetylation state in the presence of NDs fit this explanation, as well as additional tests we ran using different types of plates (data not shown). Higher order processes, namely different fragmentation behaviors, can however not be excluded.

(**d**, *analog Fig. 3a*) BLI data with immobilized 100% POPG NDs. BLI kinetics show a (slightly) higher membrane affinity of the acetylated (K_D of 67 ± 17 nM) than the non-acetylated αS (K_D of 95 ± 14 nM).

(**e+f**, *analog Fig. 3b+c*) NMR titration data with 100% POPG NDs show a slightly increased membrane affinity of the NAC region for the non-acetylated αS. At current stage, it is not easy to explain why a modification at the N-terminus will affect the lipid interaction of a protein region that is sequentially separated by roughly 60 residues. Such a behavior could however either be related to intermolecular interactions and/or long range intramolecular interactions (in a 'horseshoe'-conformation) that may or may not be artificially introduced by the limited surface area of the NDs.

(**g**, *analog Fig. 3d*) Normalized ThT fluorescence kinetic curves for selected αS-to-ND ratios using 100% POPG NDs.

(**h+i**, *analog Fig. 3f+g*) NMR titration data with 50% POPG NDs show similar affinities of N-terminal residues for acetylated and non-acetylated αS.

(**j**, *analog Fig. 3h*) Normalized ThT fluorescence kinetic curves for selected αS-to-ND ratios using 50% POPG NDs.

Overall, it appears that the biggest effect of acetylation on aggregation is related to assay parameters that are normally not the matter of interest, which nevertheless may be important for future studies[15]. Still the results from systematic measurement of the effects of N-terminal acetylation via different methods point to subtle changes in membrane interaction in respect to NAC region specific affinities at high lipid charge densities as well as to N-terminal binding at a lipid charge density comparable with the overall composition found for membranes in e.g. synaptic vesicles[16].

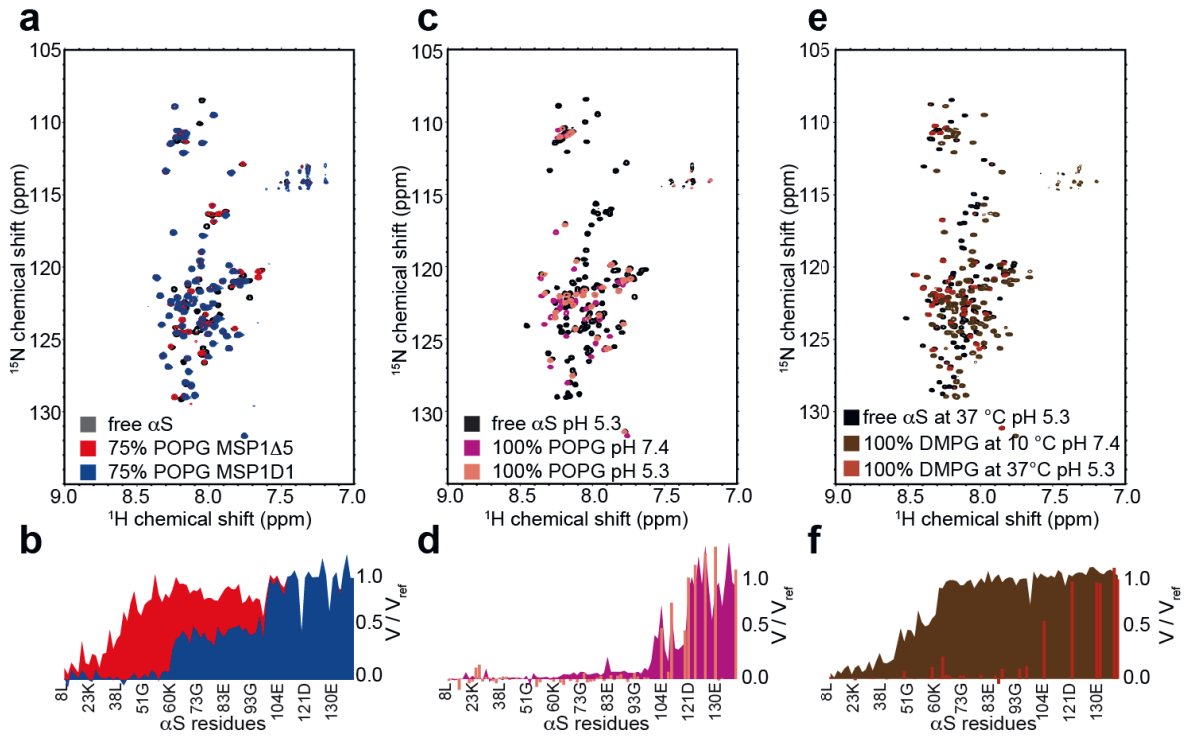

Supplementary Figure 3. αS-ND interactions using different MSP constructs, lower pH and higher temperature. NMR spectra (**a**) and the respective attenuation profiles (**b**) of [^{15}N]-acetylated-αS (50 μM) in the absence or in the presence of 25 μM NDs with 75% POPG content, assembled using the regular MSP1D1 construct (blue) or with the smaller MSP1Δ5 (red). Spectra (**c**) and attenuation profiles (**d**) corresponding to the binding of αS to NDs containing 100% POPG lipids at pH 7.4 (purple) and pH 5.3 (pale orange). Transferable assignments (bars) show that no significant difference in binding mode is visible upon pH variation. Spectra (**e**) and attenuation profiles (**f**) corresponding to the binding of αS to NDs containing 100% DMPG lipids in their gel phase (10°C, brown) or their fluid phase (37°C, red). Since normally measurement at 37 °C leads to considerable peak loss of N-terminal αS residues due to water exchange processes, the spectrum was recorded at pH 5.3 (counteracting water exchange). Note that the pH shift alone has no significant effect on binding (see (**c**) and (**d**)). Reference spectra of respective free αS are shown in dark grey. Note that a more detailed discussion about the NMR detection of the membrane-bound state is given in the Supplementary Note 2 (*vide infra*).

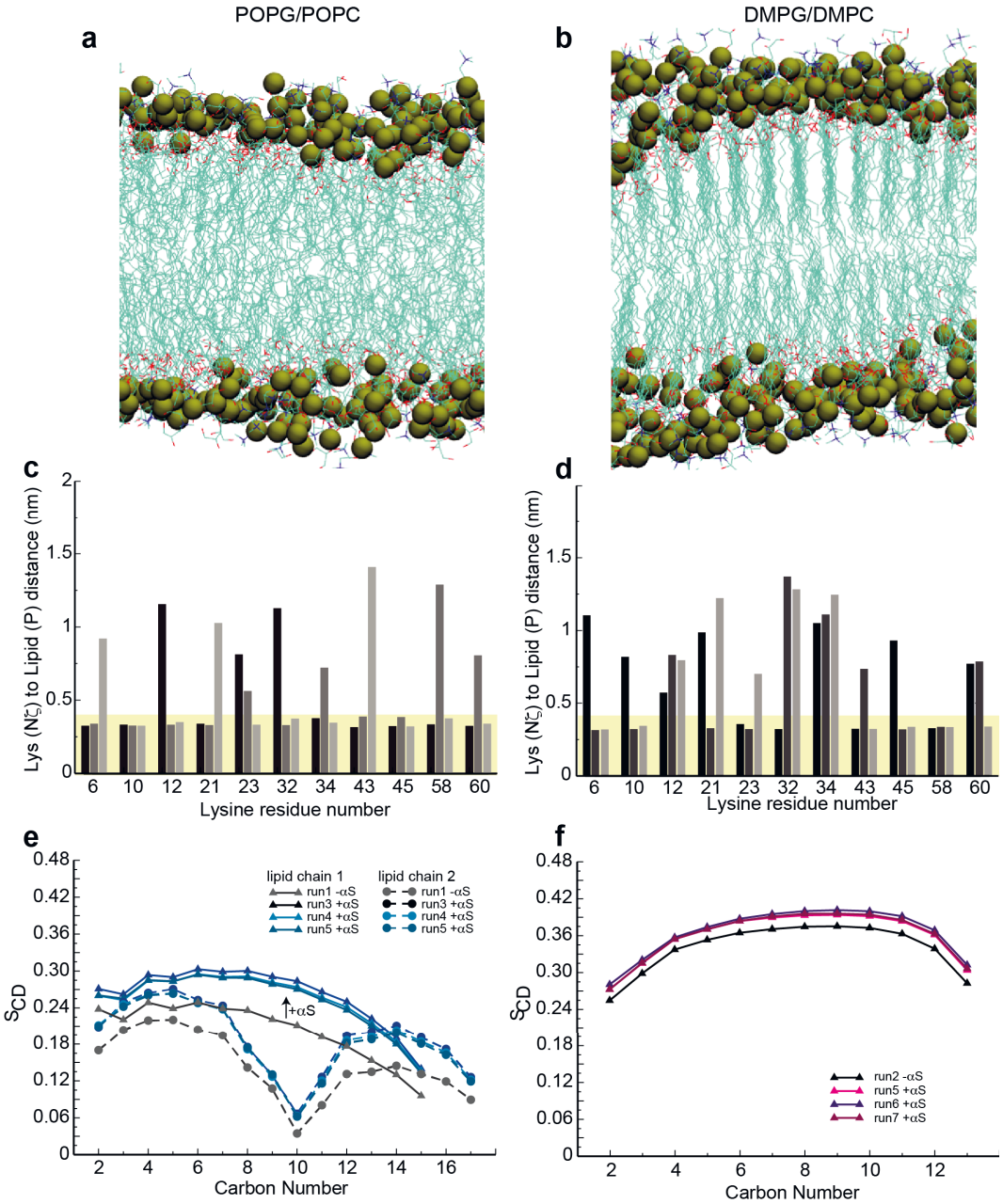

Supplementary Figure 4. Lipid properties and αS-membrane interactions as seen by MD simulations. (**a,b**) Molecular arrangement of lipid bilayer in the absence of αS for POPG/POPC lipids in fluid phase (**a**) and DMPG/DMPC lipids in gel phase (**b**) (end of run1/run2, Table S2). (**c,d**) Distances for indicated lysine residues from Lys-Nξ to the phosphorus atom of the next anionic lipid as found in different runs of MD simulations for POPG/POPC (c, individual bars for run3-5, Table S2) and DMPG/DMPC (d, individual bars for run5-7, Table S2) membranes. Distances that could promote lipid-mediated salt bridges are highlighted in yellow. (**e,f**) Calculated order parameters for indicated carbon atoms of the lipid fatty acids with and without αS for POPG/POPC (**e**) and DMPG/DMPC (**f**) membranes.

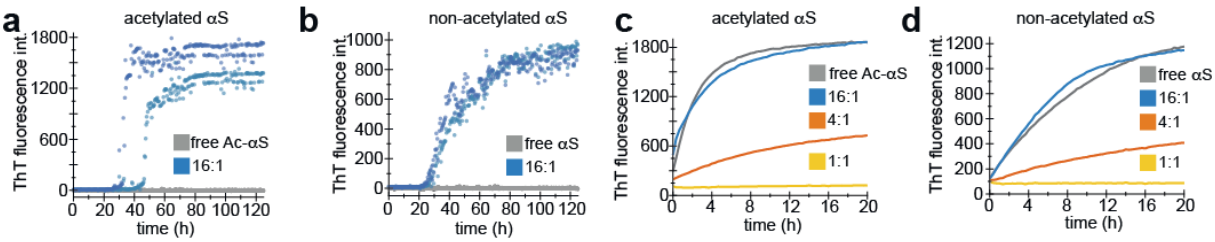

Supplementary Figure 5. Amyloid fibril nucleation and elongation in the presence of 100% POPG ND. (**a,b**) Quiescent nucleation assay of acetylated αS (**a**) and non-acetylated αS (**b**) in the absence (grey, duplicates) and presence of 100% POPG NDs (duplicates in light and dark blue, note that conditions shown in (a) are identical to those shown in Fig. 3e). (**c,d**,) Raw data of quiescent ThT fluorescence aggregation assay in the presence of 2.5% preformed seeds for acetylated (c) or non-acetylated (d) αS for different molar ratios (see color code) of 100% POPG NDs. While at high molar excess of αS (16:1, αS-to-ND), according to our NMR data, nearly all αS monomers should interact through their most N-terminal regions with the NDs, no significant effect on the elongation rate was observed (c,d, blue). At molar ratios of 4:1 (orange) a decrease in elongation is observed, however at this ratio our NMR data clearly indicate that all αS monomers are interacting with the NDs. Nevertheless, in both cases (molar ratios of 16:1 and 4:1) larger fractions of the monomer population should still have accessible NAC regions, which may explain their ability to participate in the fibril elongation process. However, the limited interaction surface may also influence the dynamic nature of membrane association leading to a certain population of free monomeric αS at any given time.

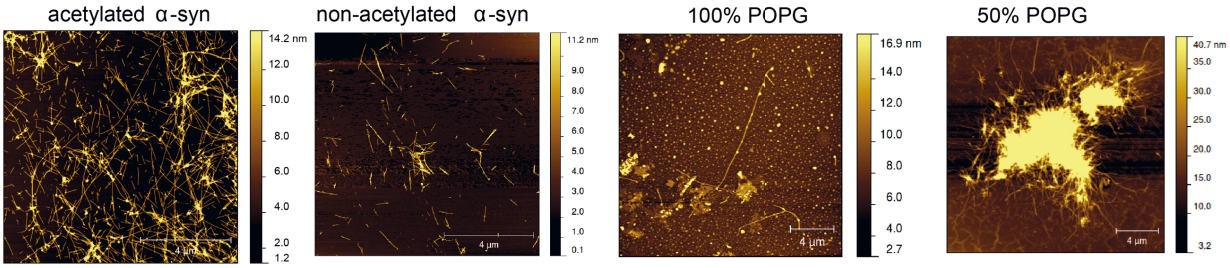

Supplementary Figure 6. αS fibrils grown in the absence and presence of NDs have similar morphologies. AFM images of αS amyloid fibrils formed using acetylated αS and non-acetylated αS as well as acetylated αS in the presence of NDs with indicated lipid composition (from left to right). While no in depth AFM characterization is attempted here, our data indicates that the morphology of all tested samples is rather similar (mostly mature fibrils), in contrast to previous results reported for aggregation in the presence of liposomes[1] (thin and curly fibrils). This observation suggests that the interplay between the lipids and the αS and potential incorporation of lipids into fibrils is different in the case of nanodiscs (in line with a more stable environment compared to liposomes).

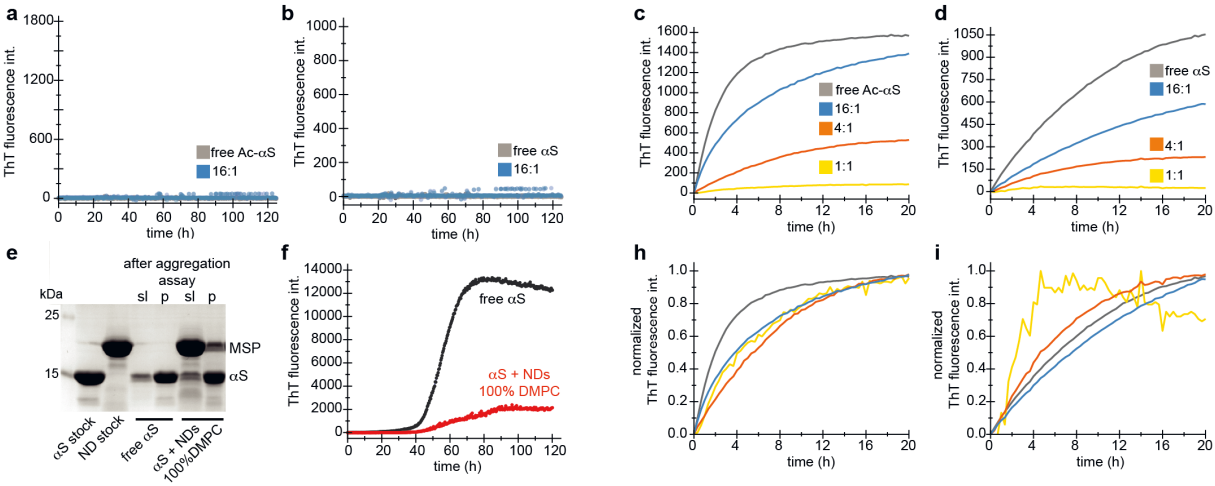

Supplementary Figure 7. Amyloid fibril nucleation and elongation in the presence of 50% POPG ND and rationale for normalization of ThT data. (**a,b**) Quiescent nucleation assay of acetylated αS (**a**) and non-acetylated (**b**) αS in the absence (grey) and presence of 50% POPG NDs (conditions analogous to data shown in Fig. S5, for 100% POPG NDs). (**c,d**,) Seeded aggregation assays under conditions analogous to data shown in Fig. S5, but using 50% POPG NDs. Surprisingly, the 50% charged NDs do show an effect on the ThT signal as a reporter for fibril elongation in seeded experiments. This data is difficult to explain given that elongation is, in all cases of amyloid formation, responsible for the generation of the bulk of fibril mass. Hence, its inhibition should slow down the overall aggregation kinetic, also under non-seeded conditions. Noteworthy, we observe that ThT signal intensity can be strongly affected by the presence of NDs and that the absolute ThT intensity does not correlate with absolute fibril mass when comparing data recorded in the absence or presence of NDs. This is visible by comparing SDS-PAGE results (**e**) with ThT intensities (**f**) of identical samples. After the aggregation assay the αS-band for soluble (sl) and insoluble (p) protein show very similar intensities in the absence and presence of 100% DMPC NDs. Although our NMR data show that these NDs do not interact with the αS, the corresponding ThT signal (of the identical samples) show very different intensities (f). It is therefore possible that the ThT (unspecifically) interacts with NDs, leading to an overall decrease in ThT intensities. Furthermore, it is possible that the attachment of ND to the growing fibrils interferes with efficient binding of ThT. We therefore normalized most ThT assays. Noteworthy, this effect is less pronounced for ND with 100% POPG (as e.g. visible in the data in Fig. S5), which could be due to the high coverage of the lipid surface by αS molecules that may reduce the unspecific ThT-ND interactions. In line with our other data recorded using 50% POPG NDs, albeit significantly reduced ThT sensitivity, only very moderate effects of the NDs on the fibril elongation process are visible after normalizing ThT intensities in the seeded aggregation assays (**h,i**).

αS type	pH	MSP type	Lipids in ND	αS-to-ND ratio	Used for data in
acetylated	5.3	-	-	-	Fig. S3c,e black
	7.4	-	-	-	Fig. S3a black
		D1	100% DMPC	2:1	Fig. 1a,b black
			25% POPG – 75% DMPC	2:1	Fig. 1a,b light blue
			50% POPG – 50% DMPC	1:1	Fig. 5g, yellow
				2:1	Fig. 1a,b blue Fig. 5g, purple
				4:1	Fig. 5g, orange
				8:1	Fig. 5g, red
				16:1	Fig. 5g, blue
			75% POPG – 25% DMPC	2:1	Fig. 1a,b dark blue
		D5			Fig. S3a,b red
		D1	100% POPG	1:2	Not shown
				1:1	Fig. 5b, yellow
				2:1	Fig. 1a,b purple Fig. 5b, purple Fig. S3c,d purple
	5.3			2:1	Fig. S3c,d, orange
				4:1	Fig. 5b, orange
				8:1	Fig. 5b, red
				16:1	Fig. 5b, blue
			100% POPC	2:1	Fig. 3a, dark grey
			50% POPG – 50% POPC		Fig. 3a, yellow
			50% DMPG – 50% POPC		Fig. 3a, green
			50% DMPG – 50% DMPC		Fig. 3a, beige
			100% DMPG		Fig. 3a, brown
non-acetylated	7.4	-	-	-	Fig. S2a, grey
		D1	100% DMPC	2:1	Fig. 1c, black Fig. S2a, black
			25% POPG – 75% DMPC	2:1	Fig. 1c, light blue Fig. S2a, light blue
			50% POPG – 50% DMPC	1:1	Fig. S2h, yellow
				2:1	Fig. 1c, blue Fig. S2a, blue Fig. S2h, purple
				4:1	Fig. S2h, orange
				8:1	Fig. S2h, yellow
				16:1	Fig. S2h, blue
				32:1	Fig. S2h, dark blue
			75% POPG – 25% DMPC	2:1	Fig. 1c, dark blue Fig. S2a, dark blue
			100% POPG	1:1	Fig. S2e, yellow
				2:1	Fig. 1c, purple Fig. S2a, purple Fig. S2e, purple
				4:1	Fig. S2e, orange
				8:1	Fig. S2e, red
				16:1	Fig. S2e, blue
				32:1	Fig. S2e, dark blue

Supplementary Table 1. Summary of NMR samples used in the study.

Membrane models	Systems	αS initial distance to the membrane surface (nm)	Time (ns)
POPC/POPG*	RUN1	-	500
DMPC/DMPG*	RUN2	-	1000
POPC/POPG	RUN3	0.5	1000
	RUN4	0.5	1000
	RUN5	1.5	1000
DMPC/DMPG	RUN6	0.5	1000
	RUN7	1.5	1000
	RUN8	1.5	1000

Supplementary Table 2. Summary of MD simulations used for the study.

Supplementary Note 1: Stability consideration of the lipid bilayer nanodiscs

While contradicting results on structural integrity of liposomes in the presence of αS have been reported, it seems that under conditions similar to our study, αS can rather quickly disrupt (POPG-based) vesicles or supported bilayers[2,3]. Therefore, it may be difficult in the obtained results to distinguish between effects that originate from interaction with (curved) intact bilayers or effects that are caused by lipid dissociation/ rearrangements. It can be expected that the presence of the scaffold protein protects the lipid bilayer to some extent from rearrangement and indeed our DSC data (Fig. S1e) suggest that the lipids in NDs are less affected by the presence of αS as compared to SUVs. This data, however, do not suffice to fully justify the assumption of an unchanging bilayer during the time course of the experiment. Noteworthy, it has also been reported that due to its amphipathic properties αS can encircle lipid bilayers in a similar way as the membrane scaffold protein and can form nanodiscs of slightly larger size[4,5]. Therefore, although thermodynamically unlikely, one cannot directly exclude the possibility that αS replaces the MSP to some extend during the experiments. However, as discussed in the following, our results strongly suggest that the NDs are stable during the time-course of the interaction experiments.

For moderately negatively charged nanodiscs (50% POPG) one strong indicator is the size exclusion chromatography data recorded after prolonged incubation (Fig. S1b). This data shows (in a quantitative way) that αS does not disrupt a detectable fraction of NDs within 24 h. Additionally the gradual increase of binding interface with increased charge density suggest that the recorded data report on α-Synuclein's interaction with the membrane surface (lipid head groups) and not on the 'encircling' of the hydrophobic acetyl chains. This aspects is valid for all NDs from 0-75% anionic lipid content.

For highly charged nanodiscs (100% POPG), resembling the 100% POPS used in[4] the interpretation of the SEC profile (see Fig. S1c) is more difficult. NDs and αS co-elute at a lower retention volume, this could either be explained by a replacement of the scaffold protein by αS in nanodiscs (forming larger discs, as reported in[4]) or by a decreased interaction with the SEC material arising from tightly bound αS molecules with a significant protruding region (residues 98 to 140). Our BLI measurements with immobilized 100% POPG NDs, however, show a clear full recovery of the signal after αS binding and release (Fig. 5a, Fig. S2d). Since only the MSP and not the αS is immobilized on the tip, this data show that during the time course of the experiment no disruption and/or MSP displacement and/or larger lipid rearrangement occur due to the presence of strongly interacting αS. Overall these data, in combination with the overall consistency of the data measured during the time course of several days, strongly indicates that the different experiments recorded on the different ND preparations report predominantly on the interaction with a stable planar bilayer.

While the stability assumption seems valid for all interaction studies, it is at this point not fully clear whether this also holds true for the aggregation assays. It has been shown that lipids from vesicles and reconstituted planar bilayers can be incorporated into fibrils during the aggregation process[3,6], which might be an important process for the toxicity of αS oligomers, forming pores in membranes[7,8]. Our AFM data do not show clear differences in morphologies (Fig. S6) as have been observed under similar conditions for aggregation assays in the presence of SUVs[1], suggesting that no/less lipids are incorporated into the αS fibrils. Native gels recorded after the aggregation assay do show intact NDs (data not shown), however denaturing gels after the aggregation also show some MSPs in the insoluble fraction, possibly indicating co-aggregation to some extent (Fig. S7e). In general, the consistency between the interaction studies and the visible effects in the aggregation assays suggest that the interaction with stable bilayers does have a considerable effect during the aggregation, however additional effects from lipid incorporation/rearrangements during the aggregation assays cannot be excluded.

Supplementary Note 2: Considerations regarding solution NMR detection of membrane-bound state

It is worth noting that the solution NMR results described in the manuscript refer to the decrease in peak intensity as a reporter for interactions, which is in line with the effects seen before using SUVs[17]. While it is clear that SUVs have particle sizes (associated with slow tumbling rates) well above the detection limit of conventional solution NMR techniques, the smaller size of the NDs system should, in principle, allow detection of NMR signals, as has been reported before for several ND-bound or ND-integrated proteins[18]. Nonetheless, neither the usage of Transverse Relaxation Optimized Spectroscopy (TROSY)[19] with increased signal accumulation (i.e. 10-fold longer as for spectra shown in Fig. 1a) nor the measurement at increased temperatures (35°C) and the usage of an NMR-optimized smaller membrane scaffold protein (MSP1D1ΔH5)[20] forming NDs of smaller size and higher tumbling rates, resulted in appearance of a new set of peaks indicative for the bound sate (and the presence of slow exchange processes) or a collective shift of peaks indicative of fast on-off exchange processes (Fig. S3).

In theory, three effects may explain this observation and obstruct detection of the ND-bound residues of αS: (i) the bound-to-free exchange rate is in the order of the NMR time scale (so-called intermediate exchange), (ii) the presence of a non-negligible part of αS protruding out of the ND (namely at least residues 98-140), slowing down molecular tumbling and increasing relaxation leading to line broadening beyond the detection limit, and/or (iii) membrane-bound αS shows a significant amount of plasticity leading to inhomogeneous broadening of the NMR lines.

While intermediate exchange can be largely ruled out due to the observed binding kinetics (BLI results, Fig. 5a, t_{on} and t_{off} of around 4 $\mu s \cdot M$ and 65 s, respectively) it is at this point difficult to further distinguish between slower tumbling and molecular plasticity (or a combination thereof) that interfere with solution NMR detection of the bound conformation.

Supplementary Note 3: Generation of structural models of aS nanodiscs interaction

Atomic coordinate files (.pdb-files) of nanodiscs with the appropriate lipids and scaffold protein were generated using the Charmm nanodiscs builder module[21]. αS with ideal α-helical secondary structure for regions interacting with the NDs was generated using the builder module in pymol (The PyMOL Molecular Graphics System, Version 1.7 Schrödinger, LLC.). The interacting regions reflect respective solution NMR attenuation profiles and secondary structure is in line with DNP solid-state NMR data. No distance restrains or additional structure calculation algorithms were used. The benefits of the resulting structural model are that it rather accurately reflects the respective molecular sizes, e.g. length of elongated helixes in respect to nanodisc diameter or molecular crowding on the nanodisc surface.

Supplementary References

1. Galvagnion, C. et al. Lipid vesicles trigger alpha-synuclein aggregation by stimulating primary nucleation. *Nat. Chem. Biol.* **11**, 229-234 (2015).
2. Fusco, G. et al. Structural basis of synaptic vesicle assembly promoted by alpha-synuclein. *Nat. Commun.* **7**, 12563; DOI:10.1038/ncomms12563 (2016).
3. Reynolds, N.P. et al. Mechanism of membrane interaction and disruption by alpha-synuclein. *J. Am. Chem. Soc.* **133**, 19366-19375 (2011).
4. Eichmann, C. et al. Preparation and characterization of stable alpha-synuclein lipoprotein particles. *J. Biol. Chem.* **291**, 8516-8527 (2016).
5. Eichmann, C., Kumari, P. & Riek, R. High-density lipoprotein-like particle formation of synuclein variants. *FEBS Lett.* **591**, 304-311 (2017).
6. Hellstrand, E., Nowacka, A., Topgaard, D., Linse, S. & Sparr, E. Membrane lipid co-aggregation with alpha-synuclein fibrils. *PLoS One* **8**, e77235; DOI:10.1371/journal.pone.0077235 (2013).
7. Auluck, P.K., Caraveo, G. & Lindquist, S. alpha-Synuclein: membrane interactions and toxicity in Parkinson's disease. *Annu. Rev. Cell Dev. Biol.* **26**, 211-233 (2010).
8. Butterfield, S.M. & Lashuel, H.A. Amyloidogenic protein-membrane interactions: mechanistic insight from model systems. *Angew. Chem. Int. Ed. Engl.* **49**, 5628-5654 (2010).
9. Maltsev, A.S., Ying, J. & Bax, A. Impact of N-terminal acetylation of alpha-synuclein on its random coil and lipid binding properties. *Biochem.* **51**, 5004-5013 (2012).
10. Dikiy, I. & Eliezer, D. N-terminal acetylation stabilizes N-terminal helicity in lipid- and micelle-bound alpha-synuclein and increases its affinity for physiological membranes. *J. Biol. Chem.* **289**, 3652-3665 (2014).
11. Bartels, T., Kim, N.C., Luth, E.S. & Selkoe, D.J. N-alpha-acetylation of α-aynuclein increases its helical folding propensity, GM1 binding specificity and resistance to aggregation. *PLoS ONE* **9**, e103727; DOI:10.1371/journal.pone.0103727 (2014).
12. Kang, L., Janowska, M.K., Moriarty, G.M. & Baum, J. Mechanistic insight into the relationship between N-terminal acetylation of α-synuclein and fibril formation rates by NMR and fluorescence. *PLoS ONE* **8**, e75018; DOI:10.1371/journal.pone.0075018 (2013).
13. Vacha, R., Linse, S. & Lund, M. Surface effects on aggregation kinetics of amyloidogenic peptides. *J. Am. Chem. Soc.* **136**, 11776-11782 (2014).
14. Campioni, S. et al. The presence of an air-water interface affects formation and elongation of alpha-synuclein fibrils. *J. Am. Chem. Soc.* **136**, 2866-2875 (2014).
15. Iyer, A. et al. The impact of N-terminal acetylation of alpha-synuclein on phospholipid membrane binding and fibril structure. *J. Biol. Chem.* **291**, 21110-21122 (2016).
16. Fusco, G. et al. Direct observation of the three regions in alpha-synuclein that determine its membrane-bound behaviour. *Nat. Commun.* **5**, 3827; DOI:10.1038/ncomms4827 (2014).
17. Bodner, C.R., Dobson, C.M. & Bax, A. Multiple tight phospholipid-binding modes of alpha-synuclein revealed by solution NMR spectroscopy. *J. Mol. Biol.* **390**, 775-790 (2009).
18. Viegas, A., Viennet, T. & Etzkorn, M. The power, pitfalls and potential of the nanodisc system for NMR-based studies. *Biol. Chem.* **397**, 1335-1354 (2016).
19. Pervushin, K., Riek, R., Wider, G. & Wuthrich, K. Attenuated T2 relaxation by mutual cancellation of dipole-dipole coupling and chemical shift anisotropy indicates an avenue to NMR structures of very large biological macromolecules in solution. *Proc. Natl. Acad. Sci. U. S. A.* **94**, 12366-12371 (1997).
20. Hagn, F., Etzkorn, M., Raschle, T. & Wagner, G. Optimized phospholipid bilayer nanodiscs facilitate high-resolution structure determination of membrane proteins. *J. Am. Chem. Soc.* **135**, 1919-1925 (2013).
21. Jo, S., Kim, T., Iyer, V.G. & Im, W. CHARMM-GUI: A Web-based Graphical User Interface for CHARMM. *J. Comput. Chem.* **29**:1859-1865 (2008).

Biophysical Journal
Article

Biophysical Society

DNP-Enhanced MAS NMR: A Tool to Snapshot Conformational Ensembles of α-Synuclein in Different States

Boran Uluca,[1,2] Thibault Viennet,[1,2] Dušan Petrović,[1] Hamed Shaykhalishahi,[1,2] Franziska Weirich,[1,2] Ayşenur Gönülalan,[1] Birgit Strodel,[1,3] Manuel Etzkorn,[1,2] Wolfgang Hoyer,[1,2] and Henrike Heise[1,2,*]
[1]Institute of Complex Systems, Structural Biochemistry, Research Center Jülich, Jülich, Germany, [2]Institute of Physical Biology, and [3]Institute of Theoretical and Computational Chemistry, Heinrich-Heine-University Düsseldorf, Düsseldorf, Germany

ABSTRACT Intrinsically disordered proteins dynamically sample a wide conformational space and therefore do not adopt a stable and defined three-dimensional conformation. The structural heterogeneity is related to their proper functioning in physiological processes. Knowledge of the conformational ensemble is crucial for a complete comprehension of this kind of proteins. We here present an approach that utilizes dynamic nuclear polarization-enhanced solid-state NMR spectroscopy of sparsely isotope-labeled proteins in frozen solution to take snapshots of the complete structural ensembles by exploiting the inhomogeneously broadened line-shapes. We investigated the intrinsically disordered protein α-synuclein (α-syn), which plays a key role in the etiology of Parkinson's disease, in three different physiologically relevant states. For the free monomer in frozen solution we could see that the so-called "random coil conformation" consists of α-helical and β-sheet-like conformations, and that secondary chemical shifts of neighboring amino acids tend to be correlated, indicative of frequent formation of secondary structure elements. Based on these results, we could estimate the number of disordered regions in fibrillar α-syn as well as in α-syn bound to membranes in different protein-to-lipid ratios. Our approach thus provides quantitative information on the propensity to sample transient secondary structures in different functional states. Molecular dynamics simulations rationalize the results.

INTRODUCTION

Intrinsically disordered proteins (IDPs) are characterized by their high degree of conformational freedom, which is due to a rather flat free energy landscape, comprising low energy barriers and many local minima. These allow IDPs to fluctuate rapidly over an ensemble of conformations in solution instead of adopting a well-defined three-dimensional structure (1–5). The structural heterogeneity of IDPs is closely related to their biological functions, e.g., in signaling and regulation (6). Essential biological processes rely on IDPs and elucidating the link between composition of the conformational ensemble and function is required for a complete comprehension of IDPs.

For studying conformational ensembles of IDPs, both experimental and computational methods have been developed in recent years. On the experimental side, far-ultraviolet circular dichroism is used for the determination of secondary structure content of proteins in solution, small-angle x-ray scattering (SAXS) can provide overall dimensions and shape of the molecules, and fluorescence resonance energy transfer and electron paramagnetic resonance spectroscopy can provide quantitative distance distributions (7–11). On the theoretical side, a number of methods have evolved in recent years to overcome two of the main problems of molecular dynamics (MD) simulations of IDPs: the lack of conformational sampling due to hardware restraints, and the limited performance of available force-field parameters for representation of the protein ensemble (12–14).

A well-established experimental method for studying structure, dynamics, and function of IDPs is solution NMR spectroscopy. NMR chemical shifts and residual dipolar couplings are sensitive to conformational sampling of IDPs. Conformational ensembles of IDPs were previously studied by generating large arrays of molecules by Monte Carlo-based methods and subsequently selecting

Submitted November 27, 2017, and accepted for publication February 7, 2018.

*Correspondence: h.heise@fz-juelich.de

Editor: Jill Trewhella.

https://doi.org/10.1016/j.bpj.2018.02.011

conformers in agreement with predicted NMR parameters (15–22), or by MD simulations using experimental data as restraints (23). Furthermore, longitudinal relaxation rate dispersion profiles of protein protons at low magnetic fields give information on long-range correlated motions in IDPs (24).

Studying the proportion of secondary structure motifs of an IDP is impeded by conformational averaging on the timescales of many biophysical methods, and conformational distributions in many cases can be detected only indirectly. We therefore use an approach that allows simultaneous observation of the entire conformational ensemble and quantification of the amount of transient secondary structure sampled. For this aim, the sample is frozen in solution, and hyperpolarized solid-state NMR (ssNMR) experiments are performed at cryogenic temperatures as low as 100 K (25–29). In such a frozen solution, the molecules are statistically trapped in different conformations and consequently, a continuum of chemical shifts is observed for each nucleus. The obtained spectrum reflects the entire conformational ensemble covered, representing a snapshot of its momentary composition (27). Changes in composition of the structural ensemble due to different functional states of the IDP can be tracked by this method, which is applied here on the IDP α-synuclein (α-syn).

The 140 amino-acid-residue protein α-syn possesses a remarkable conformational flexibility. α-Syn is able to adjust its conformation to the environmental conditions and is thus called a "protein-chameleon" (30). Its natural function is supposed to involve membrane and lipid vesicle binding, driven by the properties of lipids (mainly headgroups' charge density), and inducing α-helical structural features (31). This propensity is thought to play a role in SNARE-like vesicle fusion mechanisms (32–34). Membrane binding of α-syn critically depends on membrane properties, such as curvature and charge, as well as molecular crowding. Different membrane affinities have been determined for different regions of the protein (35).

Moreover, it is well established that α-syn can adopt β-strand conformations along the energetically favorable pathway of protein aggregation and fibril formation (36). At least five different polymorphic forms have been observed for α-syn amyloid fibrils (37–40). The conformational characteristics of the heterogeneously structured α-syn are not yet completely understood. Aggregation of α-syn into amyloid fibrils is linked to a number of neurodegenerative diseases, known as synucleopathies, of which the most widely known is Parkinson's disease (41). As the conformational ensembles of IDPs critically report on their propensities to form transient secondary structural elements and thus may predict early aggregation and membrane binding events, monomeric α-syn has been extensively studied (42). The intrinsically disordered monomer was found to be stabilized by long-range intramolecular contacts between the C terminus and the hydrophobic center region of the protein (43), and β-strand propensities in monomeric α-syn were found to correlate well with β-sheet regions in mature fibrils (44).

In this work, we studied different conformational ensembles of the IDP α-syn in frozen solution. The study was performed on recombinantly expressed α-syn in its monomeric, fibrillar, and membrane-associated forms. Additionally, we quantified the amount of α-helical secondary structure features in α-syn bound to membranes in different protein-to-lipid ratios. As ssNMR spectra of diluted biological samples suffer from low sensitivity, we made use of dynamic nuclear polarization (DNP) for signal enhancement (45–48). To reduce spectral overlap in the inhomogeneously broadened NMR spectra, α-syn was expressed using the previously described TEASE labeling strategy (Fig. 1 *a*), simplifying ^{13}C-^{13}C spectra to valine Cα/Cβ and leucine Cβ/Cγ correlations (49). We used the backbone chemical shifts of the 19 valine residues as a reporter for the conformational ensemble of α-syn. Furthermore, we explored the valine conformational ensemble and chemical shifts from MD simulations with different force fields and solvent models.

MATERIALS AND METHODS

Recombinant expression and purification of α-syn

α-Syn was expressed recombinantly in *Escherichia coli* cells from pT7-7, as described previously (50). The labeling strategy, adopted from the TEASE approach (49), was applied by growing cells in M9 minimal medium containing [2-^{13}C]-glucose and $^{15}NH_4Cl$ as sole carbon and nitrogen sources. The ^{13}C labeling of the amino acids Phe, Gln, Glu, Pro, Asn, Asp, Met, Thr, Lys, and Ile was suppressed by supplementing sufficient quantities (150 μg/mL of each) of these unlabeled amino acids to the expression media. The cells were harvested 4 h after inducing with IPTG to a final concentration of 1 mM. Harvesting was followed by cell lysis performed by sonication in lysis buffer (20 mM Tris-HCl, 1 mM EDTA, pH 8.0). Purification of α-syn started with ammonium sulfate precipitation at 4°C for 15 min under nutation, with centrifugation for 30 min at 15,000 $\times$ *g* at 4°C to pellet precipitated α-syn. Further purification was achieved by anion exchange chromatography on a 5 mL HiTrap Q FF column (GE Healthcare, Little Chalfont, UK) where α-syn eluted at ~300 mM NaCl in 50 mM Tris-HCl pH 8. Finally, it was purified by size-exclusion chromatography (SEC) on a HiLoad 16/60 Superdex 75 column (GE Healthcare), equilibrated in 20 mM sodium phosphate, 50 mM NaCl, pH 7.4.

Membrane scaffold protein expression and purification

As reported in Bayburt et al. (51), *E. coli* BL21 (DE3) were transformed with MSP1D1 plasmid DNA in vector pET28a. Cells were grown in LB medium, induced by 1 mM IPTG at an optical density of 0.7 and incubated 5–6 h at 37°C, then pelleted down. Cells were resuspended in 50 mM Tris-HCl pH 8, 500 mM NaCl (buffer B) supplemented with 6 M Gdn-HCl and EDTA-free Complete protease inhibitors (Macherey-Nagel, Düren, Germany) lysed by sonication (Sonopuls MS72 probe; Bandelin, Berlin, Germany), centrifuged at 17,000 $\times$ *g* for 1 h (Cat. No. J2-21 rotor JA-20.1; Beckman Coulter, Brea, CA) and incubated 1 h with previously equilibrated 2.5 mL Ni-NTA agarose resin/3L culture (Macherey-Nagel). The column was washed

subsequently with 4 CV buffer B; 4 CV buffer B supplemented with 1% Triton X-100; 4 CV buffer B + 60 mM Na-cholate; and 4 CV buffer B, 4 CV buffer B + 20 mM imidazole. Four fractions of 1 CV were eluted with 250 mM imidazole. The whole process was kept at 4°C in a cold room. The elution fractions were pooled and dialyzed against 100-fold 200 mM Tris-HCl pH 7.5, 100 mM NaCl. N-terminal His-tag was cleaved using TEV protease incubated overnight at 4°C. ΔHis MSP was separated from MSP by immobilized metal ion affinity chromatography and concentrated to the desired molarity using a Vivaspin centrifugal device (Vivaproducts, Littleton, MA) of 10 kDa MWCO.

Nanodisc assembly

Nanodiscs (NDs) were assembled according to established protocols (52,53). In short, lipid chloroform stocks (Avanti Polar Lipids, Alabaster, AL) were dried under nitrogen flow to obtain a lipid film and stored under vacuum overnight. ΔHis MSP1D1 and the appropriate amount of 1-palmitoyl-2-oleoyl-*sn*-glycero-3-phospho-(1′-rac-glycerol) solubilized in 60 mM Na-cholate were mixed together in 20 mM Tris-HCl pH 7.5, 100 mM NaCl, 5 mM EDTA. The scaffold-to-lipids molar ratio was calculated from geometrical considerations. A quantity of 20% w/v of previously washed (methanol, water, buffer twice) Biobeads SM-2 (BioRad, Hercules, CA) was added and the mixture incubated at room temperature overnight. The Biobeads were removed by centrifugation and once again 20% w/v was added for an additional 4–5 h. Finally, they were purified by SEC on a HiLoad 16/600 Superdex 200 pg column (GE Healthcare) equilibrated with 20 mM sodium phosphate pH 7.4, 50 mM NaCl using an Äkta pure device (GE Healthcare) run at 1 mL/min. The quality of ND preparation was evaluated by the SEC chromatogram as well as by DLS (Nicomp system; Particle Sizing Systems, Port Richey, FL). NDs were concentrated to the desired molarity using a Vivaspin centrifugal device of 10 kDa MWCO.

DNP experiments

DNP experiments were conducted using a wide-bore Avance 600 MHz spectrometer (Bruker, Billerica, MA) connected to a 395-GHz gyrotron as a source of continuous microwaves. The samples were suspended in d_8-glycerol/D_2O/H_2O solutions (60:30:10 volume ratio) and 2.5 mM AMUPol (54) was added as a radical source. The samples were filled into 3.2-mm sapphire rotors and experiments were performed at a temperature of 100 K. All experiments were recorded using a recycle delay of 5 s. Two-dimensional (2D) ^{13}C-^{13}C proton-driven spin diffusion (PDSD) spectra with 1 s mixing time were recorded using 300 t_1 increments with 16 or 48 scans (16 scans for monomeric and fibrillated form, 48 scans for membrane-associated α-syn). All PDSD spectra were recorded at a magic angle spinning frequency of 9 kHz during a total experimental time of 8 h for the monomeric and fibrillar form and 24 h for α-syn in contact with a membrane. 2D ^{13}C-^{13}C double quantum/single quantum (DQ/SQ) SPC5 spectra were recorded at a magic angle spinning frequency of 8.2 kHz and with 64 or 128 scans (64 scans for monomeric and fibrillated form, 128 scans for all the α-syn in contact with membrane samples). The number of t_1 increments was 86 for the monomeric form and 128 for the others. The maximum evolution time was set to 1.3 ms for all samples. Total experimental times were 8, 11, and 24 h for monomeric, fibrillar, and membrane-bound α-syn, respectively. DNP enhancement factors of ∼32 were obtained for the protein signals in all samples (Fig. S1).

^1H decoupling using SPINAL-64 with a decoupling field of 104 kHz was employed during evolution and detection periods. All NMR spectra were processed with the software TopSpin 3.2 (Bruker).

To integrate the crosspeaks in DQ/SQ NMR spectra, one-dimensional projections from the respective regions were summed up. For the monomeric, fibrillary, and membrane-bound forms, the regions in between 85–103, 86–101, and 86–107 ppm on the double-quantum axis were summed up, respectively. The respective region is shown in Fig. S2). The program DMfit (dmfit2015_vs32) (55) was used for deconvolution of overlapping peaks with a Gaussian distribution. The integrals were calculated from the deconvoluted spectra. The crosspeak intensities were evaluated for both sides of the diagonal.

MD simulations

The replica exchange MD simulations were initialized from a linear conformation of the AGKTKEGVAGGA peptide, protected with N-terminal acetyl and C-terminal N-methyl amide capping groups. We performed simulations with five different force-field/solvent model combinations: 1) AMBER99SB*-ILDN (56,57) with implicit generalized Born solvent (58), 2) AMBER99SB*-ILDN with TIP3P explicit solvent (59), 3) AMBER99SB*-ILDN with TIP4P-D explicit solvent (60), 4) CHARMM22* (61) with TIP4P-Ew explicit solvent (62), and 5) CHARMM36m (63) with CHARMM-modified TIP3P explicit solvent (64). In addition, we performed an MD simulation of the GGVGG peptide with the CHARMM36m force field and CHARMM-modified TIP3P solvent (Fig. S3).The peptide was capped with an N-terminal acetyl and a C-terminal $–NH_2$ group.

The explicit solvent simulations were performed using GROMACS v. 4.6.7 (65) patched with PLUMED v. 2.1 (66,67). The peptide was centered in a cubic box, at least 10 Å away from each edge, and the net charge of the system was neutralized with one chloride ion. The system was simulated under periodic boundary conditions, where particle mesh Ewald (68) was used to treat electrostatic interactions. The short-range nonbonded interactions were calculated using a cutoff of 9 Å. Bond lengths were constrained with the LINCS algorithm (65). The system was minimized with the steepest descent and conjugate gradient minimizers, until the maximal force was smaller than 500 and 100 kJ mol^{-1} nm^{-1}, respectively. During the 0.1 ns NVT equilibration, the system was heated to 300 K using a v-rescale thermostat (69), and the main-chain atoms were restrained with a force of 1000 kJ mol^{-1} nm^{-2}. An additional 0.4-ns restrained NpT equilibration was performed keeping the pressure at 1 bar with a Berendsen barostat (70). The equilibrated system was used as starting structure for the subsequent Hamiltonian replica exchange-MD simulations involving eight replicas at 300 K and 1 bar. As before, a v-rescale thermostat was used together with Parrinello-Rahman barostat (71). An effective temperature range of 300–500 K was achieved by scaling the Hamiltonians of the replicas with λ-values of 1.000, 0.930, 0.864, 0.803, 0.747, 0.694, 0.645, and 0.600. Replica exchanges were attempted every 4 ps during the 1 μs simulation with a 2-fs time step (note: for AMBER99SB*-ILDN with TIP4P-D and CHARMM22* only 300 ns/replica were simulated), which led to exchange rates of 30–45%.

The implicit solvent simulation was performed with GROMACS v. 5.1.1, using the Still algorithm and a dielectric constant of 80 (57). Bond lengths were constrained with the LINCS algorithm and infinite cutoffs were used for the calculation of nonbonded interactions. The peptide was minimized with the steepest-descent minimizer (maximum force smaller than 250 kJ mol^{-1} nm^{-1}). Before the temperature replica exchange-MD simulation was started, each of the 12 replicas was equilibrated for 0.2 ns at the desired temperature ranging from 300 to 525 K. The exact temperatures were 300.0, 315.3, 331.5, 348.5, 366.5, 385.5, 405.5, 426.6, 448.8, 472.2, 496.8, and 522.4 K. The temperature was controlled with a v-rescale thermostat. Each replica was simulated for 2 μs (with a 2-fs time step), and the exchange between the replicas was attempted every 2 ps, which led to exchange rates of ∼58%.

The analysis was performed on the unperturbed replica ($\lambda = 1$ or $T =$ 300 K). The α_R-helix region was defined as $-100° < \phi < -30°$ and $-67° < \Psi < -7°$, α^+ as $-160° < \phi < -20°$ and $-120° < \Psi < 50°$, whereas the β-sheet was defined as $-180° < \phi < -90°$ and $50° < \Psi <$ 180° plus $-180° < \Psi < -120°$, the PP^{II} region covers $-90° < \phi < -20°$

and $50° < \Psi < 180°$ or $-180° < \Psi < -120°$, and the left-handed α-helix region is defined as $30° < \phi < 100°$ and $7° < \Psi < 67°$ (63). Chemical shifts were calculated with SPARTA+ (72) for conformations sampled every 10 ps of the trajectory. Data analysis was performed with the software MATLAB R2015b (The MathWorks, Natick, MA).

RESULTS AND DISCUSSION

Conformational ensemble of the IDP elucidated by DNP-enhanced solid-state NMR at cryogenic temperature

α-Syn is found predominantly as a disordered monomer in solution, with a very high conformational plasticity. Solution-state NMR spectra of monomeric α-syn yield random-coil chemical shift values that represent averages over the full conformational ensemble sampled by the protein (31); however, there is no corresponding random-coil conformation area in the Ramachandran plot. Instead, "random-coil state" refers to a rapid sampling of the energetically favored parts of the Ramachandran space that predominantly consists of conformations typically found in left- and right-handed α-helices and β-strand/polyproline-like conformations (Fig. 1 *c*) (73). Upon freezing the sample, each monomer is trapped in its conformation, and thus, every conformer gives rise to a chemical shift typical for its conformation, and, as a consequence, inhomogeneously broadened lines that contain information on the conformational distribution, are obtained. Fig. 1 *b* shows a DNP-enhanced 2D ^{13}C-^{13}C PDSD spectrum (1 s mixing-time) acquired on monomeric α-syn in glycerol/water solution at a temperature of ∼100 K. The 19 valine residues (shown in *red* in Fig. 1 *a*) of this IDP contribute to one inhomogeneously broadened Cα-Cβ crosspeak. Due to the labeling approach, no other intraresidual Cα-Cβ crosspeaks are expected. Note that due to the low resolution attained at cryogenic temperatures, discrimination between individual valine residues is not possible and site-specific information cannot be extracted from this spectrum. Instead, the crosspeak shows a characteristic and reproducible 2D shape reporting on the entire conformational ensemble adopted by the 19 valine residues in the α-syn sequence. Two peak maxima can be distinguished, one located in the typical α-helical chemical-shift region, and the other in the typical β-strand chemical-shift region. The static snapshot of the entire ensemble thus contains backbone conformations that are typical of α-helical and β-strand conformations. Note that we report here on the propensity of single residues to adopt conformations similar to those found in α-helices or β-strands and not on the secondary structures. We keep these denominations for the sake of simplicity.

It is visible in Fig. 1 *b* that the contribution from the β-strand part of the valine Cα-Cβ crosspeak is higher than the α-helical part. These data are in line with conformational propensities of α-syn derived from NMR and SAXS results, in which valine residues roughly sampled 70% β-sheet/polyproline and 30% α-helix conformation (74).

To gain further insight into this conformational sampling of valine residues inside disordered monomeric α-syn, we decided to pursue MD simulations. For the sake of computation time, we focused on the highly conserved KTKEGV motif of the α-syn primary sequence that repeats four times. The dodecapeptide AGKTKEGVAGGA contains a sole valine residue that was used to monitor the conformational changes. We performed long replica exchange MD simulations whose nature allows the molecule to cross energy barriers efficiently, and thus to thoroughly sample the conformational ensemble (75).

A structural ensemble generated with the AMBER99SB*-ILDN force field with TIP3P explicit solvent samples the full allowed region of the Ramachandran space (Figs. 1 *c* and S5). Chemical shifts were predicted from these structures with the help of the simulation program SPARTA+ (72). The comparison of the experimental and simulated chemical shifts shows good mutual agreement (Figs. 1 *d* and S5); however, simulated chemical shifts do not cover the full area of the experimental crosspeak. This observation may partly be explained either by the fact that 1) the single valine in the model peptide is not representative for all 19 valine residues in the sequence, or 2) that the conformational space sampled by the IDP exceeds that sampled by MD simulations, or 3) by shortcomings of the shift calculations. The coverage of the experimental crosspeaks becomes even smaller when using SHIFTX2 (76) instead of SPARTA+ for the chemical shift calculations. We also checked the influence of the force field and the water model on the sampled Ramachandran space and found that the relative ratio between α-helical and β-sheet-like conformations obtained from MD simulations strongly depends on both the force field and the water model (Fig. S6). The usage of TIP4P-D, a water model that was developed to produce more expanded protein structures for disordered states due to increased water dispersion interactions (60), shifts the equilibrium toward the β-state while not changing the sampled Ramachandran space otherwise, as the comparison between AMBER99SB*-ILDN/TIP3P and AMBER99SB*-ILDN/TIP4P-D shows (Fig. S6). The two CHARMM force fields disfavor the α-helical state and instead prefer the polyproline II conformation. Moreover, the left-handed helix is sampled at somewhat higher ψ-values than AMBER99SB*-ILDN predicts for this helix, which has already been observed in a previous study (77). Not quite unsurprisingly, AMBER99SB*-ILDN combined with an implicit solvent encourages intrapeptide hydrogen bonds, causing a gain in population of the α-helix.

We were further interested in probing the propensity of neighboring residues to adopt similar conformations. Notably, interresidual crosspeaks between ^{13}C atoms of adjacent amino acids can be observed in PDSD spectra acquired with a long mixing time (here 1 s). In the case of sparsely

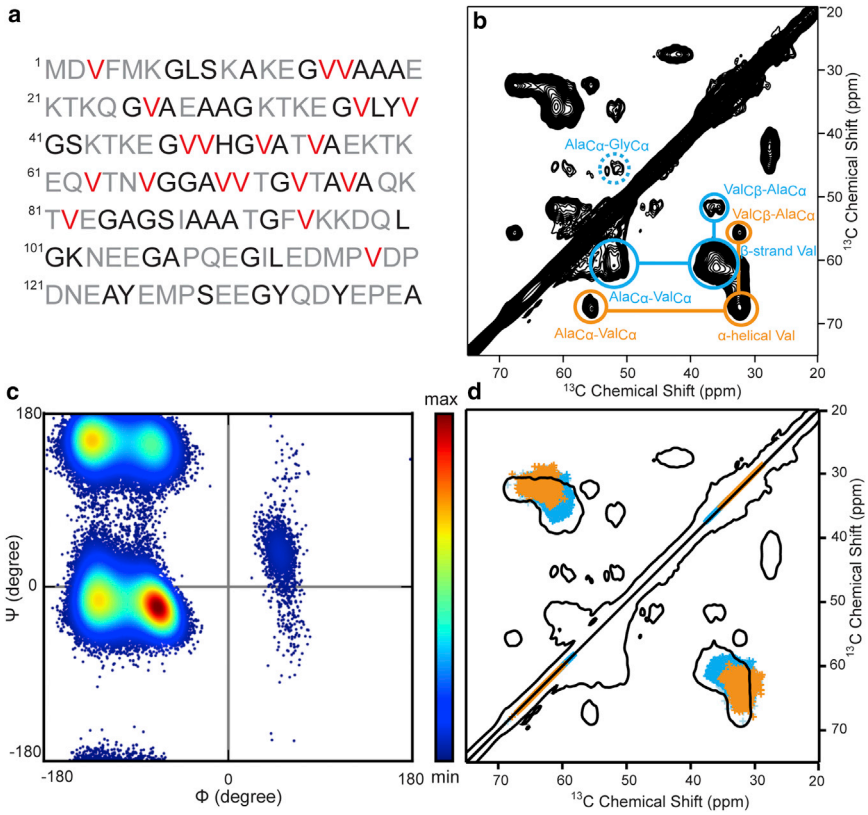

FIGURE 1 (*a*) Primary sequence of α-syn indicating the labeling scheme obtained by addition of [2-^{13}C]-glucose to the M9 medium: simultaneous ^{13}C enrichment of Cα and Cβ is only achieved for valine residues (*red*); amino acid residues labeled only in Cα position (except for leucine, which is labeled in Cβ and Cγ position) are printed in black. (*b*) 2D ^{13}C-^{13}C PDSD DNP-NMR spectrum of specifically ^{13}C-labeled α-syn monomers are shown. Intra- and interresidual crosspeaks involving β-strand or α-helical valine residues are highlighted in blue and orange, respectively. (*c* and *d*) Conformational sampling and NMR shifts of the valine residue in a representative AGKTKEGVAGGA peptide using the AMBER99SB*-ILDN force field in TIP3P explicit solvent are shown. (*c*) Ramachandran plot indicating relative probabilities of different secondary structures is shown. (*d*) NMR spectrum of monomeric α-syn in frozen solution (*black*) overlaid with chemical shifts of the simulated ensemble is shown. The positions of β-sheet (*blue*) and right-handed α-helix (*orange*) regions are also annotated. Further analysis is given in Fig. S4.

labeled α-syn, isotope-labeled neighbors of the valine residues are 7 ^{13}Cα-labeled alanine and 8 ^{13}Cα-labeled glycine residues. Interresidual valine-glycine cross-correlation signals were surprisingly weak, which may originate from the relatively large flexibility of glycine residues reflected by a larger array of backbone conformations and thus also increased heterogeneous line broadening of the glycine Cα resonance peak. On the other hand, two distinct interresidual valine-alanine crosspeaks can be found, located at chemical shifts typical for either α-helical or β-strand conformation for both amino acids. This indicates that neighboring valine and alanine residues have a strong propensity to adopt the same secondary structure in the majority of conformers and that a correlation between local conformations can be observed (Fig. S7). Previous ensemble descriptions of the Tau protein and of α-syn by NMR, SAXS, and molecular ensemble approaches are consistent with such a local structural correlation within a conformer, even though the ensemble selection treats each amino acid independently (74). Also, in our MD simulations, we could observe a weak but nonnegligible correlation between backbone conformations of neighboring amino acids. If the valine residue is found in a β-sheet-like conformation (definition given in the Materials and Methods), the subsequent alanine residue is found in a β-sheet-like conformation with a likelihood of 32%, whereas this likelihood is reduced to 24% when the preceding valine residue is in an α-helical conformation. Likewise, the alanine residue adopts an α-helical conformation with a likelihood of 24% if the preceding valine residue is in α-helical conformation, and only 11% if the preceding valine is in β-sheet conformation. Transient secondary structure elements have been observed and predicted in other IDPs as well (78–80).

Visualizing the conformational ensemble of α-syn in different states

α-Syn is able to spontaneously aggregate into amyloid fibrils, a species rich in β-sheet content (81). Misfolded and aggregated α-syn plays an important role in the neurodegenerative Parkinson's disease. We studied fibrillar α-syn under the same conditions as the monomeric α-syn to observe the conformational change due to fibrillation. As expected, the valine chemical shifts were shifted strongly toward the region typical of β-sheet conformation after fibrillation (Fig. 2 *a*). Nevertheless, a fraction of the valine signal remains in the α-helical region of the spectrum. As α-helical secondary structures per se are highly unexpected in amyloid fibrils, these are likely to stem from disordered regions protruding from the fibril core. It has indeed been reported before that the C-terminal region is mobile. Likewise, for most polymorphs, the β-sheet core region was found to start only around residue 38 (37–39,82), therefore, a substantial fraction of the valine residues can still be expected to be located in disordered regions of the protein.

α-Syn is also known to bind to lipid vesicles and membranes, with a binding mode strongly influenced by the

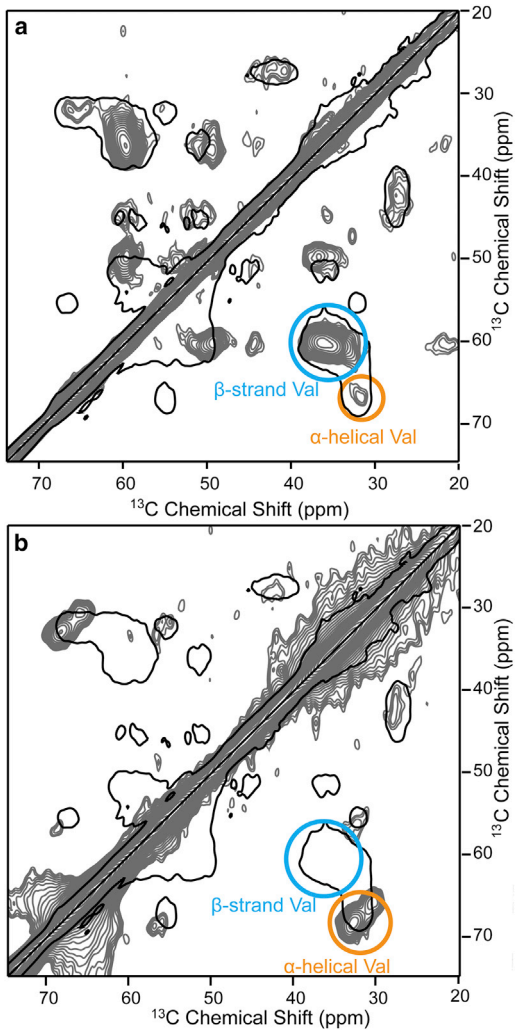

FIGURE 2 2D ^{13}C-^{13}C PDSD DNP-NMR spectra of specifically ^{13}C-labeled α-syn (*a*) fibrils and (*b*) α-syn monomers bound to nanodiscs in a molar ratio of 2:1 of protein to nanodisc. Intra- and interresidual crosspeaks involving β-strand or α-helical valine residues are highlighted in blue and orange, respectively. Both spectra were recorded with a longitudinal mixing time of 1 s. The outline (i.e., the lowest contour level) of the spectrum of monomeric α-syn (Fig. 1 *b*) is given in black for comparison. To see this figure in color, go online.

charge density of lipids and other physical properties (35). Moreover, α-syn undergoes a significant conformational transition with some regions of the protein adopting a high degree of α-helical structure (35,83,84). We therefore mixed α-syn with negatively charged lipid bilayers in the form of NDs (100% 1-palmitoyl-2-oleoyl-sn-glycero-3-phospho-(1′-rac-glycerol), more information in Materials and Methods) and characterized its conformational ensemble. In Fig. 2 *b*, the DNP-enhanced PDSD spectrum of α-syn bound to NDs in a protein-to-ND molar ratio of 2:1 is shown (one protein per membrane leaflet). We almost exclusively observe α-helical signals in this spectrum. The β-sheet content is dramatically decreased and could only be observed at the noise level.

Additionally, interresidual crosspeaks between α-helical valine and α-helical alanine are observed. This further confirms a correlation between local α-helical conformations of neighboring residues binding to the membrane bilayer and is in line with the α-helix structural model (35,85,86).

Notably, the α-helical crosspeak of membrane-bound α-syn (Fig. 2 *b*) has a distinct shape that exceeds the α-helical region covered by the random-coil ensemble. We observe two peak maxima in the α-helical signal region of the valine residues. This surprising fact could be attributed to two distinguishable populations of valine residues, e.g., those buried inside the lipid bilayer versus those residues facing more the charged headgroups, thus experiencing different chemical environments. Alternatively, it may also be feasible that α-syn can bind to the membrane surface in different ways, which also would lead to differences in the chemical environment of different valine residues.

Quantification of conformational populations in different states

PDSD or similar ^{13}C/^{13}C correlation spectra are considered as "protein fingerprints" in solid-state NMR. They are very useful, e.g., to visualize differences between samples, as we did above. Nevertheless, this type of experiment relies on a proton-proton dipolar network around the carbon nuclei to transfer magnetization. This has, in our hands, two disadvantages. The magnetization transfer is rather inefficient under DNP conditions, because the glycerol/water glassy matrix used contains only 10% protons to optimize enhancement factors. Thus, long mixing times are required during which relaxation processes can take place. Secondly, the relative intensities of crosspeaks are affected by different local densities of protons (e.g., at the protonated membrane and in the bulk solution), which may lead to variation in magnetization transfer efficiency and, thus, also in crosspeak intensity for amino acid residues located in different environments. For those reasons we decided to use a proton-independent magnetization transfer scheme for accurate quantification, i.e., the DQ/SQ experiment using SPC5 recoupling (87).

In the case of monomeric disordered α-syn, we do not expect those effects to play a significant role because all parts of the protein should experience the same proton density. Indeed, for both PDSD (Fig. 1 *b*) and DQ/SQ (Fig. 3 *a*), quantification of α-helical and β-strand contributions to the signal led to amounts of 30 and 70%, respectively, after deconvolution of the projected crosspeaks (Fig. 3 *e*). The discrepancy between the populations determined from the two experiments was <5%. These numbers are well in line with previously reported studies, as mentioned above.

For fibrillar α-syn, the quantification in the DQ/SQ spectrum (Fig. S2) gives a β-strand content of 89% and an α-helical content of 11%. Based on the intrinsic conformational propensity of disordered residues stated above

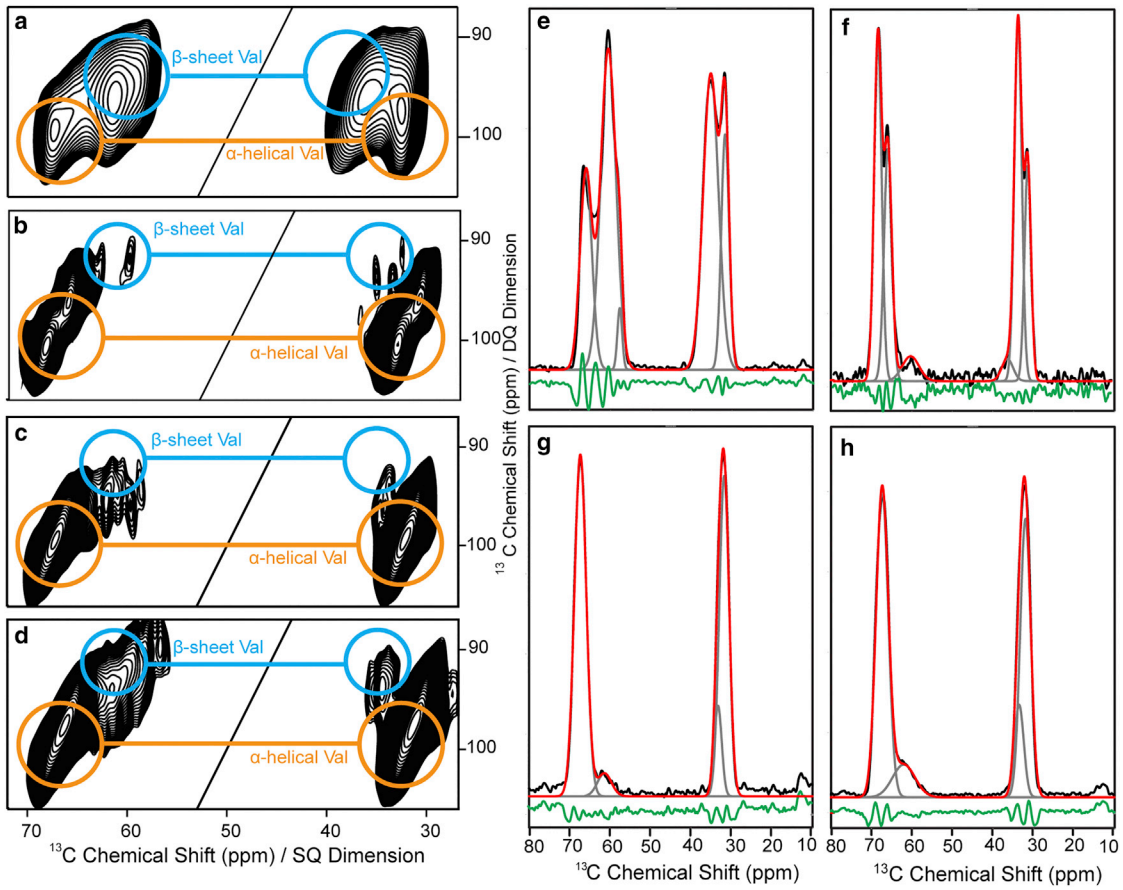

FIGURE 3 2D ^{13}C-^{13}C correlation DQ/SQ spectra of specifically ^{13}C-labeled (*a*) α-syn monomers, and α-syn monomers mixed with nanodiscs in (*b*) 2:1, (*c*) 8:1, and (*d*) 16:1 protein-to-nanodisc molar ratio. For one-dimensional projections (*black lines* in *e–h*), the Cα-Cβ crosspeak region of valines of the 2D spectra was summed up. The projections were deconvoluted using Gaussian line shapes with the help of the DMfit program. The projections are given in black, the single deconvoluted peaks in gray, the resulting fitting curve is shown in red for each sample, and the difference spectrum is given in green. The simulations were done for the monomeric form (*e*); for α-syn monomers mixed with nanodiscs in a protein-to-nanodisc molar ratio of (*f*) 2:1, (*g*) 8:1, and (*h*) 16:1; and for the fibrillar form (Fig. S2).

(i.e., assuming that 30% of all valine residues located in unstructured regions contribute to the α-helical signal intensity I_α), we can now quantify P_{rc}, the fraction of valine residues that remain disordered in the fibrillary state from I_α, as follows:

$$P_{rc} = \frac{I_\alpha}{0.3} = \frac{0.11}{0.3} = 0.36. \quad (1)$$

Thus, 36% of all 19 valines (corresponding to six to seven valine residues) in the α-syn sequence are expected to be disordered, which is very well in line with the six valines N-terminal of position 38 and one valine residue (V118) in the disordered C-terminus.

In the ND-bound state (one α-syn molecule per membrane leaflet), as the membrane is fully protonated, the fraction of α-syn bound to the membrane is in close vicinity to a dense proton network, which leads to a higher transfer efficiency in PDSD than for the unbound, unstructured part. Indeed, almost exclusively, the α-helical signal could be detected in PDSD spectra for membrane-bound α-syn, whereas β-sheet signals are hardly visible (Fig. 2 *b*). However, these signals can be observed in a DQ/SQ spectrum (Fig. 3 *b*), and after quantification (Fig. 3 *f*) give a β-strand to α-helix ratio of 6:94. The propensity of valine residues in unstructured regions of the protein can, in a similar way as in Eq. 1, be calculated as follows:

$$P_{rc} = \frac{I_\beta}{0.7}. \quad (2)$$

Therefore, the amount of valines remaining disordered is ~8%, corresponding to one or two valine residues in the sequence of α-syn. At such a low protein-to-lipid ratio and high lipid negative charge density, α-syn is expected to bind to the membrane with its N-terminal 92 residues (85,86), indeed leaving one valine residue in the disordered C-terminal region.

To challenge our quantitative approach further, we prepared samples of α-syn in different molar ratios with the

NDs: 8:1 and 16:1, corresponding to 4 and 8 proteins per membrane leaflet (composed of roughly 77 lipids), respectively. As visible in the DQ/SQ spectra shown in Fig. 3, *c* and *d*, increasing protein-to-ND ratios lead to higher signal intensities at chemical shifts typical for β-strands. The deconvolution (Fig. 3, *g* and *h*) gives β-strand contents of 11 and 21%, corresponding to fractions of disordered valines of 15 and 30%, respectively. This agrees well with the previously reported decrease in α-helical secondary structures when the lipid availability is lowered (88). Moreover, our previous solution NMR titration experiments on the same samples (89) allowed observing the behavior of α-syn association with NDs. The signal intensities from all unbound valine residues were summed up, and the ratios obtained this way are 7, 19, and 29% for protein-to-ND ratios of 2:1, 8:1, and 16:1, respectively. These numbers are in very good agreement (4% off for the highest discrepancy) with our DNP results, corroborating the ability of DNP-enhanced solid-state NMR to quantify conformational propensities and secondary structures with high accuracy.

CONCLUSIONS

The definition of representative conformational ensembles sampled by IDPs usually requires the combination of different methodologies. In this article, we have shown that it is possible to study conformational ensembles of IDPs with one experiment (and in 1 d) by DNP-enhanced ssNMR spectroscopy in frozen solution. Different conformational ensembles were obtained under different environmental conditions for our conformationally versatile model protein α-syn, and our results are in good agreement with previous studies.

DNP spectra were shown to faithfully report on expected conformational distribution of α-syn in different states of physiological relevance, i.e., unstructured free monomeric, β-sheet fibrillary, and α-helical membrane bound α-syn in different protein-to-lipid ratios, with very good agreement with the structural models.

Our analysis of 2D $^{13}C/^{13}C$ correlation spectra allowed accurate quantification of the expected structural features in different membrane binding modes of α-syn, which is also in line with our previously performed solution NMR titration experiments and current MD simulations.

In summary, we have demonstrated the power of DNP-enhanced solid-state NMR at cryogenic temperatures for the study of conformational ensembles and anticipate that this technique will also be useful for the study of interactions of proteins exhibiting flexible regions with other proteins, ligands, or membrane surfaces.

SUPPORTING MATERIAL

Seven figures are available at http://www.biophysj.org/biophysj/supplemental/S0006-3495(18)30214-5.

AUTHOR CONTRIBUTIONS

M.E., W.H., and H.H. designed the experiments. B.U., T.V., H.S., F.W., and A.G. performed experiments. B.U., T.V., and H.H. analyzed the NMR data. D.P. and B.S. performed and analyzed MD simulations. B.U. and H.H. wrote the manuscript with input from all authors. All authors discussed the results and commented on the manuscript.

ACKNOWLEDGMENTS

This work was supported by the Deutsche Forschungsgemeinschaft (HE 3243/4-1) and by the Ministry of Innovation, Science and Research within the framework of the NRW Strategieprojekt BioSC (BioSc seed fund). Financial support from an Emmy Noether grant of the DFG ET103/2-1 to M.E. is gratefully acknowledged. This project has further received funding from the European Research Council under the European Union's Horizon 2020 Research and Innovation Programme, grant agreement No. 726368 (to W.H.). T.V. acknowledges support from the International Graduate School of Protein Science and Technology (iGRASPseed) granted by the Ministry of Innovation, Science and Research of the state North Rhine-Westphalia. D.P. is financially supported by the Jürgen Manchot Foundation. The authors gratefully acknowledge the computing time granted by the JARA-HPC Vergabegremium and VSR commission on the supercomputer JURECA (project ICS69) at Forschungszentrum Jülich as well as access to the Jülich-Düsseldorf Biomolecular NMR Center.

REFERENCES

1. Fink, A. L. 2005. Natively unfolded proteins. *Curr. Opin. Struct. Biol.* 15:35–41.
2. Wright, P. E., and H. J. Dyson. 1999. Intrinsically unstructured proteins: re-assessing the protein structure-function paradigm. *J. Mol. Biol.* 293:321–331.
3. Donne, D. G., J. H. Viles, …, H. J. Dyson. 1997. Structure of the recombinant full-length hamster prion protein PrP(29–231): the N terminus is highly flexible. *Proc. Natl. Acad. Sci. USA.* 94:13452–13457.
4. Dyson, H. J., and P. E. Wright. 2005. Intrinsically unstructured proteins and their functions. *Nat. Rev. Mol. Cell Biol.* 6:197–208.
5. van der Lee, R., M. Buljan, …, M. M. Babu. 2014. Classification of intrinsically disordered regions and proteins. *Chem. Rev.* 114:6589–6631.
6. Fu, B., and M. Vendruscolo. 2015. Structure and dynamics of intrinsically disordered proteins. *In* Intrinsically Disordered Proteins Studied by NMR Spectroscopy. I. C. Felli and R. Pierattelli, eds. Springer, New York, NY, pp. 35–48.
7. Eschmann, N. A., E. R. Georgieva, …, S. Han. 2017. Signature of an aggregation-prone conformation of tau. *Sci. Rep.* 7:44739.
8. Kjaergaard, M., A.-B. Nørholm, …, B. B. Kragelund. 2010. Temperature-dependent structural changes in intrinsically disordered proteins: formation of α-helices or loss of polyproline II? *Protein Sci.* 19:1555–1564.
9. Rauscher, S., V. Gapsys, …, H. Grubmüller. 2015. Structural ensembles of intrinsically disordered proteins depend strongly on force field: a comparison to experiment. *J. Chem. Theory Comput.* 11:5513–5524.
10. Receveur-Bréchot, V., J.-M. Bourhis, …, S. Longhi. 2006. Assessing protein disorder and induced folding. *Proteins.* 62:24–45.
11. Haas, E. 2012. Ensemble FRET methods in studies of intrinsically disordered proteins. *In* Intrinsically Disordered Protein Analysis: Volume 1, Methods and Experimental Tools. V. N. Uversky and A. K. Dunker, eds. Humana Press, New York, NY, pp. 467–498.
12. Beauchamp, K. A., Y.-S. Lin, …, V. S. Pande. 2012. Are protein force fields getting better? A systematic benchmark on 524 diverse NMR measurements. *J. Chem. Theory Comput.* 8:1409–1414.

13. Abraham, M. J., T. Murtola, …, E. Lindahl. 2015. GROMACS: high performance molecular simulations through multi-level parallelism from laptops to supercomputers. *SoftwareX*. 1–2:19–25.
14. Shaw, D. E., M. M. Deneroff, …, S. C. Wang. 2008. Anton, a special-purpose machine for molecular dynamics simulation. *Commun. ACM*. 51:91–97.
15. Choy, W.-Y., and J. D. Forman-Kay. 2001. Calculation of ensembles of structures representing the unfolded state of an SH3 domain. *J. Mol. Biol.* 308:1011–1032.
16. Bernadó, P., L. Blanchard, …, M. Blackledge. 2005. A structural model for unfolded proteins from residual dipolar couplings and small-angle x-ray scattering. *Proc. Natl. Acad. Sci. USA*. 102:17002–17007.
17. Shen, Y., and A. Bax. 2007. Protein backbone chemical shifts predicted from searching a database for torsion angle and sequence homology. *J. Biomol. NMR*. 38:289–302.
18. Ozenne, V., R. Schneider, …, M. Blackledge. 2012. Mapping the potential energy landscape of intrinsically disordered proteins at amino acid resolution. *J. Am. Chem. Soc.* 134:15138–15148.
19. Nodet, G., L. Salmon, …, M. Blackledge. 2009. Quantitative description of backbone conformational sampling of unfolded proteins at amino acid resolution from NMR residual dipolar couplings. *J. Am. Chem. Soc.* 131:17908–17918.
20. Krzeminski, M., J. A. Marsh, …, J. D. Forman-Kay. 2013. Characterization of disordered proteins with ENSEMBLE. *Bioinformatics*. 29:398–399.
21. Daughdrill, G. W., S. Kashtanov, …, F. M. Ytreberg. 2012. Understanding the structural ensembles of a highly extended disordered protein. *Mol. Biosyst.* 8:308–319.
22. Kurzbach, D., G. Kontaxis, …, R. Konrat. 2015. NMR spectroscopic studies of the conformational ensembles of intrinsically disordered proteins. *Adv. Exp. Med. Biol.* 870:149–185.
23. Cavalli, A., C. Camilloni, and M. Vendruscolo. 2013. Molecular dynamics simulations with replica-averaged structural restraints generate structural ensembles according to the maximum entropy principle. *J. Chem. Phys.* 138:094112.
24. Parigi, G., N. Rezaei-Ghaleh, …, C. Luchinat. 2014. Long-range correlated dynamics in intrinsically disordered proteins. *J. Am. Chem. Soc.* 136:16201–16209.
25. Concistrè, M., E. Carignani, …, M. H. Levitt. 2014. Freezing of molecular motions probed by cryogenic magic angle spinning NMR. *J. Phys. Chem. Lett.* 5:512–516.
26. Heise, H., S. Luca, …, M. Baldus. 2005. Probing conformational disorder in neurotensin by two-dimensional solid-state NMR and comparison to molecular dynamics simulations. *Biophys. J.* 89:2113–2120.
27. Havlin, R. H., and R. Tycko. 2005. Probing site-specific conformational distributions in protein folding with solid-state NMR. *Proc. Natl. Acad. Sci. USA*. 102:3284–3289.
28. Siemer, A. B., K. Y. Huang, and A. E. McDermott. 2012. Protein linewidth and solvent dynamics in frozen solution NMR. *PLoS One*. 7:e47242.
29. Tycko, R. 2013. NMR at low and ultralow temperatures. *Acc. Chem. Res.* 46:1923–1932.
30. Uversky, V. N. 2003. A protein-chameleon: conformational plasticity of alpha-synuclein, a disordered protein involved in neurodegenerative disorders. *J. Biomol. Struct. Dyn.* 21:211–234.
31. Eliezer, D., E. Kutluay, …, G. Browne. 2001. Conformational properties of alpha-synuclein in its free and lipid-associated states. *J. Mol. Biol.* 307:1061–1073.
32. Bellani, S., V. L. Sousa, …, E. Chieregatti. 2010. The regulation of synaptic function by α-synuclein. *Commun. Integr. Biol.* 3:106–109.
33. Burré, J., M. Sharma, …, T. C. Südhof. 2010. Alpha-synuclein promotes SNARE-complex assembly in vivo and in vitro. *Science*. 329:1663–1667.
34. Diao, J., J. Burré, …, A. T. Brunger. 2013. Native α-synuclein induces clustering of synaptic-vesicle mimics via binding to phospholipids and synaptobrevin-2/VAMP2. *eLife*. 2:e00592.
35. Fusco, G., A. De Simone, …, G. Veglia. 2014. Direct observation of the three regions in α-synuclein that determine its membrane-bound behaviour. *Nat. Commun.* 5:3827.
36. Chiti, F., and C. M. Dobson. 2006. Protein misfolding, functional amyloid, and human disease. *Annu. Rev. Biochem.* 75:333–366.
37. Heise, H., W. Hoyer, …, M. Baldus. 2005. Molecular-level secondary structure, polymorphism, and dynamics of full-length alpha-synuclein fibrils studied by solid-state NMR. *Proc. Natl. Acad. Sci. USA*. 102:15871–15876.
38. Bousset, L., L. Pieri, …, R. Melki. 2013. Structural and functional characterization of two alpha-synuclein strains. *Nat. Commun.* 4:2575.
39. Tuttle, M. D., G. Comellas, …, C. M. Rienstra. 2016. Solid-state NMR structure of a pathogenic fibril of full-length human α-synuclein. *Nat. Struct. Mol. Biol.* 23:409–415.
40. Hoyer, W., H. Shaykhalishahi, …, H. Heise. 2015. Structural characterization of α-synuclein amyloids. *In* The Prion Phenomena in Neurodegenerative Diseases: New Frontiers in Neuroscience. Nova Science Biomedical, Hauppauge, NY, pp. 111–128.
41. Goedert, M. 2001. Alpha-synuclein and neurodegenerative diseases. *Nat. Rev. Neurosci.* 2:492–501.
42. Drescher, M., M. Huber, and V. Subramaniam. 2012. Hunting the chameleon: structural conformations of the intrinsically disordered protein alpha-synuclein. *ChemBioChem.* 13:761–768.
43. Bertoncini, C. W., Y. S. Jung, …, M. Zweckstetter. 2005. Release of long-range tertiary interactions potentiates aggregation of natively unstructured alpha-synuclein. *Proc. Natl. Acad. Sci. USA*. 102:1430–1435.
44. Kim, H.-Y., H. Heise, …, M. Zweckstetter. 2007. Correlation of amyloid fibril β-structure with the unfolded state of α-synuclein. *ChemBioChem.* 8:1671–1674.
45. Carver, T. R., and C. P. Slichter. 1953. Polarization of nuclear spins in metals. *Phys. Rev.* 92:212–213.
46. Overhauser, A. W. 1953. Polarization of nuclei in metals. *Phys. Rev.* 92:411–415.
47. Akbey, Ü., W. T. Franks, …, H. Oschkinat. 2010. Dynamic nuclear polarization of deuterated proteins. *Angew. Chem. Int. Ed. Engl.* 49:7803–7806.
48. Rosay, M., L. Tometich, …, W. E. Maas. 2010. Solid-state dynamic nuclear polarization at 263 GHz: spectrometer design and experimental results. *Phys. Chem. Chem. Phys.* 12:5850–5860.
49. Hong, M., and K. Jakes. 1999. Selective and extensive ^{13}C labeling of a membrane protein for solid-state NMR investigations. *J. Biomol. NMR*. 14:71–74.
50. Hoyer, W., D. Cherny, …, T. M. Jovin. 2004. Impact of the acidic C-terminal region comprising amino acids 109–140 on alpha-synuclein aggregation in vitro. *Biochemistry*. 43:16233–16242.
51. Bayburt, T. H., J. W. Carlson, and S. G. Sligar. 1998. Reconstitution and imaging of a membrane protein in a nanometer-size phospholipid bilayer. *J. Struct. Biol.* 123:37–44.
52. Denisov, I. G., Y. V. Grinkova, …, S. G. Sligar. 2004. Directed self-assembly of monodisperse phospholipid bilayer nanodiscs with controlled size. *J. Am. Chem. Soc.* 126:3477–3487.
53. Viegas, A., T. Viennet, and M. Etzkorn. 2016. The power, pitfalls and potential of the nanodisc system for NMR-based studies. *Biol. Chem.* 397:1335–1354.
54. Sauvée, C., M. Rosay, …, P. Tordo. 2013. Highly efficient, water-soluble polarizing agents for dynamic nuclear polarization at high frequency. *Angew. Chem. Int. Ed. Engl.* 52:10858–10861.
55. Massiot, D., F. Fayon, …, G. Hoatson. 2002. Modelling one- and two-dimensional solid-state NMR spectra. *Magn. Reson. Chem.* 40:70–76.
56. Best, R. B., and G. Hummer. 2009. Optimized molecular dynamics force fields applied to the helix-coil transition of polypeptides. *J. Phys. Chem. B*. 113:9004–9015.

57. Lindorff-Larsen, K., S. Piana, …, D. E. Shaw. 2010. Improved side-chain torsion potentials for the Amber ff99SB protein force field. *Proteins.* 78:1950–1958.

58. Qiu, D., P. S. Shenkin, …, W. C. Still. 1997. The GB/SA continuum model for solvation. A fast analytical method for the calculation of approximate Born radii. *J. Phys. Chem. A.* 101:3005–3014.

59. Jorgensen, W. L., J. Chandrasekhar, …, M. L. Klein. 1983. Comparison of simple potential functions for simulating liquid water. *J. Chem. Phys.* 79:926–935.

60. Piana, S., A. G. Donchev, …, D. E. Shaw. 2015. Water dispersion interactions strongly influence simulated structural properties of disordered protein states. *J. Phys. Chem. B.* 119:5113–5123.

61. Piana, S., K. Lindorff-Larsen, and D. E. Shaw. 2011. How robust are protein folding simulations with respect to force field parameterization? *Biophys. J.* 100:L47–L49.

62. Horn, H. W., W. C. Swope, …, T. Head-Gordon. 2004. Development of an improved four-site water model for biomolecular simulations: TIP4P-Ew. *J. Chem. Phys.* 120:9665–9678.

63. Huang, J., S. Rauscher, …, A. D. MacKerell, Jr. 2017. CHARMM36m: an improved force field for folded and intrinsically disordered proteins. *Nat. Methods.* 14:71–73.

64. MacKerell, A. D., D. Bashford, …, M. Karplus. 1998. All-atom empirical potential for molecular modeling and dynamics studies of proteins. *J. Phys. Chem. B.* 102:3586–3616.

65. Hess, B. 2008. P-LINCS: a parallel linear constraint solver for molecular simulation. *J. Chem. Theory Comput.* 4:116–122.

66. Tribello, G. A., M. Bonomi, …, G. Bussi. 2014. PLUMED 2: new feathers for an old bird. *Comput. Phys. Commun.* 185:604–613.

67. Bussi, G. 2014. Hamiltonian replica exchange in GROMACS: a flexible implementation. *Mol. Phys.* 112:379–384.

68. York, D. M., T. A. Darden, and L. G. Pedersen. 1993. The effect of long-range electrostatic interactions in simulations of macromolecular crystals—a comparison of the Ewald and truncated list methods. *J. Chem. Phys.* 99:8345–8348.

69. Bussi, G., D. Donadio, and M. Parrinello. 2007. Canonical sampling through velocity rescaling. *J. Chem. Phys.* 126:014101.

70. Berendsen, H. J. C., J. P. M. Postma, …, J. R. Haak. 1984. Molecular-dynamics with coupling to an external bath. *J. Chem. Phys.* 81:3684–3690.

71. Parrinello, M., and A. Rahman. 1981. Polymorphic transitions in single-crystals—a new molecular-dynamics method. *J. Appl. Phys.* 52:7182–7190.

72. Shen, Y., and A. Bax. 2010. SPARTA+: a modest improvement in empirical NMR chemical shift prediction by means of an artificial neural network. *J. Biomol. NMR.* 48:13–22.

73. Smith, L. J., K. M. Fiebig, …, C. M. Dobson. 1996. The concept of a random coil. Residual structure in peptides and denatured proteins. *Fold. Des.* 1:R95–R106.

74. Schwalbe, M., V. Ozenne, …, M. Blackledge. 2014. Predictive atomic resolution descriptions of intrinsically disordered hτ40 and α-synuclein in solution from NMR and small angle scattering. *Structure.* 22:238–249.

75. Schor, M., A. S. J. S. Mey, and C. E. MacPhee. 2016. Analytical methods for structural ensembles and dynamics of intrinsically disordered proteins. *Biophys. Rev.* 8:429–439.

76. Han, B., Y. Liu, …, D. S. Wishart. 2011. SHIFTX2: significantly improved protein chemical shift prediction. *J. Biomol. NMR.* 50:43–57.

77. Best, R. B., X. Zhu, …, A. D. MacKerell, Jr. 2012. Optimization of the additive CHARMM all-atom protein force field targeting improved sampling of the backbone φ, ψ and side-chain $\chi(1)$ and $\chi(2)$ dihedral angles. *J. Chem. Theory Comput.* 8:3257–3273.

78. Szöllősi, D., T. Horváth, …, T. Hegedűs. 2014. Discrete molecular dynamics can predict helical prestructured motifs in disordered proteins. *PLoS One.* 9:e95795.

79. Ytreberg, F. M., W. Borcherds, …, G. W. Daughdrill. 2015. Using chemical shifts to generate structural ensembles for intrinsically disordered proteins with converged distributions of secondary structure. *Intrinsically Disord. Proteins.* 3:e984565.

80. Kurzbach, D., A. Vanas, …, R. Konrat. 2016. Detection of correlated conformational fluctuations in intrinsically disordered proteins through paramagnetic relaxation interference. *Phys. Chem. Chem. Phys.* 18:5753–5758.

81. Spillantini, M. G., M. L. Schmidt, …, M. Goedert. 1997. Alpha-synuclein in Lewy bodies. *Nature.* 388:839–840.

82. Vilar, M., H. T. Chou, …, R. Riek. 2008. The fold of alpha-synuclein fibrils. *Proc. Natl. Acad. Sci. USA.* 105:8637–8642.

83. Maltsev, A. S., J. Ying, and A. Bax. 2012. Impact of N-terminal acetylation of α-synuclein on its random coil and lipid binding properties. *Biochemistry.* 51:5004–5013.

84. Fusco, G., A. De Simone, …, C. M. Dobson. 2016. Structural ensembles of membrane-bound α-synuclein reveal the molecular determinants of synaptic vesicle affinity. *Sci. Rep.* 6:27125.

85. Drescher, M., F. Godschalk, …, M. Huber. 2008. Spin-label EPR on alpha-synuclein reveals differences in the membrane binding affinity of the two antiparallel helices. *ChemBioChem.* 9:2411–2416.

86. Ulmer, T. S., A. Bax, …, R. L. Nussbaum. 2005. Structure and dynamics of micelle-bound human α-synuclein. *J. Biol. Chem.* 280:9595–9603.

87. Hohwy, M., C. M. Rienstra, …, R. G. Griffin. 1999. Fivefold symmetric homonuclear dipolar recoupling in rotating solids: application to double quantum spectroscopy. *J. Chem. Phys.* 110:7983–7992.

88. Galvagnion, C., A. K. Buell, …, C. M. Dobson. 2015. Lipid vesicles trigger α-synuclein aggregation by stimulating primary nucleation. *Nat. Chem. Biol.* 11:229–234.

89. Viennet, T., M. M. Wördehoff, …, M. Etzkorn. 2018. A structural and kinetic link between membrane association and amyloid fibril formation of α-synuclein. bioRxiv, https://doi.org/10.1101/173724.

Biophysical Journal, Volume *114*

Supplemental Information

DNP-Enhanced MAS NMR: A Tool to Snapshot Conformational Ensembles of α-Synuclein in Different States

Boran Uluca, Thibault Viennet, Dušan Petrović, Hamed Shaykhalishahi, Franziska Weirich, Ayşenur Gönülalan, Birgit Strodel, Manuel Etzkorn, Wolfgang Hoyer, and Henrike Heise

Supporting Material

DNP-enhanced MAS NMR: a Tool to Snapshot Conformational Ensembles of α-Synuclein in Different States

Boran Uluca[1,2], Thibault Viennet[1,2], Dušan Petrović[1], Hamed Shaykhalishahi[1,2], Franziska Weirich[1,2], Ayşenur Gönülalan[1], Birgit Strodel[1,3], Manuel Etzkorn[1,2], Wolfgang Hoyer[1,2], Henrike Heise[*,1,2]

[1]Institute of Complex Systems, Structural Biochemistry (ICS-6), Research Center Jülich, 52425 Jülich, Germany

[2]Institute of Physical Biology, Heinrich-Heine-University Düsseldorf, Universitätsstraße 1, 40225 Düsseldorf, Germany

[3]Institute of Theoretical and Computational Chemistry, Heinrich-Heine-University Düsseldorf, Universitätsstraße 1, 40225 Düsseldorf, Germany

*corresponding author: h.heise@fz-juelich.de

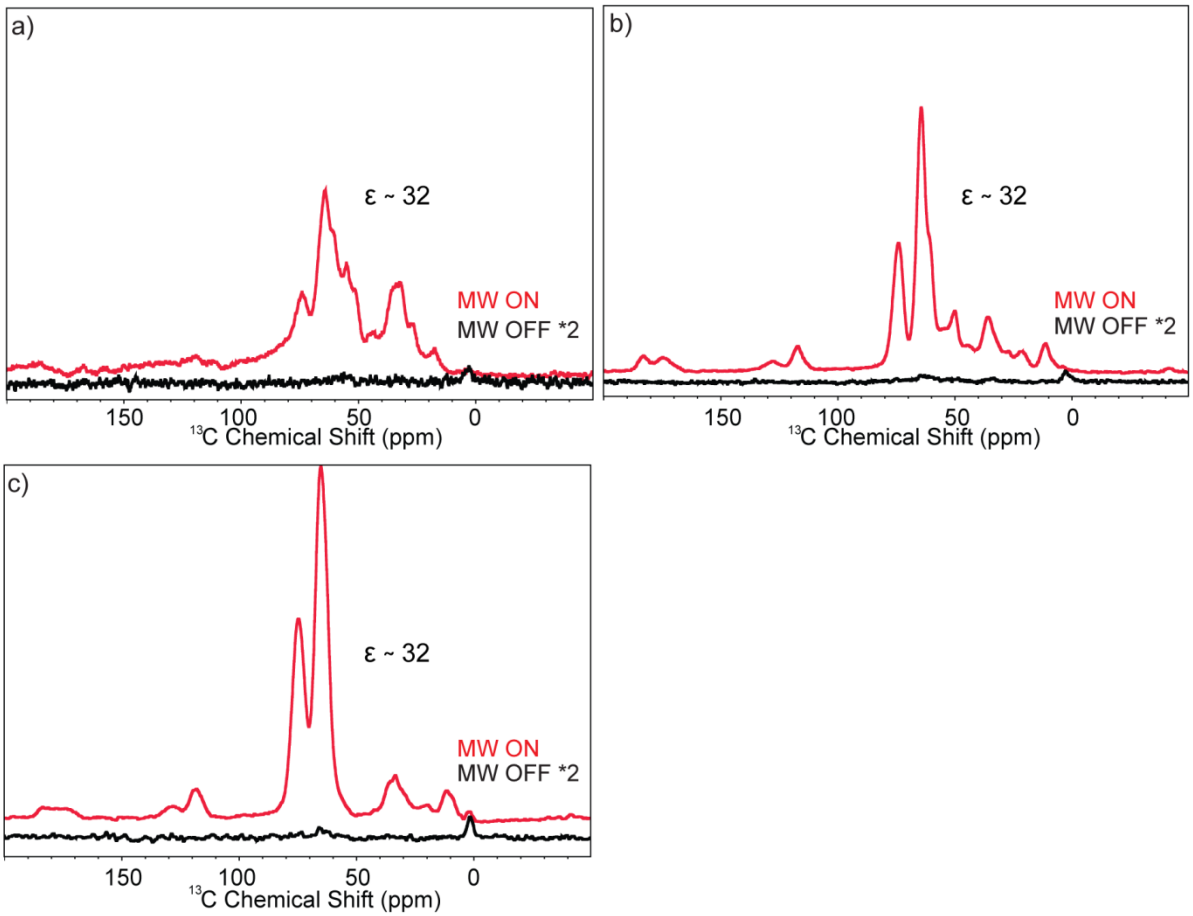

Figure S1: To determine the DNP enhancement factor, ^{13}C CP-MAS spectra were recorded with microwave irradiation (red) and compared to spectra recorded without microwave irradiation (black) under exactly the same experimental conditions. Enhancement factors of ~32 were obtained for the aliphatic region of the protein in all cases, i.e. for a) monomeric, b) fibrillary and c) α-syn monomers mixed with nanodiscs in a 2:1 protein to nanodisc molar ratio. All spectra were recorded at a nominal sample temperature of ~ 100 K, with a spinning speed of 8 kHz and 16 scans. Contact times for proton to carbon transfer via cross polarization were a) 100 µs, b) 400 µs, and c) 1150 µs.

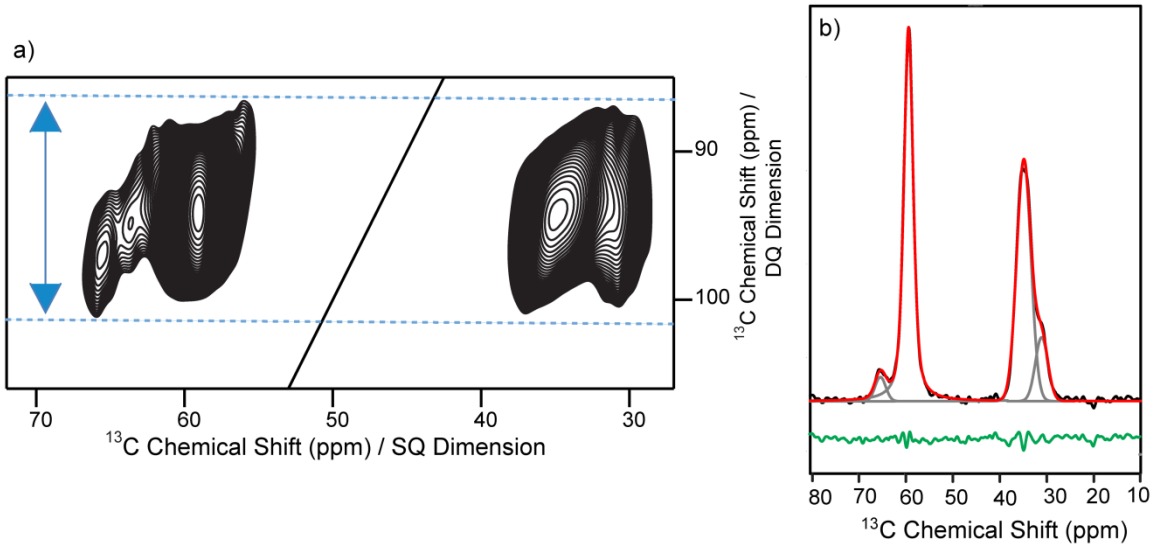

Figure S2: a) 2D ^{13}C-^{13}C correlation DQ/SQ spectrum of specifically ^{13}C labeled α-syn fibrils. 1D projections of 2D spectra were generated by summing up the Cα-Cβ cross-peak region for valines, which is indicated here by the blue dashed lines. b) The projections were deconvoluted using Gaussian line shapes with the help of the DMfit software. The projection is given in black and the single deconvoluted peaks in grey, the resulting fitting curve is shown in red, and the difference spectrum is given in green.

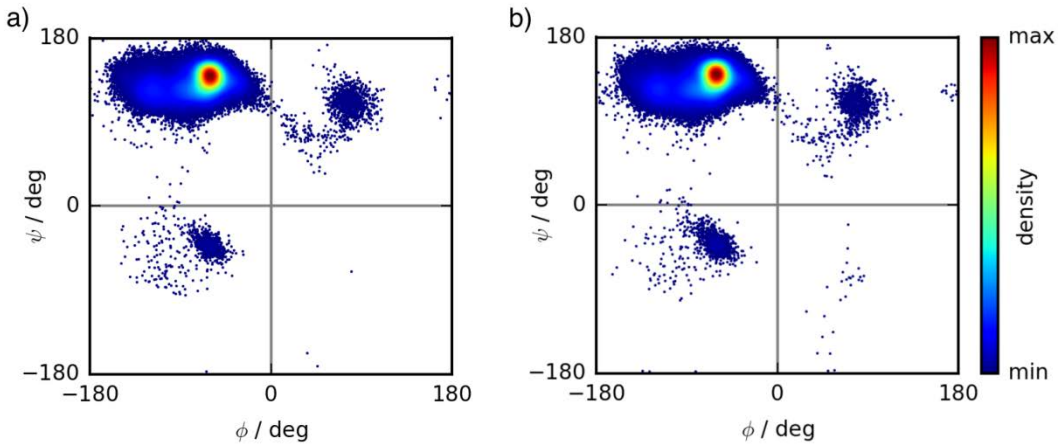

Figure S3: Ramachandran plots for the valine residue in the model peptides a) AGKTKEGVAGGA and b) GGVGG simulated with the CHARMM36m force field using the CHARMM modified TIP3P water model. The color bar shows the local data density.

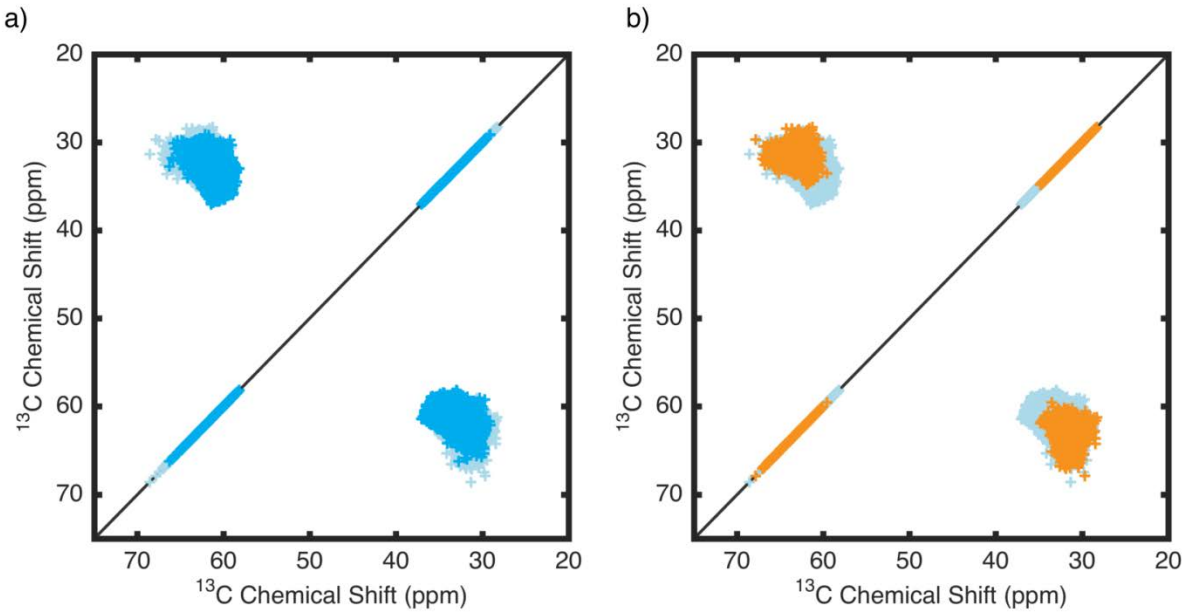

Figure S4: Conformational sampling and NMR shifts of the valine residue in the AGKTKEGVAGGA peptide from a MD simulation using the AMBER99SB*-ILDN force field in TIP3P explicit solvent. Chemical shifts of the full simulated ensemble are shown in light blue. The positions of specific regions are given as: a) β-sheet in blue, b) right handed α-helix in orange. A β-sheet like conformation is defined in the Ramachandran space as $-180° < \phi < -90°$ and $-180° < \psi < -120°$ or $50° < \psi < 180°$, and left handed α-helical conformation as $-100° < \phi < -30°$ and $-67° < \psi < -7°$.

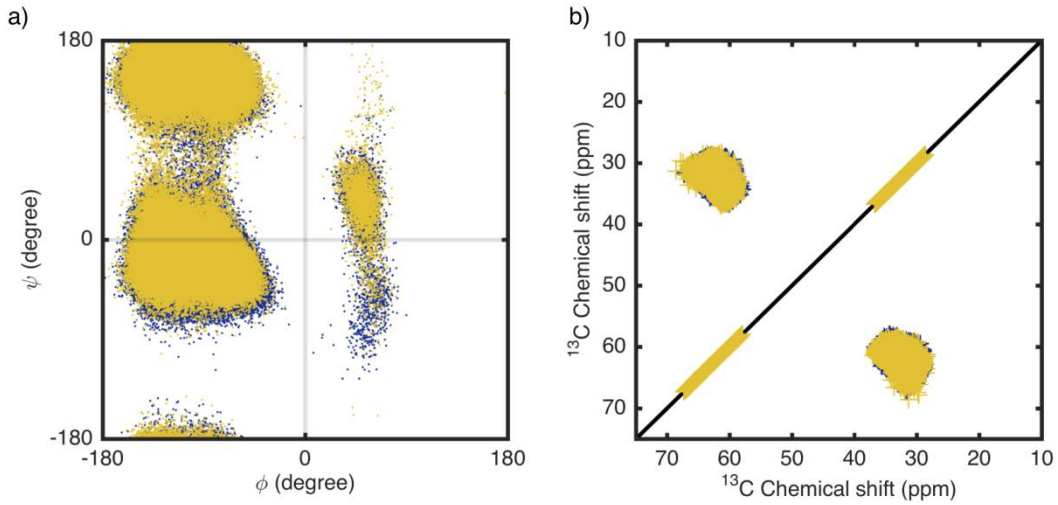

Figure S5: AMBER99SB*-ILDN force field used with generalized Born implicit solvent (blue) and TIP3P explicit solvent (orange) show great mutual resemblance in a) sampled conformational space and b) ^{13}C chemical shifts of the valine residue in the AGKTKEGVAGGA peptide. Figure S6 shows, however, that the relative ratio of the secondary structures is strongly dependent on the type of solvent used for MD simulations.

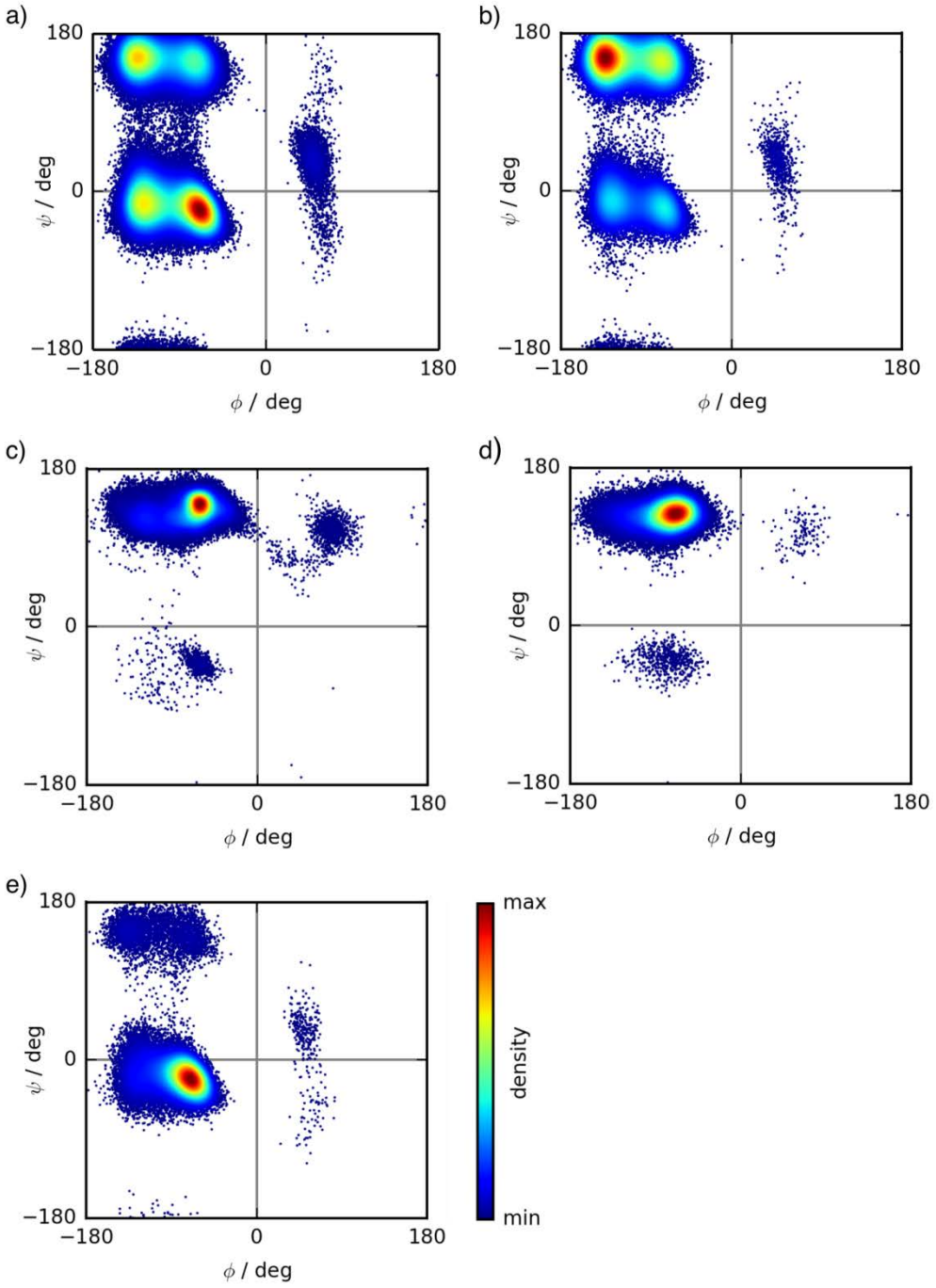

Figure S6: Force field comparison for conformational sampling of the valine residue in the AGKTKEGVAGGA peptide. The Ramachandran plots with data distribution are shown for a) AMBER99SB*-ILDN force field with TIP3P explicit solvent, b) AMBER99SB*-ILDN force field with TIP4P-D explicit solvent, c) CHARMM36m force field with CHARMM modified TIP3P solvent, d) CHARMM22* force field with TIP4P-Ew water, and e) AMBER99SB*-ILDN with implicit generalized Born solvent. The CMAP potential in the CHARMM simulations was not scaled. The color bar shows the local data density.

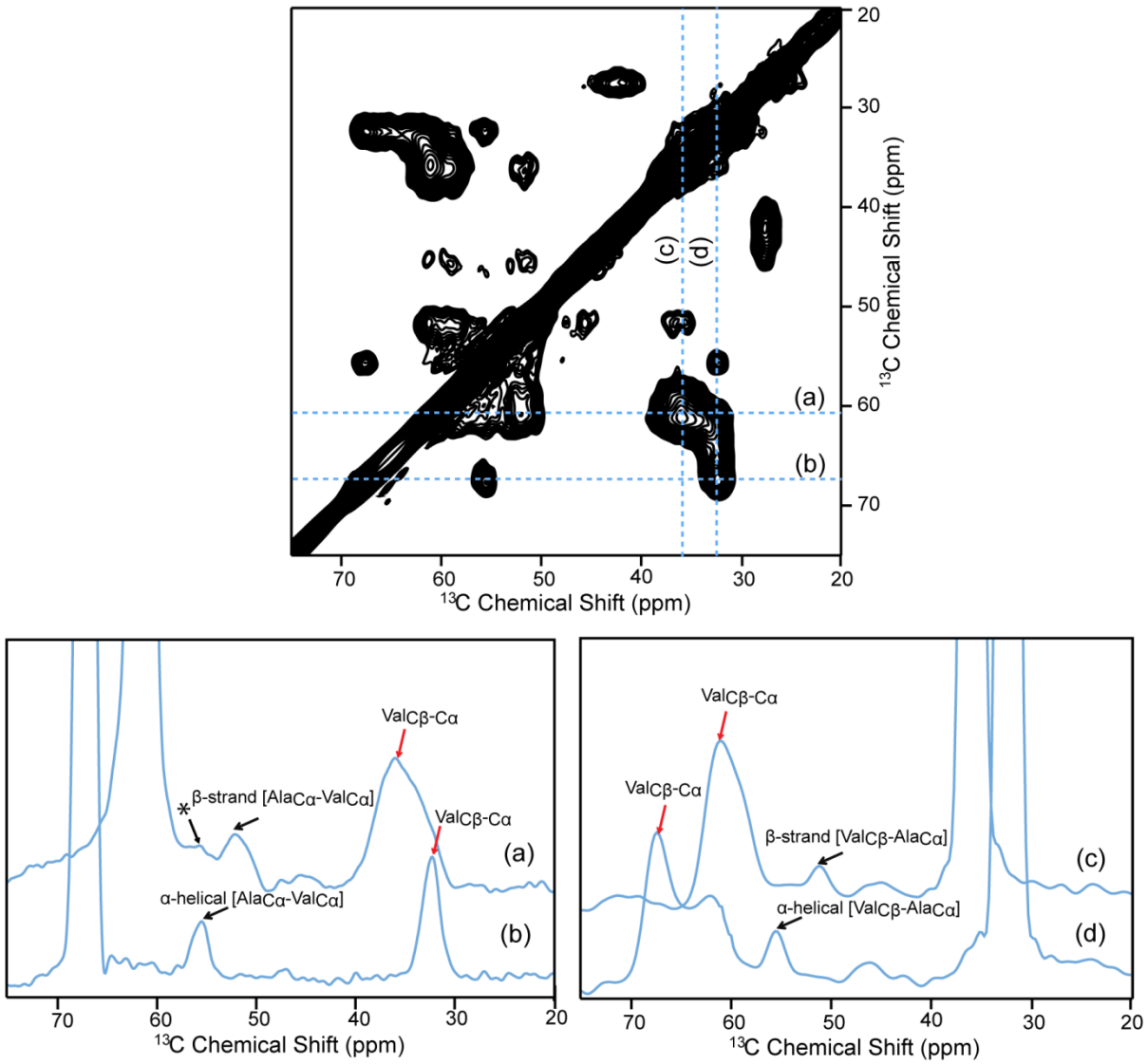

Figure S7: 2D ^{13}C-^{13}C PDSD DNP-NMR spectra of specifically ^{13}C labeled α-syn monomers recorded with a longitudinal mixing time of 1 s. From the 2D spectra, 1D slices were extracted for four cross sections at the positions labeled with (a), (b), (c) and (d). The black arrows indicate inter-residual valine-alanine correlations adopting the same secondary structure, and red arrows indicate intra-residual Cα-Cβ correlations of valines. A correlation of different local structural motifs, i.e., of β-strand Val(Cα) and α-helical Ala(Cα) might be contained in the peak marked with an asterisk. However, this peak is very close to the diagonal and therefore it is not possible to assess if it is a peak or a baseline distortion. Furthermore, there is no symmetry peak observed on the other side of the diagonal. Therefore, we conclude that there is no such correlation of neighboring α-helical and β-strand secondary structure motifs.

Molecular basis for diversification of yeast prion strain conformation

Yumiko Ohhashi[a,b], Yoshiki Yamaguchi[c,1], Hiroshi Kurahashi[a,1], Yuji O. Kamatari[d], Shinju Sugiyama[a,e], Boran Uluca[f,g], Timo Piechatzek[f,g], Yusuke Komi[a], Toshinobu Shida[a,e], Henrik Müller[f,g], Shinya Hanashima[c,h], Henrike Heise[f,g], Kazuo Kuwata[i], and Motomasa Tanaka[a,e,2]

[a]Laboratory for Protein Conformation Diseases, RIKEN Brain Science Institute, Wako, 351-0198 Saitama, Japan; [b]Department of Applied Chemistry, Tokyo University of Science, Shinjuku-ku, 162-8601 Tokyo, Japan; [c]Structural Glycobiology Team, RIKEN-Max Planck Joint Research Center, Wako, 351-0198 Saitama, Japan; [d]Life Science Research Center, Gifu University, 501-1193 Gifu, Japan; [e]School of Life Science and Technology, Tokyo Institute of Technology, Midori-ku, Yokohama, 226-8503 Kanagawa, Japan; [f]Institute of Physical Biology, University of Dusseldorf, 40225 Dusseldorf, Germany; [g]Institute of Complex Systems, ICS-6: Structural Biochemistry, Research Center Julich, 52425 Julich, Germany; [h]Department of Chemistry, Graduate School of Science, Osaka University, Toyonaka, 560-0043 Osaka, Japan; and [i]United Graduate School of Drug Discovery and Medical Information Sciences, Gifu University, 501-1194 Gifu, Japan

Edited by David Baker, University of Washington, Seattle, WA, and approved February 1, 2018 (received for review September 4, 2017)

Self-propagating β-sheet–rich fibrillar protein aggregates, amyloid fibers, are often associated with cellular dysfunction and disease. Distinct amyloid conformations dictate different physiological consequences, such as cellular toxicity. However, the origin of the diversity of amyloid conformation remains unknown. Here, we suggest that altered conformational equilibrium in natively disordered monomeric proteins leads to the adaptation of alternate amyloid conformations that have different phenotypic effects. We performed a comprehensive high-resolution structural analysis of Sup35NM, an N-terminal fragment of the Sup35 yeast prion protein, and found that monomeric Sup35NM harbored latent local compact structures despite its overall disordered conformation. When the hidden local microstructures were relaxed by genetic mutations or solvent conditions, Sup35NM adopted a strikingly different amyloid conformation, which redirected chaperone-mediated fiber fragmentation and modulated prion strain phenotypes. Thus, dynamic conformational fluctuations in natively disordered monomeric proteins represent a posttranslational mechanism for diversification of aggregate structures and cellular phenotypes.

yeast prion | amyloid | protein misfolding | protein dynamics | aggregate

Formation of protein aggregates including amyloid fibers is widely observed in a variety of organisms, including microorganisms and vertebrates, and is often associated with human diseases (1, 2). In contrast to the fact that polypeptides fold into unique native structures, amyloidogenic proteins frequently misfold into distinct aggregate conformations which can dictate different physiological consequences, such as cellular toxicity or tissue specificity (3–5). A classic example of this phenomenon is prion strains where prion protein particles apparently composed of the same protein lead to phenotypically distinct infectious and transmissible states (6–8). Previous studies show that distinct prion strains are caused by structural polymorphism in infectious prion amyloid (9–11). For example, amyloid fibers of Sup35NM, the intrinsically disordered N-terminal and middle (M) domain of yeast prion protein Sup35, the protein determinant of [*PSI*$^+$] prion states (7, 8), adopt distinct conformations at 4 °C (WT-4) and 37 °C (WT-37), and introduction of these conformational variants into yeast cells leads to mitotically stable strong and weak [*PSI*$^+$] strains, respectively (11, 12). Moreover, single point mutations in the amino acid sequence may alter the cellular phenotypes associated with the amyloidogenic protein. A single point mutation of Sup35 where serine 17 is replaced with arginine (S17R) induces characteristic sectoring (mitotically unstable), weak [*PSI*$^+$] strains (13, 14), and a codon polymorphism at residue 129 in human prion protein causes clinical diversity in Creutzfeldt–Jakob disease (6, 15). While distinct cellular phenotypes are likely caused by conformational differences in protein aggregates, it has been a critical open question how distinct structures of protein aggregates such as prions are created from the same monomeric protein. One leading hypothesis is that the difference in aggregate conformations may originate from structural diversity and fluctuation within the monomeric protein. In particular, Sup35NM, which is intrinsically disordered, might show monomer conformational heterogeneity (16, 17). Nonetheless, it remains unknown whether or how genetic mutations or environmental factors alter the dynamics or conformational equilibrium of intrinsically disordered Sup35NM monomers to induce the formation of distinct amyloid conformations with different phenotypic effects.

Results

Sup35NM Can Misfold into Two Strikingly Distinct Amyloid Conformations. To address this question, we first established methods to identify amyloid core regions, which are critical determinants of prion strain phenotypes (18), by limited proteolysis with proteinase K followed by mass spectral analysis for high and low molecular weight regions. When we analyzed WT-4 and WT-37 amyloid core regions of WT Sup35NM, the main peptides in the high molecular weight region

Significance

On the basis of the amino acid sequence, a polypeptide folds into a unique structure. In contrast, aggregation-prone proteins often misfold into distinct aggregate conformations. Interestingly, each distinct aggregate conformation can dictate different phenotypic consequences, such as cellular toxicity. However, the underlying mechanism of the origin of such structural diversity of protein aggregates has been a critical open question. Using the intrinsically disordered domain of yeast prion protein Sup35, we revealed the structural diversification of prion aggregate is triggered by thermodynamic fluctuations within the monomeric protein prior to aggregation. Our findings not only provide a clue to explain previously puzzling observations in prion biology but also have important implications for therapeutic approaches for human diseases in which protein aggregation is involved.

Author contributions: Y.O. and M.T. designed research; Y.O., Y.Y., H.K., Y.O.K., S.S., B.U., T.P., Y.K., T.S., H.M., S.H., and H.H. performed research; Y.O., Y.Y., H.K., H.H., K.K., and M.T. analyzed data; and Y.O., B.U., H.H., and M.T. wrote the paper.

The authors declare no conflict of interest.

This article is a PNAS Direct Submission.

Data deposition: The NMR chemical shifts have been deposited in the BioMagResBank, www.bmrb.wisc.edu/ (accession no. 12016).

[1]Y.Y. and H.K. contributed equally to this work.

[2]To whom correspondence should be addressed. Email: motomasa@brain.riken.jp.

This article contains supporting information online at www.pnas.org/lookup/suppl/doi:10.1073/pnas.1715483115/-/DCSupplemental.

Published online February 21, 2018.

were assigned to the amino acid regions 2–38, 2–42, 2–45, and 2–46 for WT-4 amyloid and 2–70, 2–71, and 2–72 for WT-37 amyloid. (Fig. 1 *A* and *C* and Table S1). This result mirrored previous results by hydrogen/deuterium exchange NMR experiments (18). With mass spectrometry of proteinase K-treated fibrils, we remarkably found that the S17R amyloid formed at 4 °C (S17R-4) and 37 °C (S17R-37) showed core regions of amino acids 81, 82–144, 147, and 148 and amino acids 62–144 and 63–144, respectively (Fig. 1 *B* and *C* and Table S1).

The unexpected existence of a C-terminal prion domain (PrD-C) amyloid core was further supported by solid-state NMR spectroscopy and proline-scanning analyses. Taking advantage of the fact that all four phenylalanines at positions 92, 104, 117, 129 are located in the PrD-C (Fig. 1*C*), we labeled Sup35NM WT and S17R proteins with Phe-1-^{13}C, formed amyloid fibers, and measured ^{13}C–^{13}C dipolar dephasing by constant-time RF-driven dipolar recoupling (CT-RFDR) of the amyloid by solid-state magic angle spinning (MAS) NMR spectroscopy (Fig. 1*D*)

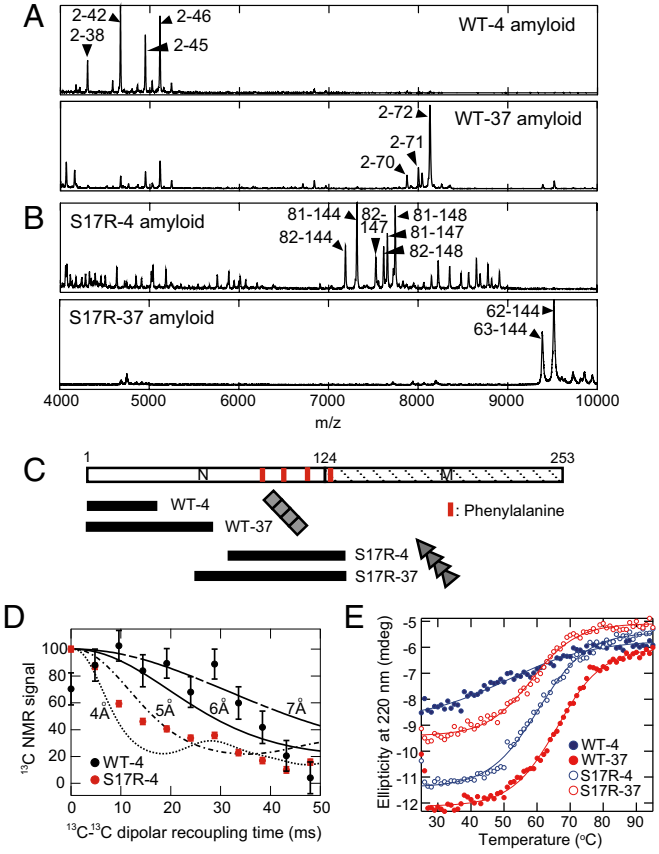

Fig. 1. Sup35NM can misfold into two strikingly distinct amyloid conformations. (*A*) High-*m/z*-range MALDI-TOF-MS spectra (*m/z* 4,000–10,000) of core peptides derived from WT-4 and WT-37 amyloids. Arrowheads indicate distinctive signals (amino acids 2–42/45/46 for WT-4 and amino acids 2–70/71/72 for WT-37). (*B*) High-*m/z*-range MALDI-TOF-MS spectra (*m/z* 4,000–10,000) of core peptides derived from S17R-4 and S17R-37 amyloids. Arrowheads indicate distinctive signals (amino acids 81/82–144/147/148 for S17R-4 and amino acids 62/63–144 for S17R-37). (*C*) Alignment of main core regions of WT and S17R amyloids detected by high-*m/z*-range MALDI-TOF-MS analysis. The red lines in the upper panel show the location of phenylalanine residues. (*D*) Solid-state NMR ^{13}C–^{13}C dipolar dephasing curves of Phe-1-^{13}C–labeled amyloids of Sup35NM WT (black) and S17R (red) formed at 4 °C. Simulated finite-pulse RFDR-CT (fpRFDR-CT) curves are shown for ideal linear chains of ^{13}C nuclei with distances of 4, 5, 6, and 7 Å. (*E*) Thermal disassembly of WT-4, WT-37, S17R-4, and S17R-37 amyloid fibers was monitored by the ellipticity at 220 nm with a CD spectrophotometer. Resulting plots were fitted by a sigmoidal curve for determination of T_m.

(19, 20). The S17R fibrils labeled with Phe-1-^{13}C showed a rate of signal decay characteristic for a distance of 4.5–5.0 Å to the nearest neighbor for all labeled Phe residues. This result indicated that all four Phe residues must be located in parallel, in-register β-sheets and thus confirmed the nature of the PrD-C core of S17R amyloid. In-register parallel β-sheet structures had been observed for WT fibrils with the N-terminal core before (19, 20). Furthermore, we performed proline scanning with thioflavin T (ThT) fluorescence, in which various single-proline Sup35NM mutants were polymerized in the presence of WT-4, WT-37, S17R-4, or S17R-37 seeds, and examined whether the replacement with proline, which cannot adopt β-sheet conformations, in Sup35NM monomers impairs seeding activity (Fig. S1*A*). We observed that mutational positions which showed seeding defects matched the amyloid core region identified by mass spectral analysis (Fig. S1 *B* and *C*). These results demonstrated that our method of limited proteolysis and mass spectrometry readily identified amyloid core regions without assignment of NMR signals of dimethyl sulfoxide-denatured protein (18).

The conformational differences between WT and S17R amyloids were further investigated by the analyses of thermal stability using circular dichroism (CD) spectroscopy. The CD spectrophotometer monitored changes of the ellipticity at 220 nm of amyloid solutions in the presence of SDS upon the increase of temperature from 25 °C to 95 °C. This experiment reports on amyloid disassembly as evidenced by the spectral changes from β-sheet/random coil-containing amyloid structures to random coil-rich monomer structures (Fig. S1*D*). Notably, the low secondary structure content estimated from the CD spectra of Sup35NM amyloid indicates that Sup35NM amyloid is constituted by both β-sheet–rich amyloid core and random coil regions. The T_m values calculated from the melting curves were different in WT-4 and WT-37 amyloids (WT-4: 55.7 ± 1.2, WT-37: 64.8 ± 0.3) but were similar in S17R-4 and S17R-37 amyloids (S17R-4: 57.9 ± 0.5, S17R-37: 56.2 ± 0.5) (Fig. 1*E*). Such different characteristics of T_m in WT and S17R amyloids are consistent with their distinct amyloid core regions (Fig. 1 *A*–*C*). Furthermore, our atomic force microscopy (AFM) analysis revealed that the S17R-4 and S17R-37 amyloid fibers have the propensity to exhibit more periodically twisted morphology than WT-4 and WT-37 fibrils, respectively (Fig. S2), implying that the WT and S17R amyloid structures are different. Finally, to examine the physiological consequences of the S17R amyloid, we performed a protein infection assay (11). The infectivities of in vitro-generated S17R-4 and S17R-37 amyloids to nonprion [*psi*$^-$] yeast were 2.8% and <0.1%, respectively, which were much lower than those of WT-4 and WT-37 amyloids (77.7% and 20.5%, respectively) (Fig. S1*E*). In most cases (>80%), the resulting [*PSI*$^+$(S17R)] strains showed sectoring/weak phenotypes (Fig. S1*F*), indicating unstable prion transmission, as previously reported (13, 14). Collectively, these results support the notion that the S17R mutation induces an amyloid structure that is markedly different from the amyloid conformation of WT Sup35NM.

WT Sup35NM Can Adopt the PrD-C Amyloid Core. To examine whether WT Sup35NM is able to adopt the S17R-type PrD-C amyloid core, we polymerized WT Sup35NM monomer in the presence of S17R amyloid seeds [5% (mol/mol)] and examined the resulting amyloid structures. First, we found that the S17R amyloid efficiently seeded WT Sup35NM (Fig. 2*A*), suggesting that WT Sup35NM is able to form the S17R-type amyloid conformation. Importantly, using the WT fibrils that were formed with S17R seeds [5% (mol/mol)] (denoted as "WT[S17R]"), we confirmed this hypothesis by the peaks in the high-*m/z* region of mass spectra (Fig. 2*B* and Table S1) and the low infectivity accompanied by the appearance of sectoring/weak [*PSI*$^+$] phenotypes in protein infection assays (Fig. S3 *A* and *B*), both of which are quite similar to the results obtained with S17R amyloid (Fig.

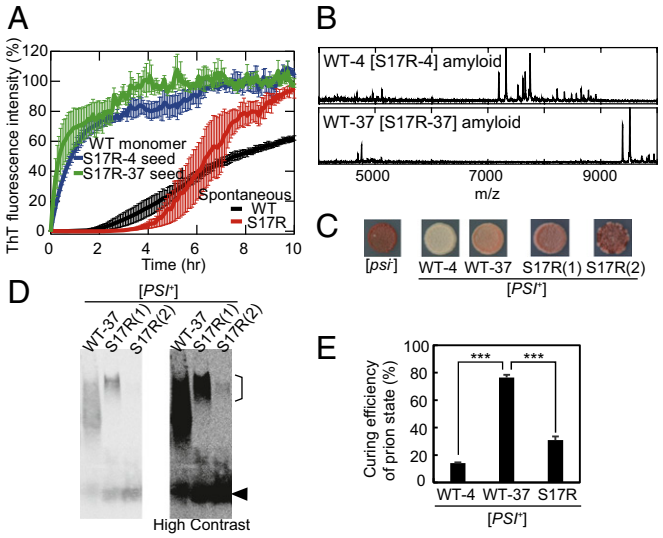

Fig. 2. Wild-type Sup35NM can adopt the PrD-C amyloid core. (*A*) Kinetics of spontaneous WT and S17R amyloid formation and seeding reaction with WT monomer and S17R-4 and S17R-37 seeds monitored by ThT fluorescence at 25 °C. Error bars denote SEM. (*B*) High-*m/z*-range MALDI-TOF-MS spectra (*m/z* 4,000–10,000) of core peptides derived from cross-seeded WT[S17R] amyloid formed at 4 °C (WT-4[S17R-4]) and 37 °C (WT-37[S17R-37]). (*C*) Weak/sectoring phenotypes of two examples of [*PSI*$^+$(S17R)] strains obtained by overexpression of the Sup35NM S17R mutant in [*psi*$^-$] yeast. Phenotypes of [*PSI*$^+$(WT-4)] and [*PSI*$^+$(WT-37)] strains and [*psi*$^-$] yeast are also shown as controls. (*D*) SDD-AGE analysis with yeast lysates of [*PSI*$^+$(WT-37)] and [*PSI*$^+$(S17R)] strains probed by an anti-Sup35NM antibody. A high-contrast image is shown on the right. An arrowhead and a line in the high molecular region indicate the positions of monomeric Sup35NM and S17R-type prions, respectively. Note that [*PSI*$^+$(S17R (2))] strains also contain a large size of prion aggregates. (*E*) Efficiency of [*PSI*$^+$]-state curing of [*PSI*$^+$(WT-4)], [*PSI*$^+$(WT-37)], and [*PSI*$^+$(S17R)] strains by Hsp104 overexpression. [*PSI*$^+$(S17R)] strains were generated by in vitro infection of Sup35NM S17R-4 or S17R-37 amyloid fibers in [*psi*$^-$] yeast. The curing efficiency of [*PSI*$^+$(S17R)] is an average of the data from the two [*PSI*$^+$(S17R)] strains. Error bars denote SEM. ***P < 0.001 by a Student's t test; $n \geq 3$.

S1 *E* and *F*). Furthermore, we found that the addition of 1 M sodium chloride to the amyloid formation buffer induced a S17R-type amyloid conformation even for WT Sup35NM (Fig. S3*C* and Table S1). In addition, the Sup35NM mutant lacking residues 2–34 (Δ2–34) could form an amyloid conformation with a PrD-C core (Fig. S3*D* and Table S1). These results established that WT Sup35NM has the intrinsic potential to form two strikingly different amyloid conformations, either of which is eventually selected depending on amino acid sequences and/or solvent conditions for amyloid formation.

How does the PrD-C core of S17R amyloid induce the characteristic sectoring phenotypes in [*PSI*$^+$(S17R)] strains which are obtained when the GFP-fused S17R mutant is overexpressed (13) or when in vitro-generated S17R amyloid is introduced in [*psi*$^-$] yeast (Fig. 2*C* and Fig. S1*F*)? The mitotically unstable/sectoring phenotypes of [*PSI*$^+$(S17R)] strains suggest reduced chaperone-mediated fiber fragmentation. If this is the case, we would expect to observe an increased size of prion aggregates in [*PSI*$^+$(S17R)] strains. Therefore, we examined the size of prion aggregates in two representative weak [*PSI*$^+$(S17R)] strains as well as weak [*PSI*$^+$(WT-37)] strains (Fig. 2 *C* and *D*). We employed a semidenaturing detergent agarose gel electrophoresis (SDD-AGE) (21) to address it, since SDD-AGE previously revealed a difference in the prion size between [*PSI*$^+$(WT-4)] and [*PSI*$^+$(WT-37)] strains (12). As we expected, the average size of [*PSI*$^+$(S17R)] prions was larger than that of WT-37 prions (Fig. 2*D*). Importantly, the increased prion size did not result from enhanced seeding extension reactions of [*PSI*$^+$(S17R)] prions, as the seeding activity of S17R amyloid to WT monomer was similar to that of WT amyloid to WT monomer at 30 °C in vitro (Fig. S3*E*). These results suggested impairment of chaperone-mediated fragmentation of [*PSI*$^+$(S17R)] prion aggregates, although the fragmentation defect was not so severe as to eliminate the [*PSI*$^+$(S17R)] prion state. Since Hsp70/Hsp40 chaperones first bind to prion aggregates and then recruit Hsp104 (22), an AAA+ ATPase chaperone essential to prion propagation (23), our observations imply that the PrD-C region, which is buried in [*PSI*$^+$(S17R)] prion aggregates, partly includes a binding site of Hsp70/Hsp40.

A recent study showed that residues 129–148 in Sup35 are involved in binding to overexpressed Hsp104 (24). Interestingly, the PrD-C core region of S17R amyloid overlaps with this binding site, suggesting that the curing of [*PSI*$^+$(S17R)] strains by Hsp104 overexpression may be compromised due to residues 80–148 being buried in the amyloid core. Indeed, we found that [*PSI*$^+$(S17R)] strains were more resistant to [*PSI*$^+$] curing by Hsp104 overexpression than [*PSI*$^+$(WT-37)] strains (Fig. 2*E*), although the [*PSI*$^+$(S17R)] strains had been expected to be cured more easily due to their larger size and smaller amounts of prions than the [*PSI*$^+$(WT-37)] strains (Fig. 2*D*). Overexpressed Hsp104 is suggested to bind to Sup35 prion aggregates in the initial step of [*PSI*$^+$] curing, which prevents Hsp70/Hsp40 from having access to prion aggregates, resulting in a loss of [*PSI*$^+$] states (24). The acquired resistance of [*PSI*$^+$(S17R)] yeast to the curing would be caused by impaired binding of overexpressed Hsp104 to the [*PSI*$^+$(S17R)] prions, as observed for Δ129–148 Sup35 prions (24).

Sup35NM Monomers Form Compact Local Structures with Long-Range Interactions. We asked how such a dramatic difference in amyloid conformation might be caused by the single S17R mutation although both WT and S17R Sup35NM monomers have similar disordered structures (Fig. S4*A*). To address this question at amino acid resolution, we performed a comprehensive assignment of protein backbone ^{1}H-^{15}N NMR chemical shifts of Sup35NM. This had been a challenge, because Sup35NM is a relatively large protein (253 residues) for signal assignment, the aggregation-prone property limits the measurement time of NMR, and both the intrinsically disordered structure and the presence of 5.5 degenerate oligopeptide repeats cause severely impaired signal separation. Nonetheless, we completed the amino acid assignment of more than 90% of ^{1}H-^{15}N HSQC signals for the Sup35NM monomer.

First, we investigated the amino acid residues required for oligomer formation by NMR, since oligomers play an important role in determining amyloid conformation (25). We acquired ^{1}H-^{15}N HSQC spectra at several temperatures from 37 °C to 7 °C and quantified temperature-dependent changes in NMR signal intensities (Fig. 3 *A* and *B*). While analytical ultracentrifugation showed that Sup35NM under the NMR measurement condition is solely monomeric at 37 °C (Fig. S4*B*), the temperature-dependent reduction of NMR signal intensities from 37 °C to 7 °C implies protein assembly due to decreased tumbling rates of protons (Fig. 3 *B* and *C*). This result is consistent with our previous observation that Sup35NM is a monomeric form at 37 °C but forms oligomers at low temperatures (25). In particular, residues 45–90 showed a gradual reduction in signal intensity as the temperature decreased (yellow area in Fig. 3*B*), indicating that these residues are involved in oligomer formation. We observed a slight decrease in the amount of oligomers in the S17R mutant, but no major difference between WT and the S17R mutant was detected in the amino acid region required for oligomer formation (Fig. 3 *B* and *C*).

Next, we examined oligomer structures by saturation transfer difference (STD) NMR spectroscopy at 22 °C, the temperature at which both Sup35NM monomer and oligomer are populated (Fig. 3*C*). By mixing unlabeled (^{1}H^{14}N) Sup35NM with ^{2}H^{15}N-labeled Sup35NM proteins and saturating the ^{1}H signals in

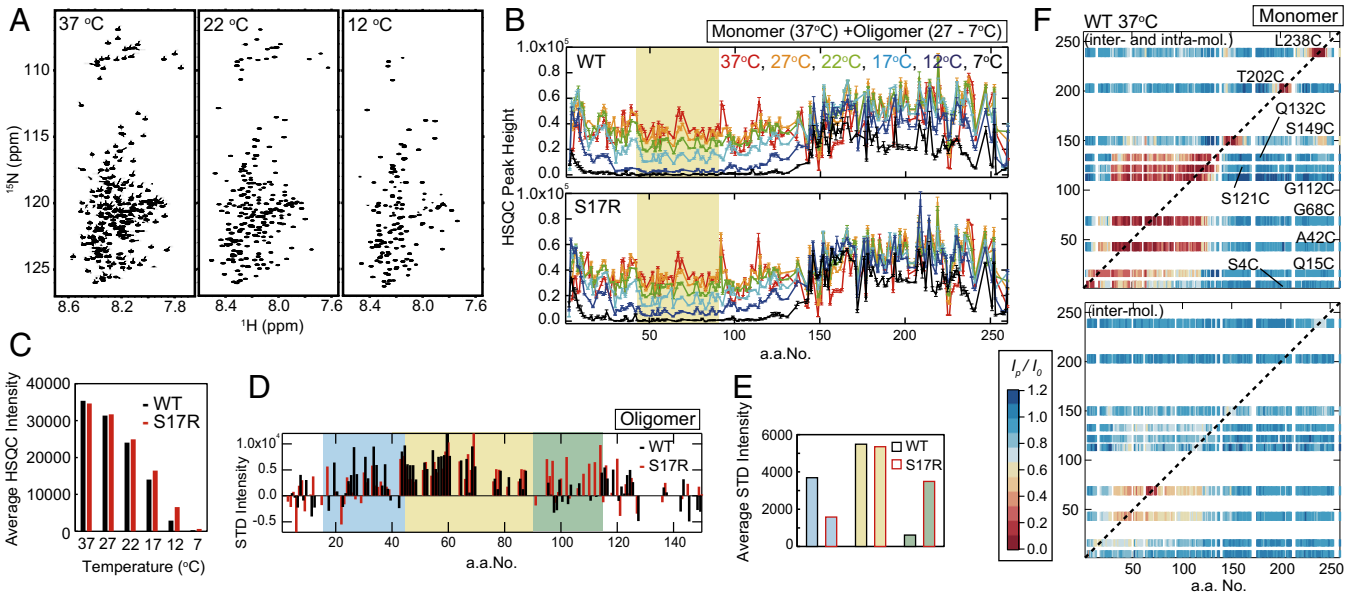

Fig. 3. Sup35NM monomers form latent compact local structures with long-range interactions. (*A*) Temperature-dependent changes of ^{1}H-^{15}N HSQC spectra of WT Sup35NM. (*B*) Signal intensities for ^{1}H-^{15}N cross-peaks in an HSQC spectrum of WT and S17R Sup35NM at 37 °C (red), 27 °C (orange), 22 °C (green), 17 °C (cyan), 12 °C (blue), and 7 °C (black). The yellow area indicates the amino acid region with significantly reduced signal intensities at low temperature, indicating the oligomer core region. (*C*) Temperature-dependent change of average ^{1}H-^{15}N HSQC signals in the yellow area in B (amino acids 45–90). (*D*) STD signal intensity of the N domain of WT (black) and S17R Sup35NM (red) at 22 °C. The blue and green areas indicate the amino acid regions with increased STD signals specific to WT and S17R Sup35NM, respectively. (*E*) Averaged STD signal intensities in the blue (amino acids 15–44), yellow (amino acids 45–90), and green (amino acids 91–115) areas in *D* are indicated by blue, yellow, and green bars, respectively. (*F*) Paramagnetic relaxation enhancement of WT Sup35NM monitored by ^{1}H-^{15}N HSQC signal intensity. A MTSL spin probe was introduced into each selected single-cysteine Sup35NM mutant (S4C, Q15C, A42C, G68C, G112C, S121C, Q132C, S149C, T202C, and L238C). Inter/intramolecular (*Upper*) and intermolecular (*Lower*) PRE values at 37 °C are shown as a color scale showing the ratio of the HSQC intensity of PRE measurement to the HSQC intensity of control measurement (I_p/I_0 ratio). The red color of high PRE values indicates the presence of interactions between a MTSL spin probe and an amino acid residue of interest.

unlabeled Sup35NM, STD signals can be observed only if the two molecules directly interact with each other due to the transfer of magnetization from excited unlabeled Sup35NM to ^{2}H^{15}N-labeled Sup35NM. Therefore, the STD measurements provide information on monomer–monomer contacts in oligomers. Fig. 3*D* shows the STD signal intensities in the N-terminal prion domain and a part of the M domain, which are involved in prion propagation (26). As expected from the results shown in Fig. 3*B*, residues 45–90, which are located in the oligomer core region, showed STD signals for both the WT and the S17R mutant (yellow area in Fig. 3 *D* and *E* and Fig. S5*A*). Interestingly, we found that amino acid regions 15–44 and 91–115 specifically showed STD signals in the WT and S17R mutant, respectively (blue and green areas in Fig. 3 *D* and *E* and Fig. S5*A*). This result indicated that the different regions are involved in intermolecular interactions and thus may represent initiation sites for amyloid formation in WT and S17R mutant Sup35NM, respectively. In addition, the STD analysis showing that the amino acid residues required for intermolecular interactions are different in WT and S17R mutant Sup35NM implies that their nucleus structures are distinct from each other.

Furthermore, we measured ^{1}H-^{15}N heteronuclear Overhauser effects (NOE) at 37 °C (Fig. S5*B*), the temperature at which Sup35NM is populated only in a monomeric state (Fig. S4*B*), to examine structural fluctuation of Sup35NM monomer. Remarkably, the positive heteronuclear NOE values in the region of residues 30–110 suggested the presence of a locally compact structure (Fig. S5*B*) despite the overall disordered Sup35NM conformation (Fig. S4*A*). In contrast, negative heteronuclear NOE values throughout the M domain showed that the M domain is mostly unfolded (Fig. S5*B*). We performed further NMR experiments that report on two different time scale dynamics, T_1 and T_2 relaxation time measurements (nanoseconds and picoseconds) (Fig. S5 *C* and *D*) and paramagnetic relaxation enhancement (PRE) (microseconds) experiments with a paramagnetic spin probe, 1-oxyl-2,2,5,5-tetramethylpyrroline-3-methyl) methanethiosulfonate (MTSL), which was specifically introduced into a variety of single-cysteine Sup35NM mutants (Fig. 3*F* and Fig. S5*E*). The shorter relaxation times and the large PRE effects in the N-terminal prion domain revealed the presence of local compact structures by long-range interactions, while the longer relaxation times and the absence of PRE effects in the M domain showed that the M domain is largely unfolded. Taken together, these results show that the prion domain in Sup35NM adopts local compact structures by long-range interactions despite its overall intrinsically disordered structure (Fig. S4*A*); this was hypothesized in a previous single-molecule FRET study (17), but its biological significance had not been fully addressed.

Exposed Asparagine Residues in Sup35NM Monomers Are Scaffolds for Amyloid Formation. The fast time-scale protein dynamics was not significantly different between Sup35NM WT and the S17R mutant by our NMR analyses with PRE, T_1, and T_2 measurements (Fig. 3*F* and Fig. S5 *C*–*E*). Therefore, to gain insights into slow time-scale dynamics (in milliseconds) of the Sup35NM monomer at 37 °C, we applied phase-modulated CLEAN chemical exchange (CLEANEX-PM) NMR spectroscopy which allows us to examine backbone amide ^{1}H exchange rates with the solvent protons and thereby identify which residues are solvent-exposed or buried/hydrogen-bonded (27). We revealed that most of the amino acids in the prion domain of the S17R mutant monomer showed higher exchange rates than those in the WT monomer (Fig. 4 *A*–*C* and Fig. S5*F*), indicating that the local compact structure of the S17R mutant monomer is more unfolded than that of the WT monomer. Therefore, the S17R mutation altered the conformational space of the Sup35NM monomer, resulting in an increased population of the monomer conformation containing a less compact prion domain.

Interestingly, the asparagine residues located at both ends (residues 15–44 and 91–115) of the local compact region in the Sup35NM monomer showed significantly higher exchange rates in the S17R mutant (blue and green areas in Fig. 4 *A*–*C*), indicating that specific asparagine residues are more solvent-exposed in the S17R mutant than in the WT monomer. To examine effects of the exposed asparagine residues (Asn8, 19, 26, and 27 in the N-terminal core region and Asn100, 103, 105, and 109 in the C-terminal core region) on the formation of the WT and S17R-type amyloid cores, we prepared a range of Sup35NM mutants in which single or a few exposed asparagine residues were replaced with alanine together with or without the S17R mutation. For asparagine mutants in the N-terminal core region, we found that the N8A/N19A/N26A mutant partially acquired the PrD-C amyloid core at 4 °C (Fig. S6 *A* and *B*). Remarkably, we further found that the triple mutant S17R/N100A/N109A restored the WT-type N-terminal amyloid core both at 4 °C and 37 °C (Fig. 4*D* and Table S1), and the mutant amyloids which formed at 4 °C and 37 °C showed melting curves similar to WT-4 and WT-37 amyloids, respectively (Fig. 4*E*). Importantly, the S17R/N100A/N109A mutant still has the capability to form a PrD-C amyloid core when seeded by S17R amyloid (Fig. S6*C* and Table S1), excluding the possibility that the two N100A/N109A mutations introduced into the S17R mutant exert their effects on the amyloid state simply by preventing the mutant from having access to the PrD-C core. These results show that the exposed Asn100 and Asn109 residues are required for the S17R mutant to form the PrD-C amyloid core.

If the S17R mutant is more unfolded and both potential amyloid core regions are exposed, why does the S17R mutant selectively adopt the PrD-C amyloid core but not the N-terminal core? The STD data revealed that intermolecular interactions of S17R monomers resulted from the contacts between amino acids 91–115, suggesting that Arg17 in the S17R mutant reduced intermolecular interactions involving amino acids 15–44 while increasing intermolecular contacts involving amino acids 91–115 (Fig. 3 *D* and *E*). Consistently, the seeding assay showed that S17R monomers are incorporated into the WT-4 or WT-37 amyloid seeds, albeit more slowly than WT monomers (Fig. 4*F*), indicating that the S17R mutant still has the capability to adopt (Fig. S6*D* and Table S1) but does not prefer to form an N-terminal amyloid core. These factors would allow the S17R mutant to eventually select a PrD-C amyloid core upon aggregation.

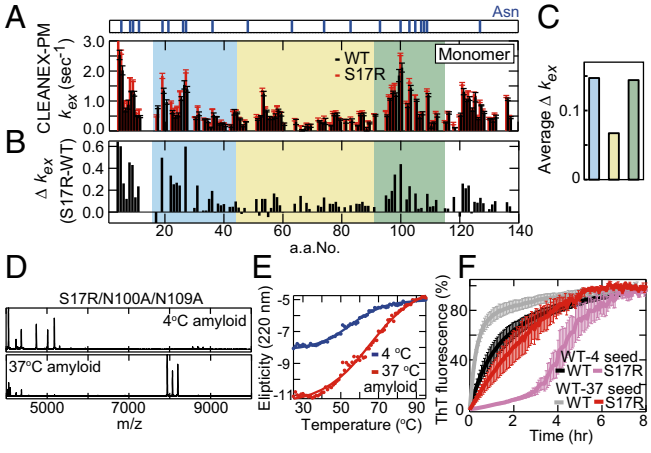

Fig. 4. Exposed asparagine residues outside the compact region in disordered Sup35NM monomers serve as a scaffold for amyloid formation. (*A*) Hydrogen exchange rates of the N domain of WT (black) and S17R Sup35NM (red) at 37 °C measured by CLEANEX-PM NMR. The positions of asparagine residues are shown as blue lines in the upper panel. (*B*) Difference in the exchange rates (k_{ex} S17R – k_{ex} WT) between WT and S17R Sup35NM. Color coding is as in Fig. 3*D*. (*C*) Averaged differences in the exchange rates in amino acids 15–44, 45–90, and 91–115 are indicated by blue, yellow, and green bars, respectively. (*D*) High-*m*/*z*-range MALDI-TOF-MS spectra (*m*/*z* 4,000–10,000) of core peptides derived from S17R/N100A/N109A amyloid formed at 4 °C and 37 °C. (*E*) Thermal disassembly of S17R/N100A/N109A amyloid fibers formed at 4 °C (blue) and 37 °C (red) was monitored by the ellipticity at 220 nm with a CD spectrophotometer. (*F*) Kinetics of amyloid formation of WT (black) and S17R (pink) monomers in the presence of WT-4 seeds and WT (gray) and S17R (red) monomers in the presence of WT-37 seeds at 25 °C. Error bars denote SEM.

Discussion

In this study, we revealed that Sup35NM is able to form two strikingly different amyloid conformations that can be selectively propagated and result in alternate strain phenotypes. These conformational subtypes of amyloid derive from the disinhibition of local compact structures of monomeric Sup35NM. Our comprehensive NMR analysis of Sup35NM at amino acid resolution indicates that exposed asparagine residues in the Sup35NM monomer serve as initiation sites for amyloid elongation and constitute an amyloid core. In WT Sup35NM, Asn100 and Asn109 are buried in the local compact structure, and thereby the N-terminal amyloid core region is selected (Fig. S7). In contrast, the S17R mutation alters the conformational equilibrium of monomer and increases the population of an unfolded form with exposed asparagine residues in the C-terminal region of the prion domain. The exposure of Asn100/Asn109 and the preference of the intermolecular contacts of the PrD-C region allow the S17R mutant to select Asn100 and Asn109 as an initiation site for amyloid formation (Fig. S7). The altered intermolecular contacts due to the unfolded nature of the S17R Sup35NM monomer would result in the formation of different nucleus structures, which could also contribute to the selection of the PrD-C amyloid core. Taken together, our results highlight that exposed asparagine residues at the edge of the local compact region in Sup35NM monomer play pivotal roles in determining Sup35 amyloid conformation and suggest that the unfolding of the local compact structure by the S17R mutation triggers selective formation of the PrD-C amyloid core.

A previous report showed that Ser17 is involved in a tight-turn structure in Sup35NM fibrils and thus is located at a strategic position (28). Importantly, the selection of the C-terminal amyloid core of the S17R mutant is not caused simply by its inability to accommodate the bulky and charged Arg17 residue into an N-terminal amyloid core. We revealed that both the triple S17R/N100A/N109A mutant and the single S17R mutant have the capability to adopt an N-terminal amyloid core (Fig. 4*D* and Fig. S6*D* and Table S1). This result shows that such a charged and/or bulky residue at the strategic position 17 can be accommodated into an N-terminal amyloid core. Furthermore, we found that the mutation of Ser17 to either bulky tryptophan or tyrosine, which might destabilize the tight-packing structures within the amyloid core, maintained the formation of an N-terminal amyloid core (Fig. S6 *E* and *F* and Table S1). Together, these results show that potential destabilization of the N-terminal core by Arg17 would not be a major factor in the formation of the PrD-C amyloid core in the S17R mutant. Rather, our data suggest that disruption of the latent compact structure in the S17R monomer and resulting exposure of Asn100 and Asn109 in the monomeric state are involved in the selection of the PrD-C amyloid core in the S17R mutant. The PrD-C amyloid core would decrease the efficiency of chaperone-mediated fiber fragmentation, resulting in the large prion size and weak/sectoring (mitotically unstable) phenotypes of [*PSI*$^+$(S17R)] strains. This result agrees well with our previous finding that fiber fragmentation rates have a greater impact on prion strain phenotypes (11). The present study indicates that dynamic structural fluctuation in natively disordered monomeric proteins is involved in the diversification of amyloid conformations dictating distinct physiological consequences.

Notably, the prion strain conformation harboring a PrD-C core that we showed in this study provides a molecular explanation for many previous findings whose underlying mechanisms had remained elusive. First, it is suggested that the first 137 amino acids of Sup35 are required for faithful maintenance of weak [*PSI*$^+$] strains (26). This observation agrees well with the PrD-C core region of the S17R-type weak prion strain conformation. Furthermore, it should be noted that protein fluctuation of Sup35NM monomer is dramatically increased from residue 140 (Fig. S5 *B–D*), which may be associated with the C-terminal end position (residues 144–148) (Table S1) of the PrD-C amyloid core. Next, the Sup35 mutant lacking a region between positions 22 and 69 forms highly unstable prions in vivo (29). The deletion of residues 22–69 is likely to disrupt the latent local compact structure, potentially generating a PrD-C amyloid core upon aggregation of the deletion mutant. In addition, a wild-type [*PSI*$^+$] variant that is insensitive to excess Hsp104 for its curing has been reported (30), and chaotropic anions including Cl^- favor the formation of weaker Sup35NM prion variants (31). These observations could result from a prion strain conformation harboring a PrD-C core.

Furthermore, our results resolve the long-standing, puzzling observation that Sup35NM forms amyloid in a head-to-head and tail-to-tail manner (32) although this amyloid conformation may not reconcile with the unique N-terminal amyloid core demonstrated by hydrogen/deuterium exchange NMR experiments (18) or the in-register parallel structure demonstrated by solid-state NMR spectroscopy (19, 20). Rather, our findings suggest that Sup35NM may be able to adopt both N-terminal and PrD-C amyloid core regions simultaneously, since solvent conditions or protein modification by chemicals such as pyrene could modulate the conformational equilibrium of Sup35NM monomers. The present study underscores the critical role of conformational space in natively disordered proteins for determination of amyloid conformation. Therefore, the regulation of conformational fluctuation can be a target for therapeutic intervention of pathologic protein aggregates. More broadly, our findings suggest that structural fluctuation in intrinsically disordered monomeric proteins, and its controlling factors, can account for individual variation in cellular and organism-wide behaviors, adding to posttranslational mechanisms for phenotypic diversification in biological systems.

Methods

Amyloid Formation. Sup35NM amyloid formed spontaneously in 5 mM potassium phosphate buffer including 150 mM NaCl at pH 7.4 (buffer C) with mild agitation [by eight end-over-end rotations per minute (Labquake, Theromo Fisher Scientific)] within 24 h. The second generation (G2) of amyloid is formed by polymerization of Sup35NM in the presence of 5% (mol/mol) sonicated amyloid that was spontaneously formed without agitation within several hours, as previously described (11–13). Spontaneously formed amyloids were used in kinetics experiments for amyloid formation, and G2 or third-generation (G3) amyloids were used in the other amyloid experiments.

NMR Measurement of HSQC Spectra. Lyophilized Sup35NM was dissolved in 50 mM Mes buffer including 10% D_2O (pH 5.0). After filtration by a 100-kDa-cutoff spin filter, Sup35NM concentration and pH were adjusted to 100 μM and pH 5.2. HSQC spectra were acquired with an Avance III 600 spectrometer equipped with a cryogenic probe. The NMR data were processed by TopSpin (Bruker BioSpin) or XWINNMR (Bruker BioSpin) and analyzed by SPARKY (https://www.cgl.ucsf.edu/home/sparky).

ACKNOWLEDGMENTS. We thank Naomi Takahashi for preparation of reagents; Drs. Herry Martadinata, Santhosh Ayalur Karunakaran, Manuel Etzkorn, Vadim Zorin, and the members of the M.T. laboratory for discussions; and Charles Yokoyama for critical reading and editing of the manuscript. DNA sequencing and mass spectrometry were performed by the RIKEN Brain Science Institute Research Resources Center. Funding was provided by the Next Program Grant LS129 from the Japan Society of the Promotion of Science (to M.T.); Grant-in-Aid for Scientific Research on Innovative Area "Molecular Science of Fluctuations toward Biological Functions" 23107734 (to Y.O.); Grant-in-Aid for Young Scientists (B) 23770193 (to Y.O.); Grant-in-Aid for Scientific Research (B) 15H04345 (to M.T.) from the Ministry of Education, Culture, Sports, Science and Technology, Japan; and Grants-in-Aid from the Ministry of Health, Labour, and Welfare, Japan (the Research Committee of Prion Disease and Slow Virus Infection) (Y.O., K.K., and M.T.), RIKEN Pioneering Projects, Cellular Evolution (M.T.), and the Mochida Foundation (M.T.). This work was also funded in part by the Heinrich Heine International Graduate School of Protein Science and Technology of the Heinrich Heine University Dusseldorf and a Forschungszentrum Julich Germany Fellowship (T.P.). B.U. was supported by the International Helmholtz Research School of Biophysics and Soft Matter.

1. Eisenberg D, Jucker M (2012) The amyloid state of proteins in human diseases. *Cell* 148:1188–1203.
2. Knowles TP, Vendruscolo M, Dobson CM (2014) The amyloid state and its association with protein misfolding diseases. *Nat Rev Mol Cell Biol* 15:384–396.
3. Petkova AT, et al. (2005) Self-propagating, molecular-level polymorphism in Alzheimer's beta-amyloid fibrils. *Science* 307:262–265.
4. Tanaka M, Komi Y (2015) Layers of structure and function in protein aggregation. *Nat Chem Biol* 11:373–377.
5. Tycko R (2015) Amyloid polymorphism: Structural basis and neurobiological relevance. *Neuron* 86:632–645.
6. Collinge J, Clarke AR (2007) A general model of prion strains and their pathogenicity. *Science* 318:930–936.
7. Liebman SW, Chernoff YO (2012) Prions in yeast. *Genetics* 191:1041–1072.
8. Tuite MF, Serio TR (2010) The prion hypothesis: From biological anomaly to basic regulatory mechanism. *Nat Rev Mol Cell Biol* 11:823–833.
9. King CY, Diaz-Avalos R (2004) Protein-only transmission of three yeast prion strains. *Nature* 428:319–323.
10. Legname G, et al. (2004) Synthetic mammalian prions. *Science* 305:673–676.
11. Tanaka M, Chien P, Naber N, Cooke R, Weissman JS (2004) Conformational variations in an infectious protein determine prion strain differences. *Nature* 428:323–328.
12. Tanaka M, Collins SR, Toyama BH, Weissman JS (2006) The physical basis of how prion conformations determine strain phenotypes. *Nature* 442:585–589.
13. Chien P, DePace AH, Collins SR, Weissman JS (2003) Generation of prion transmission barriers by mutational control of amyloid conformations. *Nature* 424:948–951.
14. DePace AH, Santoso A, Hillner P, Weissman JS (1998) A critical role for amino-terminal glutamine/asparagine repeats in the formation and propagation of a yeast prion. *Cell* 93:1241–1252.
15. Collinge J, Sidle KC, Meads J, Ironside J, Hill AF (1996) Molecular analysis of prion strain variation and the aetiology of 'new variant' CJD. *Nature* 383:685–690.
16. Marchante R, Rowe M, Zenthon J, Howard MJ, Tuite MF (2013) Structural definition is important for the propagation of the yeast [PSI+] prion. *Mol Cell* 50:675–685.
17. Mukhopadhyay S, Krishnan R, Lemke EA, Lindquist S, Deniz AA (2007) A natively unfolded yeast prion monomer adopts an ensemble of collapsed and rapidly fluctuating structures. *Proc Natl Acad Sci USA* 104:2649–2654.
18. Toyama BH, Kelly MJ, Gross JD, Weissman JS (2007) The structural basis of yeast prion strain variants. *Nature* 449:233–237.
19. Shewmaker F, Kryndushkin D, Chen B, Tycko R, Wickner RB (2009) Two prion variants of Sup35p have in-register parallel beta-sheet structures, independent of hydration. *Biochemistry* 48:5074–5082.
20. Shewmaker F, Wickner RB, Tycko R (2006) Amyloid of the prion domain of Sup35p has an in-register parallel beta-sheet structure. *Proc Natl Acad Sci USA* 103:19754–19759.
21. Bagriantsev S, Liebman SW (2004) Specificity of prion assembly in vivo. [PSI+] and [PIN+] form separate structures in yeast. *J Biol Chem* 279:51042–51048.
22. Winkler J, Tyedmers J, Bukau B, Mogk A (2012) Hsp70 targets Hsp100 chaperones to substrates for protein disaggregation and prion fragmentation. *J Cell Biol* 198: 387–404.
23. Chernoff YO, Lindquist SL, Ono B, Inge-Vechtomov SG, Liebman SW (1995) Role of the chaperone protein Hsp104 in propagation of the yeast prion-like factor [psi+]. *Science* 268:880–884.
24. Helsen CW, Glover JR (2012) Insight into molecular basis of curing of [PSI+] prion by overexpression of 104-kDa heat shock protein (Hsp104). *J Biol Chem* 287:542–556.
25. Ohhashi Y, Ito K, Toyama BH, Weissman JS, Tanaka M (2010) Differences in prion strain conformations result from non-native interactions in a nucleus. *Nat Chem Biol* 6:225–230.
26. Bradley ME, Liebman SW (2004) The Sup35 domains required for maintenance of weak, strong or undifferentiated yeast [PSI+] prions. *Mol Microbiol* 51:1649–1659.
27. Hwang TL, van Zijl PC, Mori S (1998) Accurate quantitation of water-amide proton exchange rates using the phase-modulated CLEAN chemical EXchange (CLEANEX-PM) approach with a Fast-HSQC (FHSQC) detection scheme. *J Biomol NMR* 11:221–226.
28. Luckgei N, et al. (2013) The conformation of the prion domain of Sup35p in isolation and in the full-length protein. *Angew Chem Int Ed Engl* 52:12741–12744.
29. Borchsenius AS, Wegrzyn RD, Newnam GP, Inge-Vechtomov SG, Chernoff YO (2001) Yeast prion protein derivative defective in aggregate shearing and production of new 'seeds'. *EMBO J* 20:6683–6691.
30. Borchsenius AS, Müller S, Newnam GP, Inge-Vechtomov SG, Chernoff YO (2006) Prion variant maintained only at high levels of the Hsp104 disaggregase. *Curr Genet* 49:21–29.
31. Rubin J, et al. (2013) Ion-specific effects on prion nucleation and strain formation. *J Biol Chem* 288:30300–30308.
32. Krishnan R, Lindquist SL (2005) Structural insights into a yeast prion illuminate nucleation and strain diversity. *Nature* 435:765–772.

Supporting Information

Ohhashi et al. 10.1073/pnas.1715483115

SI Methods

Yeast Strains. We used isogenic [*psi*$^-$][*PIN*$^+$] and [*PSI*$^+$] derivatives of the 74D-694 yeast strain (1). [*PSI*$^+$(WT-4)] and [*PSI*$^+$(WT-37)] strains were generated by infection of [*psi*$^-$] yeast with in vitro-generated Sup35NM WT-4 and WT-37 amyloid formed at 4 °C and 37 °C, respectively (1). [*PSI*$^+$(S17R)] strains were generated by overexpression of the Sup35NM S17R mutant with a C-terminal GFP tag or introduction of in vitro-generated Sup35-NM S17R amyloid in [*psi*$^-$] yeast. Both the overexpression and infection experiments induced similar weak/sectoring phenotypes of [*PSI*$^+$(S17R)] strains.

Plasmid Construction. For bacterial expression of Sup35NM, pAED4, or pET29b vectors including a C-terminal 7× histidine-tag were used (1–3). Mutations were introduced by site-directed mutagenesis (Takara Bio.) and confirmed by DNA sequencing.

Expression and Purification of Sup35NM Protein. Nonlabeled and uniformly ^{15}N-labeled Sup35NM was overexpressed in the bacterial strain Rosetta (DE3) and purified by nickel-nitrilotriacetic acid histidine-tag affinity chromatography and cation-exchange chromatography under denaturing conditions as previously reported (1–3). For purification of cysteine mutants, 5 mM 2-mercaptoethanol was added to the buffer. Uniformly ^{2}H,^{15}N-labeled Sup35NM was overexpressed in Spectra 9 medium (Cambridge Isotope Laboratories, Inc.) and purified in the same manner. The Sup35NM protein was desalted by reverse-phase HPLC chromatography (Hitachi) using a Protein-R column (Nacalai Tesque) followed by lyophilization.

Mass Spectral Analysis of Amyloid Core. G2 or the G3 amyloid was treated with proteinase K (0.15 mg/mL) for 1 h at room temperature (4, 5). Proteinase K-resistant amyloid fibers were collected by ultracentrifugation (154,000 × *g* for 30 min), and the pellets were dissolved in 6 M guanidine hydrochloride, 10 mM Tris·HCl (pH 7.5). The dissociated amyloid core peptides were desalted by NuTip C-4 or C-18 (Glygen Corporation) and analyzed by MALDI-TOF-MS (microflex, Bruker Daltonics) and MALDI-TOF/TOF-MS (4800 Plus MALDI TOF/TOF Analyzer, AB SCIEX) for mass spectral analysis of high and low molecular weight regions, respectively. MS spectra were calibrated by bovine ubiquitin. High molecular weight MS data were analyzed using PAWS software (ProteoMetrics).

T_m Analysis. Freshly prepared Sup35NM G2 amyloid was used at concentration of 5 μM in buffer C including 1% SDS that inhibits reaggregation of dissociated proteins. The thermal disassembly of amyloids was examined by the temperature-scanning mode of CD spectroscopy (J-818 Spectropolarimeter; JASCO) at the wavelength of 220 nm. Data were fitted by sigmoidal curve, and T_m values were determined as reported previously (1). Before and after the T_m measurement experiments, CD spectra of Sup35NM from 200–250 nm were acquired at 25 and 95 °C.

Amyloid Infection. Infection of [*psi*$^-$] yeast with in vitro-generated Sup35NM amyloid fibers was performed as previously reported (1).

NMR Backbone Signal Assignment. Backbone resonances of Sup35NM were assigned sequence specifically by analyzing 3D HN(CO)CA, HNCA, CBCANH, CBCA(CO)NH, HN(CA)CO, HNCO, and HN(CA)NNH as previously reported (6, 7). These spectra were acquired with a Bruker Avance III 800 spectrometer equipped with a cryogenic probe at 25 °C. To avoid protein aggregation, these spectra were measured in 50 mM Mes buffer including 10% D_2O (pH 3.0). After the assignment, signals were traced by pH titration measurement from pH 3.0 to pH 5.2. NMR data were processed by TopSpin (Bruker BioSpin) or XWINNMR (Bruker BioSpin) and analyzed by SPARKY (https://www.cgl.ucsf.edu/home/sparky). Ninety-four percent of the signals of main-chain amide protons were successfully assigned. A Sup35NM solution was passed through a 100-kDa-cutoff filter before NMR measurement for elimination of preexisting aggregates. Details are described below.

T_1 and T_2 and NOE Analysis. NMR relaxation measurements of 100 μM Sup35NM were performed in 50 mM Mes buffer (pH 5.2) at 37 °C with a Bruker Avance III 600 spectrometer equipped with a cryogenic probe. The relaxation delay for T_1 and T_2 measurements was 3 s. The ^{15}N T_1 and ^{15}N T_2 decays were recorded using 10 data points: 0.010, 0.050, 0.100, 0.200, 0.300, 0.400, 0.600, 0.800, 1.000, and 1.400 s and 0.017, 0.034, 0.051, 0.068, 0.085, 0.102, 0.136, 0.170, 0.204, and 0.238 s, respectively. ^{1}H-^{15}N heteronuclear NOE values were measured with two different datasets, one collected without initial proton saturation and a second one with initial proton saturation (8).

CLEANEX-PM NMR Analysis. CLEANEX-PM measurements of 100 μM Sup35NM were performed in 50 mM Mes buffer (pH 5.2) at 37 °C with a Bruker Avance III 600 spectrometer equipped with a cryogenic probe. The ^{1}H-^{15}N signal recovery by proton exchange with bulk solvent was recorded using five different mixing times (10, 20, 35, 50, and 65 ms). The hydrogen exchange rate, k_{ex}, was determined by single exponential fitting of the data using Igor software (Wavemetrics).

STD NMR Analysis. ^{1}H-^{15}N STD-HSQC spectra were recorded using a Bruker Avance 500 spectrometer equipped with a cryogenic probe. Measurements were performed with an equal mixture of nonlabeled Sup35NM and uniformly ^{2}H,^{15}N-labeled Sup35NM (total 100 μM Sup35NM in the mixture) in 50 mM Mes (pH 5.2) including 10% D_2O at 22 °C. To exclude water-edited pseudosignals, STD signals of only ^{2}H,^{15}N-labeled Sup35NM were used as a control. STD-HSQC spectra were acquired with selective methyl proton irradiation of nonlabeled Sup35NM at 3 ppm for on-resonance spectra and at 40 ppm for off-resonance reference spectra (9). The irradiation power level was 60 db, and the saturation time was 3 s.

PRE NMR Analysis. After 2-mercaptoethanol was eliminated by dilution and the Sup35NM protein solution was reconstituted, the single-cysteine mutant was treated with a 10-fold excess of MTSL (Toronto Research Chemicals, Inc.) in 6 M guanidium hydrochloride at room temperature for 2 h. MTSL-labeled Sup35NM was desalted by reverse-phase HPLC chromatography (Protein-R; Nacalai Tesque), followed by lyophilization. PRE effects were monitored by ^{1}H-^{15}N HSQC signal intensity on a Bruker Avance III 600 spectrometer equipped with a cryogenic probe. ^{15}N-labeled/MTSL-labeled Sup35NM spectra reflect the inter- and intramolecular PRE effects, while the ^{14}N-nonlabeled/MTSL-labeled Sup35NM and ^{15}N-free/MTSL-free Sup35NM spectra reflect only intermolecular PRE effects (10).

Amyloid Formation Kinetics Probed by ThT. Spontaneous and seeded amyloid formation kinetics were monitored with a plate reader (Spectra Max M2; Molecular Devices), using ThT (Sigma) as a

fluorescent probe (3). Excitation of ThT fluorescence was at 442 nm, and emission was monitored at 485 nm. Typical reactions include 5 μM Sup35NM and 20 μM ThT in 5 mM buffer C in the absence or presence of sonicated preformed amyloids as seeds [5% (mol/mol)].

Solid-State NMR Analysis. Solid-state NMR experiments on Sup35NM fibrils, where all four Phe residues were labeled by Phe-1-^{13}C, were carried out using a Varian INOVA spectrometer operating at 14.1 Tesla (600 MHz) and a 1.6 mm FAST-MAS probe. All datasets were recorded at an MAS frequency of 20 kHz and a sample temperature of 15 °C. Dipolar dephasing was achieved by PITHIRDS-CT recoupling as described by Tycko et al. (11). Pulse lengths of the 180° pulses for fpRFDR recoupling and PITHIRDS constant time blocks were equal to one-third of the rotor period, τ_R, i.e., 16.67 μs. Amplitudes of the 180° pulses were calibrated from a ^{13}C CP (cross polarization) followed by a 270° pulse of the length of 25 μs. The dipolar recoupling period, τ'_D, was incremented by a rearrangement of pulses within the recoupling sequence, which was incremented from 0–48 ms in steps of 4.8 ms. Each PITHIRDS-CT data point was obtained by adding 1,024 scans, with a recycle delay of 2 s. PITHIRDS-CT reference dephasing curves were calculated with the SIMPSON program using a linear five-spin system with internuclear distances from 4 Å to 8 Å. The raw PITHIRDS-CT data, $S_{raw}(t)$ were corrected for the 1.1% natural abundance of ^{13}C, which was estimated as a roughly linear decay of the signal to 70% after 68 ms (12, 13). The corrected decay curve, $S_{cor}(t)$, was calculated with the following equation: $S_{cor}(t) = [S_{raw}(t) - f_{na}(100 - 0.39 \times t/\text{ms})]/(1 - f_{na})$, where $f_{na,}$ the fraction of the ^{13}C signal due to the natural abundance spins, was estimated as 0.4 assuming that in a dry sample all ^{13}C′ spins contribute in a similar way to the CP signal, and $S_{raw}(t)$ was scaled such that $S_{raw}(0) = 100$.

CD Spectra. CD spectra of Sup35NM monomer were acquired at 37 °C with a J-818 Spectropolarimeter (Jasco) equipped with a Peltier thermal controller as previously reported (14).

Analytical Ultracentrifugation. Velocity area under the curve experiments were performed in a Beckman Optima XL-I analytical ultracentrifuge using an An60Ti rotor at 37 °C, and data were analyzed with Sedfit using the *c(S)* distribution method (www.analyticalultracentrifugation.com) as previously reported (14).

SDD-AGE. Yeast cells were grown in yeast extract/peptone/dextrose liquid medium for 1 d, collected, and resuspended in lysis buffer [25 mM Tris, 100 mM NaCl, 10 mM $MgCl_2$, 1 mM DTT, 5% glycerol, 1 mM EDTA, 1 mM PMSF, Protease Inhibitor mixture (pH 7.5)]. Cells were broken by a Multi Beads Shocker (Yasui Kikai), and lysates were cleared by brief centrifugation. Yeast lysates mixed with sample buffer (final 2% SDS) and run on a 1.5% agarose gel. Proteins were transferred to PVDF membranes (Millipore) and probed with an anti-Sup35 polyclonal antibody (14).

1. Tanaka M, Chien P, Naber N, Cooke R, Weissman JS (2004) Conformational variations in an infectious protein determine prion strain differences. *Nature* 428:323–328.
2. Tanaka M, Collins SR, Toyama BH, Weissman JS (2006) The physical basis of how prion conformations determine strain phenotypes. *Nature* 442:585–589.
3. Chien P, DePace AH, Collins SR, Weissman JS (2003) Generation of prion transmission barriers by mutational control of amyloid conformations. *Nature* 424:948–951.
4. Smirnovas V, et al. (2009) Distinct structures of scrapie prion protein (PrPSc)-seeded versus spontaneous recombinant prion protein fibrils revealed by hydrogen/deuterium exchange. *J Biol Chem* 284:24233–24241.
5. Furukawa Y, Kaneko K, Yamanaka K, Nukina N (2010) Mutation-dependent polymorphism of Cu,Zn-superoxide dismutase aggregates in the familial form of amyotrophic lateral sclerosis. *J Biol Chem* 285:22221–22231.
6. Ikura M, Kay LE, Bax A (1990) A novel approach for sequential assignment of 1H, 13C, and 15N spectra of proteins: Heteronuclear triple-resonance three-dimensional NMR spectroscopy. Application to calmodulin. *Biochemistry* 29:4659–4667.
7. Kay LE, Ikura M, Tschudin R, Bax A (1990) Three-dimensional triple-resonance NMR spectroscopy of isotopically enriched proteins. *J Magn Reson* 89:496–514.
8. Farrow NA, et al. (1994) Backbone dynamics of a free and phosphopeptide-complexed Src homology 2 domain studied by 15N NMR relaxation. *Biochemistry* 33:5984–6003.
9. Mayer M, Meyer B (2001) Group epitope mapping by saturation transfer difference NMR to identify segments of a ligand in direct contact with a protein receptor. *J Am Chem Soc* 123:6108–6117.
10. Clore GM, Iwahara J (2009) Theory, practice, and applications of paramagnetic relaxation enhancement for the characterization of transient low-population states of biological macromolecules and their complexes. *Chem Rev* 109:4108–4139.
11. Tycko R (2007) Symmetry-based constant-time homonuclear dipolar recoupling in solid state NMR. *J Chem Phys* 126:064506.
12. Shewmaker F, Kryndushkin D, Chen B, Tycko R, Wickner RB (2009) Two prion variants of Sup35p have in-register parallel beta-sheet structures, independent of hydration. *Biochemistry* 48:5074–5082.
13. Shewmaker F, Wickner RB, Tycko R (2006) Amyloid of the prion domain of Sup35p has an in-register parallel beta-sheet structure. *Proc Natl Acad Sci USA* 103:19754–19759.
14. Ohhashi Y, Ito K, Toyama BH, Weissman JS, Tanaka M (2010) Differences in prion strain conformations result from non-native interactions in a nucleus. *Nat Chem Biol* 6:225–230.

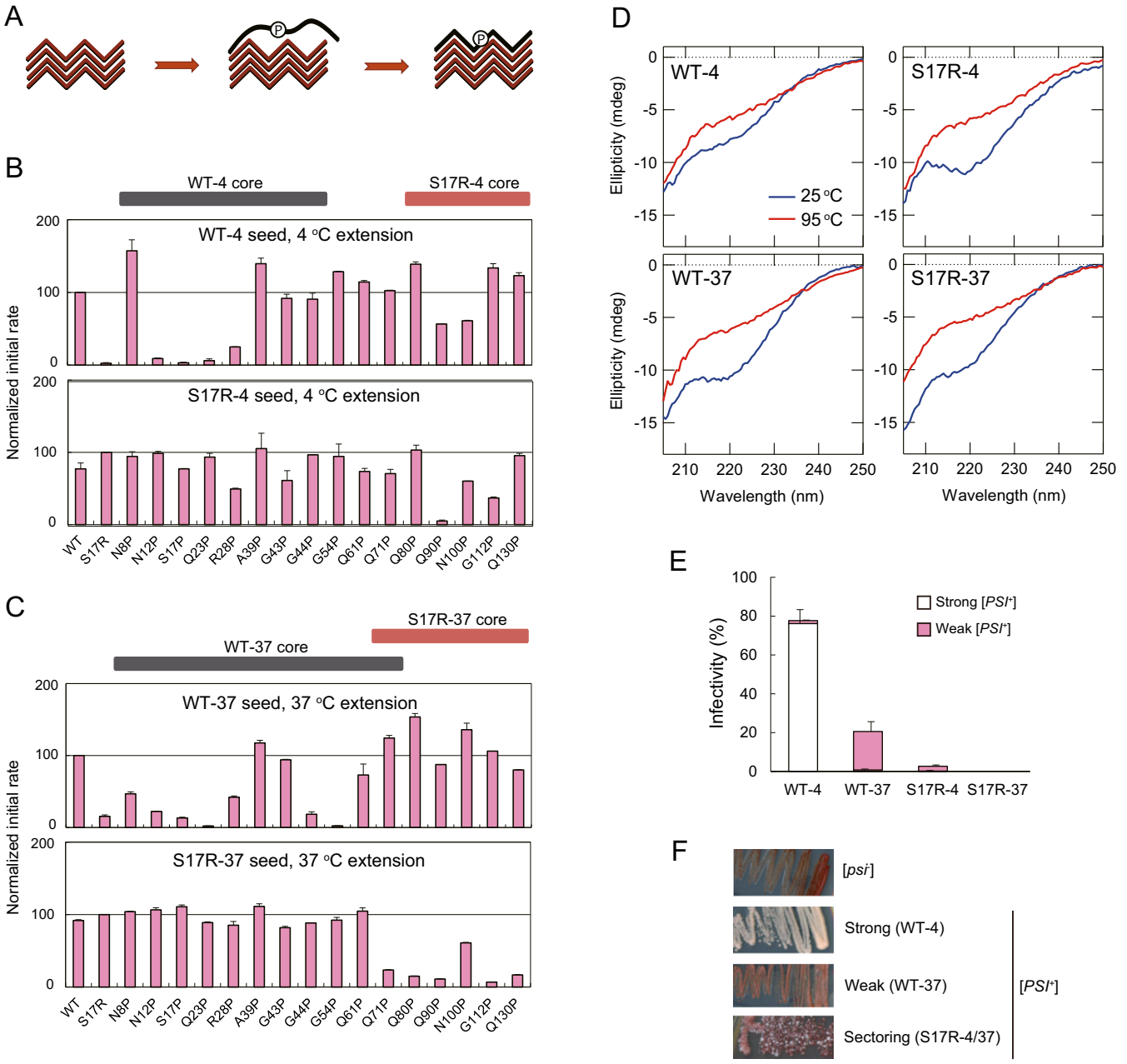

Fig. S1. Sup35NM can form two strikingly distinct amyloid conformations. (*A*) Schematic representation of proline-scanning experiments. The proline (P) mutation, which is located in the region critical to the monomer binding to amyloid seeds, causes defects in the initial rates of seeding reactions. (*B*) Initial rates of seeding reactions of 16 selected proline mutants monitored by ThT fluorescence using WT-4 and S17R-4 amyloid seeds. Initial rates were calculated by linear fitting of an increase in ThT fluorescent intensity, and the resulting values were normalized to the rate of seeding reactions using WT or S17R Sup35NM monomers with WT or S17R amyloid seeds, respectively. Gray and red bars indicate the core regions of WT-4 and S17R-4 amyloids, respectively. (*C*) Initial rates of seeding reactions of 16 selected proline mutants monitored by ThT fluorescence using WT-37 and S17R-37 amyloid seeds. Gray and red bars indicate the core regions of WT-37 and S17R-37 amyloids, respectively. The initial rates are an average from two independent experiments. Error bars denote SEM. (*D*) Far-UV CD spectra of WT-4, WT-37, S17R-4, and S17R-37 amyloids at 25 °C (blue) and 95 °C (red) in the T_m experiments. (*E*) Infectivity of in vitro-generated Sup35NM amyloids and prion strains obtained by protein infection to [*psi*$^-$] yeast. The S17R amyloid shows very low infectivity. White and pink bars indicate strong and weak/sectoring phenotypes, respectively. The infectivity is an average from four independent experiments. Error bars denote SEM. (*F*) Color phenotypes of prion strains obtained by infection with Sup35NM amyloid. WT-4 and WT-37 amyloids induce the stable white (strong) and pink (weak) [*PSI*$^+$] phenotypes, respectively, while S17R amyloid caused unstable sectoring/weak [*PSI*$^+$] phenotypes.

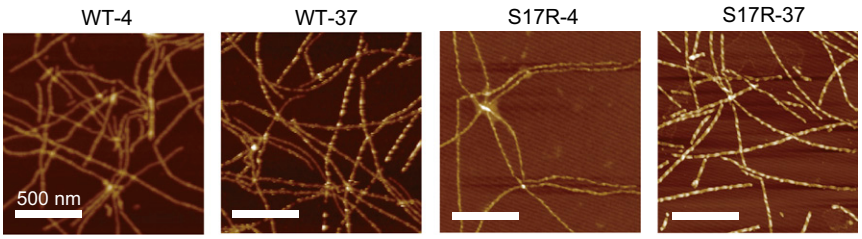

Fig. S2. AFM images of WT and S17R Sup35NM amyloids.

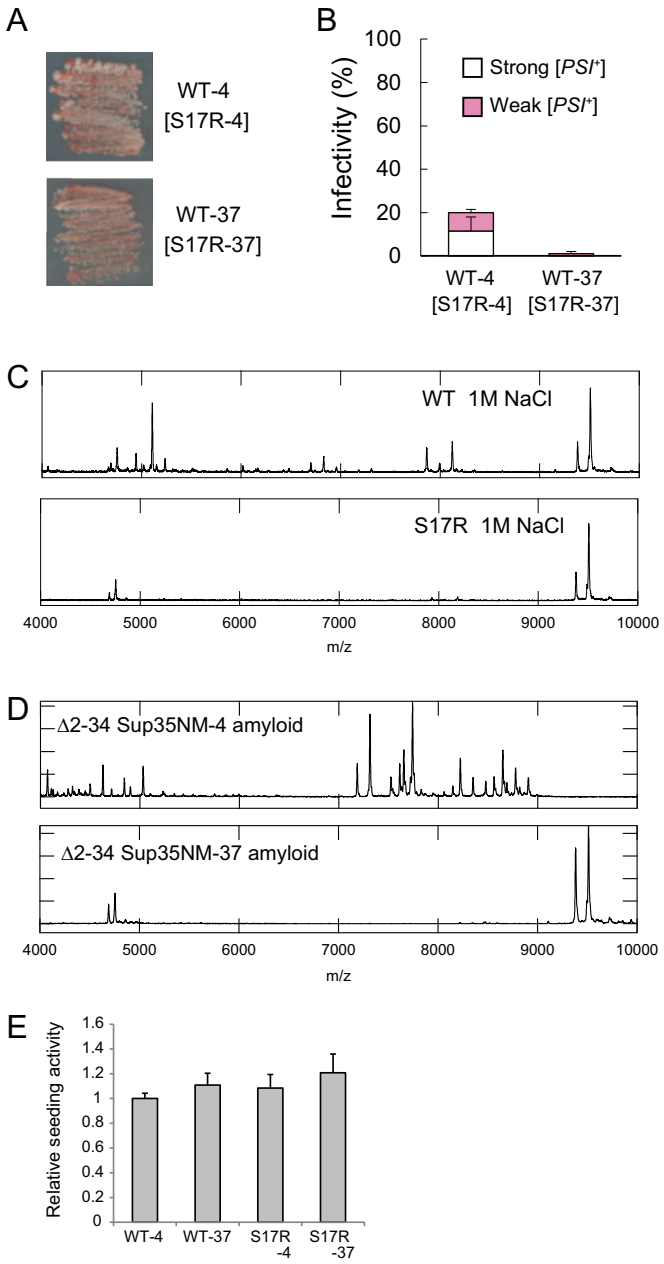

Fig. S3. WT Sup35NM has the potential to form a PrD-C core. (*A*) Typical color phenotypes of [*PSI*$^{+}$(WT[S17R])] strains obtained by infection of [*psi*$^{-}$] yeast by in vitro-generated WT[S17R] amyloid. (*B*) Infectivity of Sup35NM amyloids and color phenotypes of prion strains obtained by protein infection of [*psi*$^{-}$] yeast. White and pink bars indicate strong and weak/sectoring phenotypes, respectively. The infectivity is an average from two independent experiments. Error bars denote SEM. (*C*) High-*m/z*-range MALDI-TOF-MS spectra (*m/z* 4,000–10,000) of core peptides derived from Sup35NM WT (*Upper*) and S17R (*Lower*) amyloids formed in the presence of 1 M NaCl in buffer C at 37 °C. Note that the peptides (amino acids 61/62–144) of the S17R-type amyloid core were detected in both mass spectra. (*D*) High-*m/z*-range MALDI-TOF-MS spectra (*m/z* 4,000–10,000) of core peptides derived from Δ2–34 Sup35NM-4 (*Upper*) and Δ2–34 Sup35NM-37 (*Lower*) amyloids. (*E*) Seeding activity of WT and S17R amyloids toward the WT monomer. The normalized seeding activity at 30 °C is an average from four independent experiments. Error bars denote SEM; $n = 4$.

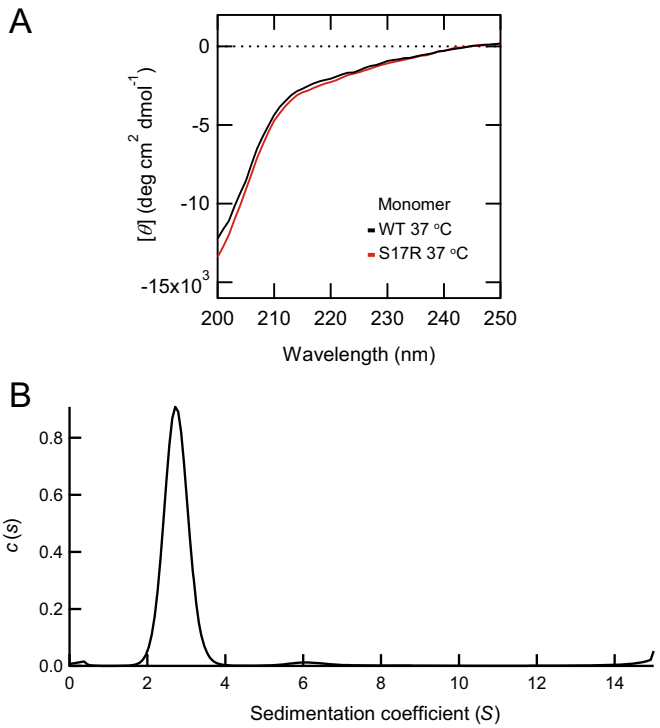

Fig. S4. Sup35NM is an intrinsically disordered monomeric protein at 37 °C. (*A*) Far-UV CD spectra of WT (black) and S17R (red) monomer Sup35NM at 37 °C. (*B*) Distribution of sedimentation coefficients of WT Sup35NM monomer (100 μM) at pH 5.3 and 37 °C by analytical ultracentrifugation.

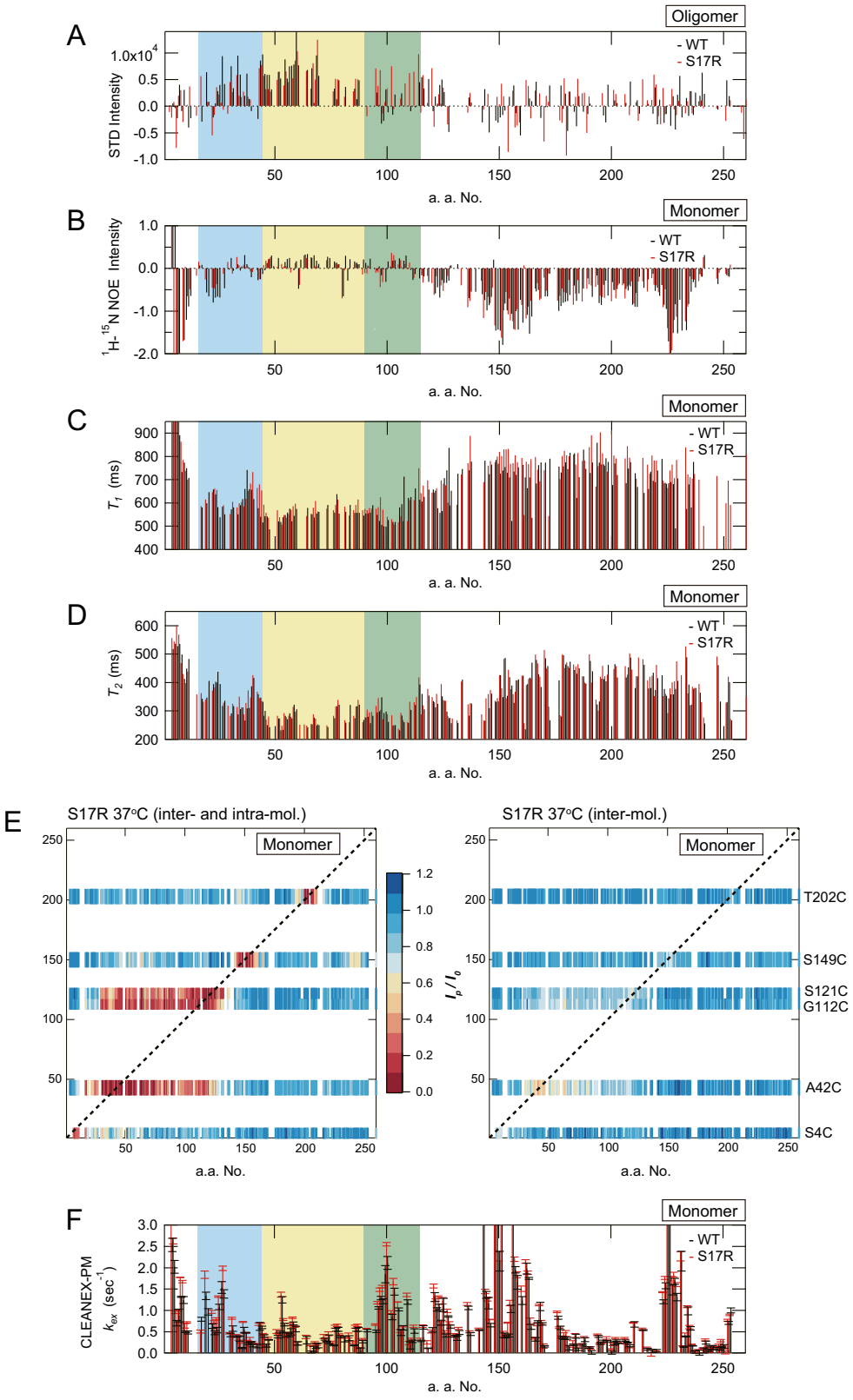

Fig. S5. Intrinsically disordered Sup35NM protein forms latent compact local structures. (*A*) STD signal intensity of WT (black) and S17R (red) Sup35NM at 22 °C. The blue and green areas indicate the amino acid regions with increased STD signals specific to WT and S17R Sup35NM, respectively. (*B*) ^{1}H-^{15}N heteronuclear NOE values for WT (black) and S17R (red) Sup35NM at 37 °C. (*C*) ^{15}N longitudinal relaxation times (T_1) of WT (black) and S17R (red) Sup35NM monomers at 37 °C. (*D*) ^{15}N transverse relaxation times (T_2) of WT (black) and S17R (red) Sup35NM monomers at 37 °C. (*E*) PRE of the S17R Sup35NM monomer monitored by ^{1}H-^{15}N HSQC signal intensity. A MTSL spin probe was introduced into each selected single-cysteine Sup35NM mutant (S4C, A42C, G112C, S121C, S149C, and T202C). Inter/intramolecular (*Left*) and intermolecular (*Right*) PRE values at 37 °C are shown as a color scale showing the I_p/I_0 ratio. (*F*) Hydrogen exchange rates of WT (black) and S17R (red) Sup35NM at 37 °C measured by CLEANEX-PM NMR.

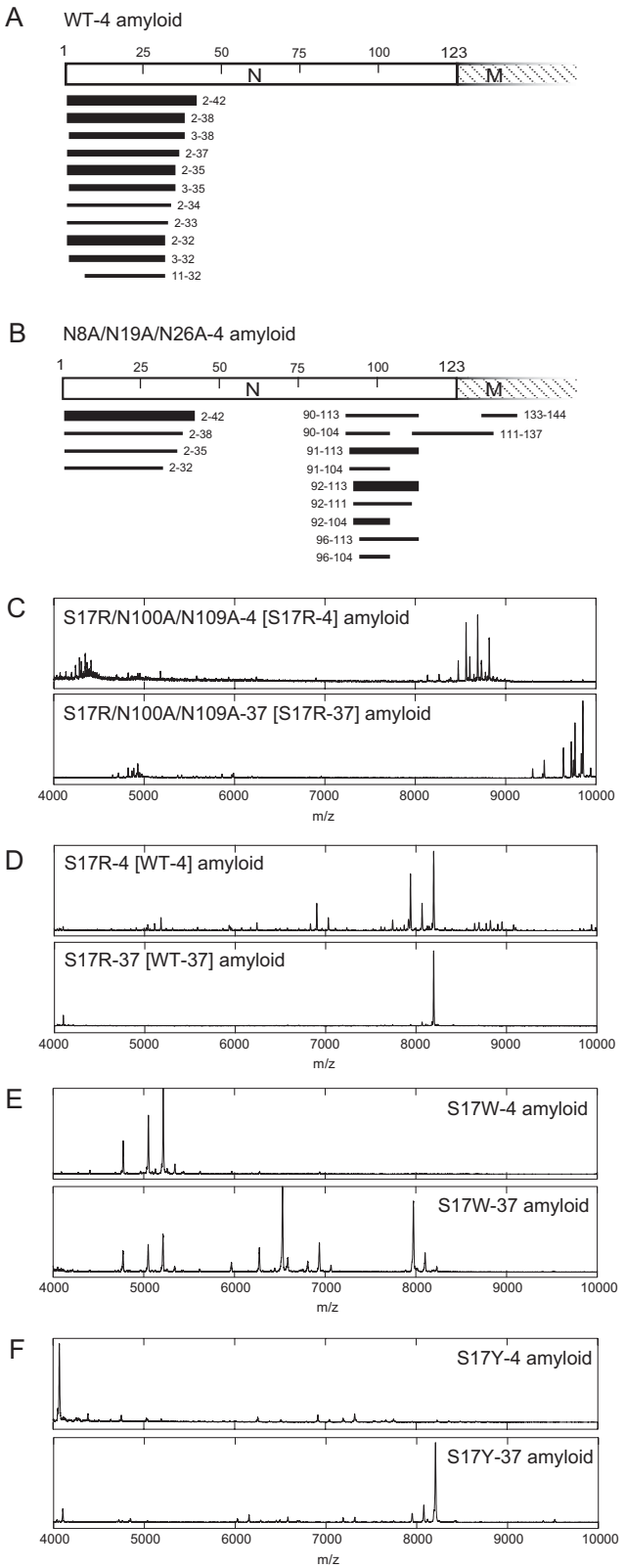

Fig. S6. Amyloid core regions of Sup35NM mutants by mass spectral analysis. (*A*) Core peptides identified in MALDI-TOF/TOF-MS spectra of WT-4 amyloid were aligned to the primary sequence of Sup35NM. The line width is proportional to the signal intensity of peaks in mass spectra. (*B*) Core peptides identified in MALDI-TOF/TOF-MS spectra of N8A/N19A/N26A-4 amyloid were aligned to the primary sequence of Sup35NM. The line width is proportional to the signal intensity of peaks in mass spectra. (*C*) High-*m*/*z*-range MALDI-TOF-MS spectra (*m*/*z* 4,000–10,000) of core peptides derived from S17R/N100A/N109A-4[S17R-4] and S17R/N100A/N109A-37[S17R-37] amyloids. (*D*) High-*m*/*z*-range MALDI-TOF-MS spectra (*m*/*z* 4,000–10,000) of core peptides derived from S17R-4[WT-4] and S17R-37[WT-37] amyloids. (*E*) High-*m*/*z*-range MALDI-TOF-MS spectra (*m*/*z* 4,000–10,000) of core peptides derived from S17W-4 and S17W-37 amyloids. (*F*) High-*m*/*z*-range MALDI-TOF-MS spectra (*m*/*z* 4,000–10,000) of core peptides derived from S17Y-4 and S17Y-37 amyloids.

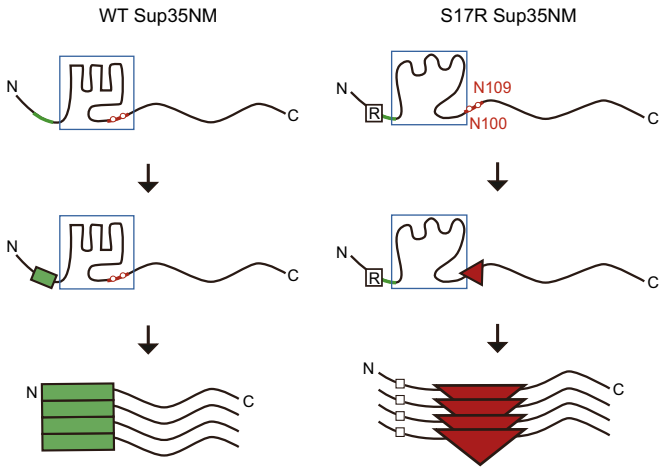

Fig. S7. A proposed model for diversification of Sup35NM amyloid conformation. (*Left*) WT Sup35NM forms a local compact structure (blue box) with buried Asn100 and Asn109, selecting the N-terminal region in the prion domain as an initiation site for amyloid extension (green). (*Right*) By contrast, the S17R mutant shows a relatively unfolded compact structure (blue box). The exposure of Asn100 and Asn109 together with the preference of the S17R mutation not to adopt the N-terminal core results in the selection of PrD-C as an initiation site for amyloid extension (red). The S17R amyloid shows a reduced efficiency in chaperone-mediated fiber fragmentation, which induces the weak/sectoring [*PSI*$^{+}$] strain phenotype.

Table S1. Sup35NM amyloid core peptides identified by mass spectral analysis

Sup35NM amyloid	Fragment, amino acids	Experimental mass, Da	Predicted mass, Da
WT-4	2–38	4,303.5	4,301.2
	2–42	4,671.0	4,668.7
	2–45	4,948.8	4,945.9
	2–46	5,112.3	5,109.1
WT-37	2–70	7,873.7	7,868.9
	2–71	8,001.3	7,997.0
	2–72	8,130.3	8,125.2
S17R-4	82–144	7,187.7	7,184.8
	81–144	7,315.9	7,313.0
	82–147	7,527.9	7,525.3
	82–148	7,615.4	7,612.4
	81–147	7,656.7	7,653.4
	81–148	7,744.3	7,740.5
S17R-37	63–144	9,385.8	9,386.1
	62–144	9,514.8	9,514.2
WT-4 [S17R-4]	82–144	7,189.1	7,184.8
	81–144	7,317.2	7,313.0
	82–147	7,529.2	7,525.3
	82–148	7,616.6	7,612.4
	81–147	7,657.7	7,653.4
	81–148	7,744.8	7,740.5
WT-37 [S17R-37]	63–144	9,387.6	9,386.1
	62–144	9,515.9	9,514.2
S17R-4 [WT-4]	2–61	6,903.1	6,902.0
	2–70	7,938.8	7,938.0
	2–71	8,067.6	8,066.1
	2–72	8,195.4	8,194.3
S17R-37 [WT-37]	2–72	8,194.4	8,194.3
S17R/N100A/N109A-4	2–35	4,059.3	4,057.1
	2–37	4,244.1	4,242.3
	2–38	4,373.0	4,370.4
	2–42	4,740.6	4,737.8
	2–45	5,018.3	5,015.1
	2–46	5,179.9	5,178.3
S17R/N100A/N109A-37	2–70	7,939.1	7,938.1
	2–71	8,067.5	8,066.3
	2–72	8,196.1	8,194.4
S17R/N100A/N109A-4 [S17R-4]	73–148	8,562.1	8,563.4
	72–148	8,690.1	8,691.6
	71–148	8,817.8	8,819.7
S17R/N100A/N109A-37 [S17R-37]	63–147	9,638.9	9,641.5
	63–148	9,726.1	9,728.6
	62–147	9,767.2	9,769.7
	62–148	9,854.0	9,856.7
1M NaCl WT-37	2–46	5,107.8	5,109.1
	2–70	7,865.5	7,868.9
	2–72	8,121.4	8,125.2
	63–144	9,381.0	9,386.1
	62–144	9,509.1	9,514.2
1M NaCl S17R-37	63–144	9,380.1	9,386.1
	62–144	9,508.1	9,514.2
Δ2–34 S17R-4	82–144	7,185.2	7,184.8
	81–144	7,313.3	7,313.0
	82–147	7,525.3	7,525.3
	82–148	7,612.6	7,612.4
	81–147	7,653.5	7,653.4
	81–148	7,741.1	7,740.5
Δ2–34 S17R-37	63–144	9,382.7	9,386.1
	62–144	9,512.3	9,514.2

Table S1. Cont.

Sup35NM amyloid	Fragment, amino acids	Experimental mass, Da	Predicted mass, Da
S17W-4	2–42	4,773.0	4,767.8
	2–45	5,050.6	5,045.0
	2–46	5,214.0	5,208.2
S17W-37	2–55	6,273.9	6,270.4
	2–57	6,530.1	6,526.6
	2–62	6,938.1	6,932.0
	2–70	7,973.1	7,968.0
	2–71	8,102.3	8,096.1
S17Y-4	2–35	4,067.0	4,065.1
S17Y-37	2–70	7,945.4	7,946.0
	2–71	8,073.6	8,074.2
	2–72	8,201.7	8,202.3